Title
Biophysical Properties of Growing Actin Networks Measured With Atomic Force Microscopy

Author
Parekh, Sapun Harshad

Publication Date
2008-06-11

Peer reviewed|Thesis/dissertation

Biophysical Properties of Growing Actin Networks Measured With Atomic Force Microscopy

by

Sapun Harshad Parekh

DISSERTATION

Submitted in partial satisfaction of the requirements for the degree of

DOCTOR OF PHILOSOPHY

in

BIOENGINEERING

in the

GRADUATE DIVISION

of the

In memory of Jason Choy

Without whom this dissertation would not be possible

Acknowledgements

I remember my first days in Berkeley. My dad and I flew out to visit the winter before I moved here for school. I recall immediately feeling that someone like me belonged in a place like this…I didn't know what exactly I wanted to study, and UC Berkeley had seemingly more majors than students. I was interested in using engineering principles to solve problems in medicine, and Berkeley had world class expertise in engineering and a joint bioengineering graduate program with UC San Francisco, a first-rate research hospitals. Well after 6 years I can honestly say that, like most things in life, it didn't work out how I thought – I didn't work directly on medical problems and spent most of my time working on basic science – but this was by far the best time of my life.

If I listed everyone that helped me make the last 6 years so great, it would take too long so here is my abbreviated list. Near the top of this list is my advisor, Dan Fletcher. Dan was willing to take a chance on me to let me bounce around in his brand new lab despite the fact that it was quite clear that I knew nothing about the lab's thrusts of molecular and cell biology, biochemistry, or atomic force microscopy (all of which turned out to be critical to my graduate work). It takes a lot of trust to put your faith into someone totally inexperienced and naive, and I can't thank him enough for the opportunity. I will always admire Dan's ability to think about a problem, synthesize ideas and data, and develop very clear and satisfying explanations for seemingly complex and messy systems. I will miss walking down to his office to discuss perplexing scientific data or get a motivational speech when things aren't working. Perhaps the most important lessons that I will take from my 5 years working under Dan are to take risks,

keep things in perspective, and do what YOU like because life's too short. Dan taught me how to think like an engineer and answer questions like a scientist. I hope one day that I may be as good a mentor to someone else as he was to me.

In addition to Dan, many other faculty, grad students, and postdocs of the UC Berkeley and UC San Francisco communities have provided help and guidance during my PhD. Specifically, I would like to thank the other members of my dissertation committee, Roger Cooke and Dyche Mullins at UC San Francisco, and members of the Drubin, Mullins, Taunton, and Welch labs for invaluable experimental assistance.

The Fletcher lab has been a fantastic place to work for the past 5 years. The original four: Allen Liu, Mike Rosenbluth, Wendy Hansen, and I will always share initial memories and growing pains of setting up the lab and establishing our existence at UC Berkeley. I was very fortunate to have crossed paths with these folks as we banded together in the early days to help each out when we had no postdocs and no senior students to look to for advice. Allen has been a great friend and taught me everything I know about biochemistry even though we rarely worked on the same projects. He showed incredible patience to walk me through basic protein purification and molecular biology and taught me many great biochemical tricks. Mike and I have shared many experiences in grad school. Where do I begin, Namibia, the Dominican Republic, carpools, debugging AFMs, lab labels, finite-element modeling, graduate biochemistry, needle-free injection, airline boarding zones, or checked luggage? His cavalier demeanor and willingness to challenge "truths" is something that I will always admire. Wendy has never been afraid to speak her mind and keep me in check, and these last few months it has been refreshing to share thoughts and ideas about life after grad school.

While not part of the original four, my primary partner in grad school has been Ovijit Chaudhuri. The two of us have gone to war together on the actin-AFM project for the last 5 years and fought battle after battle against entrenched beliefs in the actin field. Ovi's cerebral approach to science along with his raw talent and critical thinking skills coupled with my determination and continued curiosity made us a great team. I have had the pleasure of working with him on numerous scientific endeavors, and it has been very fruitful for both of us. I hope that he learned as much from me as I did from him. Wilbur Lam has been a great resource and reality check for "real world" importance of my biophysics research as well as a valuable public servant as the lab doctor over the past years.

Our first postdocs, Josh Shaevitz and Martijn van Duijn, were instrumental in helping the "kids grow up" so to speak. Josh was a pillar of efficiency with great ideas and focus and a well established track record in the biophysics field. Never afraid to speak his mind, he taught me a significant amount of force microscopy and scientific analysis and helped me improve my scientific writing style. Martijn could do ANYTHING and had a wealth of experience in science. He always had something useful to say whether about microfabrication, electroporation, surface chemistry, or microscopy techniques, and he virtually ran the lab for two years. After our latest move to the new Stanley Hall, I have had the benefit of sitting next to Sander Pronk, a theorist postdoc with an impressive ability to write massive equations, who has always been willing to engage in long discussions about fundamental polymer physics. Ross Rounsevell and Tom Hunt have been great colleagues who are always ready to share their advice and

sage wisdom about life and helped me through some of the tougher times at the end. I will miss tea time, Tom's cheerful attitude, and Team Euro.

Another welcomed partner from our latest move was Jeanne Stachowiak. She is very professional and focused, and I admire her ability to block everything out and just get it done. Viviana Risca, Ailey Crow, Dave Richmond, and Thomas Li have been fun and extremely talented additions to the lab. They are all significantly further along than I was at comparable stages in grad school. I have recently had the opportunity to work with Dave and Ailey and am continually impressed with their ideas and enthusiasm. The lab is in good hands with this next crop, and Dan is lucky to have such a great group.

My fellow BioE classmates Nick Fawzi, Erik Douglas, Janine Lupo and Meredith Metcalf have always been there when things were rough. Rich Cohen (and Mike Rosenbluth) has become one of my closest friends through grad school as we planned many events together and struggled through many challenges together. His positive attitude and enthusiasm have inspired me to do things that I would have never attempted before, and I owe him much. Peter Coats, my best friend from college, was a great distraction from the lab and always ready to talk over a beer (or two) about life and politics. I couldn't have made it these past years without the friends outside of the lab and the ocean – surfing really does make people better.

Amy Robinson, Jennifer Davidson, Tere Falciglia, Catherine Ocampo, and the rest of the Bioengineering staff at UC Berkeley have been better than I could have ever hoped. From fighting with the higher-ups to make sure our lab got a fair shake to clearing a police charge (come ask if you want the details), they have always been there for us. SarahJane Taylor and Rebecca Pauling have been great for helping to navigate the

joint campus degree program. I would also like to thank the National Institutes of Health, National Science Foundation, and Achievements Rewards for Collegiate Scientists for financial support over the past 6 years.

Last but not least, I would like to thank my family. My parents have always been supportive even though they may not agree with my research directions. It has been both infuriating and infinitely useful to talk with Mom and Dad about life, grad school, and the real world. I can't imagine completing this degree without their guidance and support through these 6 years. Finally, I would like to thank Anika Keswani, who has taught me what it really means to not give up and go after what you want. She took a chance on me and gave up everything to become an AmeriCorps volunteer in San Francisco. Thanks for believing, and I look forward to building our life together. You are my everything.

Use of published material in this dissertation

The experimental research presented in this work comes primarily from three published papers, and combined with the three originally written chapters, forms a document with comparable content to a standard PhD dissertation. Daniel Fletcher supervised all research and co-wrote all published manuscripts used in this work. The text of Chapter 3 is a reprint of the material as it appears in *Review of Scientific Instruments*. Jason Choy and I built the original differential AFM and co-wrote the manuscript. I performed the majority of the instrument characterization, data collection, and data analysis. Ovijit Chaudhuri and Allen Liu assisted with data collection and manuscript revisions. Julie Theriot and Matthew Footer provided guidance and help with the actin experiments, and Carlos Bustamante helped with manuscript preparation and

data interpretation. The text of Chapter 4 is a reprint of the material as it appears in *Nature Cell Biology*. Ovijit Chaudhuri and I collected and analyzed all experimental data and co-wrote the manuscript. Julie Theriot provided the ActA protein for actin experiments and assisted with manuscript revisions. The text of Chapter 5 is a reprint of the material as it appears in *Nature*. Ovijit Chaudhuri and I collected and analyzed all experimental data and co-wrote the manuscript.

Abstract

Biophysical Properties of Growing Actin Networks Measured With Atomic Force Microscopy

by

Sapun Harshad Parekh

Doctor of Philosophy in Bioengineering

University of California, San Francisco and University of California, Berkeley

Professor Daniel A. Fletcher, Chair

The dynamic actin cytoskeleton plays a key role in a number of cellular processes including motility and shape change. Composed of individual filaments polymerized from actin monomers, the actin cytoskeleton is organized into a branched and cross-linked dendritic network by a diverse set of actin binding proteins. Directed growth of dendritic actin networks by monomer addition, such as at the leading edge of a crawling cell, generates the mechanical forces necessary for deforming the membrane during cell motility, endocytosis, and phagocytosis. Dysfunctional actin network regulation is associated with metastatic cancers, immune system disorders, and bacterial infection and pathogenesis.

Significant biochemical work over the past four decades has culminated into the dendritic nucleation model for actin network growth. This model summarizes the role of the major actin binding proteins, and interactions among them, that form and maintain a growing, dendritic actin network in crawling cells. Though actin biochemistry has been

well studied, the force-generating ability and mechanical properties of growing dendritic actin networks that produce dynamic cellular shape changes remain unclear. This dissertation presents development of a unique measurement system for the purpose of understanding the biophysics of dendritic actin network growth. An experimental platform was built around a custom differential atomic force microscope by adapting a method for reconstituting actin network growth from cell-free extract *in vitro* to measure network force production and mechanics. The results described here demonstrate that dendritic actin networks possess a built-in force feedback system that enables active remodeling to support increasing forces. In addition, these networks exhibit the ability to reversibly stress soften under large loads, thereby avoiding catastrophic failure and retaining their underlying network structure as a molecular scaffold. These results have implications for understanding how crawling cells navigate through the physical barriers of the extracellular matrix and connective tissue *in vivo* while feeling a wide range of compressive forces.

_____

Professor Daniel A. Fletcher, Dissertation Committee Chair

Table of Contents

CHAPTER 1: INTRODUCTION 1

1.1 OVERVIEW 1
1.2 DIRECTED MOVEMENTS 2
1.2.1 Diffusive vs. active motion 2
1.2.2 Cell motility and morphogenesis 4
1.2.3 Cell motility and disease 7
1.3 CELLULAR ACTIN NETWORKS 8
1.3.1 Actin biochemistry 8
1.3.2 Functional actin networks 10
1.3.3 Dendritic actin networks 12
1.4 FORCE GENERATION BY ACTIN NETWORK GROWTH 17
1.4.1 Force generation by single actin filaments 17
1.4.2 Theoretical developments 19
1.4.3 Force generation by dendritic actin networks 21
1.5 ACTIN NETWORK MECHANICS 25
1.5.1 Actin filaments are semiflexible polymers 25
1.5.2 Rheological studies of actin networks 26
1.6 ATOMIC FORCE MICROSCOPY IN LIFE SCIENCE 29
1.6.1 Atomic force microscopy concept 30
1.6.2 Atomic force microscopy applications in biology 31

CHAPTER 2: BUILDING AN ATOMIC FORCE MICROSCOPE 33

2.1 INTRODUCTION TO ATOMIC FORCE MICROSCOPY CONSTRUCTION 33
2.2 ANATOMY OF AN ATOMIC FORCE MICROSCOPE 34
2.2.1 Laser 35
2.2.2 Position-sensitive detection 38
2.2.3 Nanopositioning systems 45
2.2.4 Macroscopic alignment 48
2.3 OPTICAL IMAGING 49

2.4 NOISE AND CALIBRATION 49
2.4.1 Noise 49
2.4.2 Stiffness calibration 52
2.5 CONCLUSION 53

CHAPTER 3: DIFFERENTIAL FORCE MICROSCOPE FOR LONG-TIMESCALE BIOPHYSICAL MEASUREMENTS 56

3.1 ABSTRACT 57
3.2 INTRODUCTION 58
3.3 ATOMIC FORCE MICROSCOPY FOR BIOPHYSICAL MEASUREMENTS 59
3.4 INSTRUMENT DESIGN AND PERFORMANCE 61
3.4.1 Design principles 61
3.4.2 Optical lever detection 63
3.4.3 Spatial stability characterization 66
3.5 APPLICATION TO ACTIN NETWORK GROWTH 68
3.6 DISCUSSION & CONCLUSIONS 71
3.7 METHODS 72
3.7.1 Differential force microscope components 72
3.7.2 Protein preparation 73
3.7.3 Actin network force-clamp measurements 73
3.8 ACKNOWLEDGEMENTS 74

CHAPTER 4: LOADING HISTORY DETERMINES THE VELOCITY OF ACTIN NETWORK GROWTH 75

4.1 ABSTRACT 76
4.2 INTRODUCTION 76
4.3 RESULTS AND DISCUSSION 79
4.4 CONCLUSIONS 85
4.5 METHODS 86
4.5.1 Protein preparation 86
4.5.2 Differential AFM 87
4.5.3 Force measurements 88

4.5.4 Data analysis 88
4.6 ACKNOWLEDGEMENTS 89
CHAPTER 5: REVERSIBLE STRESS SOFTENING OF ACTIN NETWORKS 90
5.1 ABSTRACT 91
5.2 INTRODUCTION 92
5.3 RESULTS AND DISCUSSION 94
5.4 CONCLUSIONS 100
5.5 METHODS 103
5.5.1 AFM-based microrheology 103
5.5.2 Stress dependence measurements 104
5.5.3 Data Analysis 104
5.6 ACKNOWLEDGEMENTS 105
CHAPTER 6: CONCLUSION 106
6.1 OVERVIEW 106
6.2 SUMMARY OF FINDINGS 107
6.3 ONGOING EXPERIMENTAL WORK AND FUTURE DIRECTIONS 109
6.3.1 Force generation 109
6.3.2 Mechanics 110
6.4 LONG TERM OUTLOOK 112
APPENDIX I: SUPPLEMENTARY INFORMATION FOR CHAPTER 4 114
APPENDIX II: SUPPLEMENTARY INFORMATION FOR CHAPTER 5 120
REFERENCES 128

List of Figures

Figure 1.1 Four steps of cell motility as described in reference *(13)*. 5
Figure 1.2 Actin filaments grow and shrink at their end by monomer addition. 10
Figure 1.3 Illustration showing different actin network structures and corresponding behaviors. 11
Figure 1.4 Dendritic nucleation model for actin network growth in lamellipodia of crawling cells. 12
Figure 1.5 Schematic illustration of bulk rheology assays. 27
Figure 1.6 Schematic of AFM measurement of actin network growth. 30
Figure 2.1 Basic AFM setup. 35
Figure 2.2 Cantilever deflection and beam translation on a SPD. 39
Figure 2.3 LEPD operating principle. 40
Figure 2.4 Telescopes to scale deflection on lateral effect photodiodes. 42
Figure 2.5 Basic piezo expansion principle. 46
Figure 3.1 Optical schematic of the differential force microscope. 61
Figure 3.2 Ray optics diagram of the objective-based optical lever and power spectrum of cantilever noise, both shown for a single cantilever. 65
Figure 3.3 Cantilever-surface drift, Δz, with position clamp active. 68
Figure 3.4 Simultaneous force and fluorescence microscopy of actin network growth in a force clamp. 70
Figure 4.1 Growth of an actin network from an AFM cantilever. 78
Figure 4.2 Force-velocity relationship of actin network growth under increasing forces. 80
Figure 4.3 Force-reduction experiments showing two stable velocities at a single force. 83
Figure 5.1 AFM-based microrheology of growing dendritic actin networks. 95
Figure 5.2 Frequency dependence of elastic (filled triangles, *E'*) and viscous (open triangles, *E''*) moduli. 96
Figure 5.3 Dendritic actin networks exhibit stress stiffening and reversible stress softening. 98
Figure 5.4 Stress stiffening and stress softening can arise in dendritic networks due to filaments resisting extension and buckling of filaments resisting compression. 101

Figure I.1 Cartoon illustration showing the side view of dual cantilever AFM setup. .. 114
Figure I.2 Constant force experiment. 117
Figure I.3 Mechanical stall of dendritic actin network growth. 118
Figure II.1 Cantilever-surface coupling as a function of standoff distance from surface. 124
Figure II.2 Cantilever-surface coupling in extract mix does not change with time. 125
Figure II.3 Power law does not change significantly during a frequency sweep due to growth of the network. 126

List of Tables

Table 1.1 Summary of force measurements on actin filament and dendritic network growth. 24
Table 2.1 SPD and LEPD characteristics. 43

CHAPTER 1: INTRODUCTION

1.1 Overview

This dissertation presents the bulk of my PhD research that was focused on understanding the biophysics of directed cellular movement, or motility, and more specifically to understand force generation by dendritic actin networks. Chapter 1 describes the importance of this study and introduces basic concepts in actin biochemistry/biophysics and atomic force microscopy (AFM) relevant for understanding the ideas and results that follow. Chapter 2 provides a compilation of useful topics to consider when constructing an AFM, including a basic parts list as well as common problems that one may encounter along the way. Chapter 3 builds on these ideas by detailing the design principles and performance enhancement realized by constructing a differential AFM. This instrument, around which we designed a unique experimental system, was used to obtain the results presented in Chapters 4 and 5. Chapter 4 presents our results demonstrating that dendritic actin networks generate significant forces and possess the ability to physically remodel as they grow against increasing opposing loads. Chapter 5 shows that these networks exhibit the ability to reversibly stress soften under large compressive forces rather than catastrophically fracture. Chapter 6 begins with a summary of the results presented in the previous chapters and provides context for these

results. Then it describes follow-up experiments that dig deeper into the mechanistic details of how dendritic actin networks accommodate increasing forces. Finally, Chapter 6 closes by describing potential future applications to biomedicine.

While the content of this dissertation comprises the major focus of my graduate work, it does not describe, in detail, my involvement with other projects in the lab. Specifically, my efforts in the design and construction of two additional AFMs: 1) an instrument that allows side imaging of a sample (along the loading direction) concurrently with thermally limited force and position detection and 2) an instrument with independent spatial control of two probes will not be described. In addition, my early work on construction of a piezo-electrically powered transdermal drug delivery device, and more recently, my contribution to developing a new technique for the encapsulation of biological macromolecules into biomimetic lipid vesicles, will also not be described. These side projects have resulted in two published papers *(1)* and *(2)* and another manuscript in preparation *(3)*.

1.2 Directed movements

1.2.1 Diffusive vs. active motion

Solute molecules in solution are constantly colliding with other solutes and solvent molecules. Each of these species has a fundamental amount of thermal energy, $E_T = \frac{1}{2} k_B T$, for every degree of freedom where k_B is Boltzmann's constant, and T is the temperature of the molecule (in Kelvin) *(4)*. Observing a solution of particles (microspheres, for example) under a microscope, this thermal (or random) energy is seen

as a constant "jiggling" of the particles *(5)*. Consider for a moment the length scales and physics that govern thermal motion (better known as diffusion). If a typical protein has a diffusion coefficient of, $D \sim 10^{-5}$ cm^2/sec, then based on diffusive movement, it would take more than 15 years for this protein to reach a position 1 m away *(6)*. Transport over this distance is exactly the situation in the sciatic nerve that extends from the spinal column to the base of the leg *(7)*. Because neurotransmitters are actively transported by tiny molecular machines and do not take years to reach the synaptic cleft, our minds process information and react to stimuli considerably faster than the timescale based on diffusive motion. Therefore, this requires an active and directed method of transport. While this example clearly illustrates that active processes are essential in neural transport, more generally, directed motion is evident in numerous aspects of life as we know it.

Single molecular machines such as kinesin *(8)* and myosin *(9)* act like little shuttles that carry cargo to specific locations within cells. For example kinesin molecules carry cargo down axons to nerve endings that participate in synaptic communication in the brain. Evidence for the role force generation is apparent at a higher level: whole cells move throughout the body to specific areas during wound healing, angiogenesis, and immune responses against foreign pathogens by coordinated interaction among many different proteins in a site-directed fashion *(10)*. Immune cells mobilize their motile machinery to follow sources of chemotractant molecules when chasing bacteria or moving to the site of injury. Finally, at the organ level, the collective action of individual cells results in macroscopic motion such as contraction of cardiac muscle cells during

heart beats *(10)*. These examples demonstrate that directed non-random movements are instrumental in countless physiological processes.

1.2.2 Cell motility and actin-driven protrusions

Directed cell motility or crawling is an example of an active process that is fundamental in many biological processes. Initial studies of cell motility date back as early as 1953 where Abercrombie and colleagues observed that inter-cellular proximity affects motility rate of chick heart fibroblasts *(11)*. Cell crawling speed was inversely proportional to the density of the cultures, a concept that was later understood as contact inhibition *(12)*. Since these initial studies, a plethora of research has been devoted to dissecting the mechanistic basis of cell movements. This research has culminated into a four step process that has been reviewed extensively elsewhere *(13)*. Briefly, I will mention the four steps involved in cellular motility (assuming that cellular polarization has already occurred): 1) protrusion of the leading edge, 2) adhesion formation at the leading edge, 3) translocation of the trailing cell body (and nucleus), and 4) de-adhesion of the rear portion of the cell as shown in Figure 1.1 *(13)*. This dissertation is concentrated on step 1 of this process with the aim to answer the fundamental question: how is protrusive force generated at the leading edge of a cell?

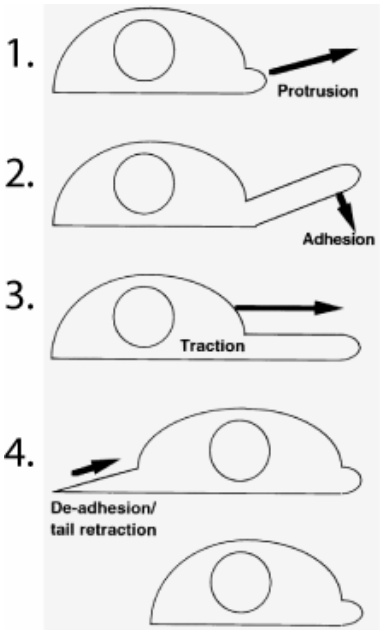

Figure 1.1 Four steps of cell motility as described in reference *(13)*.

These steps are executed in a repeated fashion as cells crawl through the body. Growing actin networks are believed to provide the force for protrusion (step 1).

In contrast to the idea that the nucleus is the central processing unit and command center for the cell, recent work has explicitly demonstrated that cellular fragments physically separated from the nucleus are capable of undergoing basic motility similar to that of whole cells *(14)*. This work highlights the importance of another part of the cell, the cytoskeleton. The cytoskeleton is the structural scaffold that gives cells their shape, allows them to resist deformation, participates in sensing of external stimuli, and is dynamically regulated during various cellular processes from mitosis to motility. The cytoplasm is the interstitial fluid that shares the space between the nuclear and cellular membrane with the cytoskeleton. This fluid contains thousands of protein and small molecule components that interact with signaling molecules to relay information through the cell and interact with the cytoskeleton *(15)*.

Of particular interest in motility is the actin filament cytoskeleton, one of the three components of the cytoskeleton *(15)*, because of recent studies showing that actin network growth is linked with cell protrusion *(13)*. Experimental results demonstrating that growing actin networks are necessary for leading edge protrusion during cell motility *(16)*, coupled with the finding that actin filament networks can deform lipid vesicles and generate forces *(17)*, have led to the belief that growing actin networks generate power for leading edge protrusion. While actin filaments are often considered static substrates for myosin-driven contractions as in skeletal muscle cells, it should be noted that myosin is not required for protrusive force generation by growing actin networks *(13)*.

A critical requirement for productive displacement against a movable load by filament growth is a rigid support to push off from, otherwise force generation results in compression of the support rather than protrusion of the membrane. As such, growing actin filaments in the network must push off the existing network/internal cytoskeleton in order to generate productive motion during the protrusive phase of motility. This highlights the importance of actin network mechanical properties in addition to their ability to generate force.

While involvement of the actin cytoskeleton in cell crawling is no longer under debate, understanding how force is generated by organized growth of actin networks is very unclear. How is actin network growth coupled to force generation? What happens to growing actin networks when crawling cells encounter movable barriers? Measurement of the force generating ability of growing actin networks in order to better understand cell motility is the primary focus of this dissertation.

1.2.3 Cell motility and disease

The section above regarding cell motility introduced actin network growth as the driving force for protrusive extension, which is a fundamental process in cellular function. In addition, numerous clinical pathologies involve deficiencies in unregulated cell movement and perhaps actin-based protrusion. Moreover, the largest poultry recall in US history in 2002 was caused by an outbreak of *Listeria monocytogenes* (*Listeria*), a bacterial parasite that hijacks the host cell's actin motility machinery and uses it to spread within the host organism while avoiding immune system detection *(18)*.

A clinical pathology directly related to immune cell motility is the Wiskott-Aldrich syndrome. This disease is characterized by mutation of the Wiskott-Aldrich syndrome protein (WASP), a protein that is instrumental in forming the growing actin networks that are critical for leading edge protrusion during cell motility *(19)*. As such, diminished ability for immune cells (like macrophages and neutrophils) to actively pursue pathogens and foreign species in the body causes immune system dysfunction and increased susceptibility to infections *(20)*. Another pathology related to motility is metastatic cancer. Tumor spreading via metastatic cell motility is a well-documented phenomenon, but it is unclear if, or how, cell crawling is upregulated *(21)*. While some metastatic cancer cells exhibit hyper-activated motility, the underlying reasons for this behavior are still unknown *(22, 23)*. Is actin network growth also hyper-activated? Does network growth produce greater force during metastasis? Fundamental biophysical studies of actin network growth could potentially shed light on the details of metastatic cell motility.

Finally, in solid tumors such as in breast cancer, tissue in symptomatic patients often exhibits a different texture and stiffness. Because tissue is composed of cells and their surrounding matrix, the stiffness of individual cells, which is largely determined by the organization of the actin cytoskeleton, will undoubtedly affect the mechanical properties of the tissue *(24)*. While the material presented in this dissertation does not specifically address disease related questions, understanding the biophysics of cell motility and the cytoskeleton, in general, may provide a more quantitative link between clinical symptoms and disease.

1.3 Cellular actin networks

Actin networks, and specifically growing dendritic actin networks, have been shown to produce forces required for cell motility among other processes *(25)*. In addition to cell crawling, it has been postulated that dendritic actin networks actively generate forces in many other cellular processes involving shape changes (morphogenesis) such as endocytosis *(26, 27)*, phagocytosis *(28)*, and exocytosis *(29)*. The section that follows provides biochemical background and introductory material on actin networks in cells with particular emphasis on dendritic actin networks.

1.3.1 Actin biochemistry

Actin is a 43 kDa protein molecule (~5.4 nm in diameter) present in the cytoplasm that interacts with more than 60 other classes of proteins in eukaryotes *(30)*. Under appropriate conditions (high salt, physiological pH) *in vitro*, individual actin monomers (G-actin) will spontaneously form dimer and trimer nuclei that grow into

helical filaments (F-actin). Nucleus formation is very unfavorable and is the rate-limiting step for filament creation in pure actin solutions. Individual filaments are composed of two protofilament strands that form a right-handed helix with biochemical polarity. Actin filaments are ~ 6 nm in diameter with a helical pitch of ~ 30 nm *(31)*.

Actin filaments grow by individual monomer addition to either the barbed or pointed end. The barbed (or plus) end is fast-growing while the pointed (or minus end) exhibits slower growth. Polymerization kinetics of actin monomers at both ends is dependent on the ionic strength of the surrounding buffer as well as the hydrolysis state of the nucleotide (ATP or ADP) bound to the G-actin molecule *(32)* (Figure 1.2). For ATP-bound G-actin, monomer association at the barbed end is 8.3 fold greater than dissociation, and at the pointed end association is 1.6 fold greater than dissociation. For ADP-bound G-actin, monomer dissociation at the barbed end is 1.9 fold greater than association, and at the pointed end dissociation is 1.7 fold greater than association *(32)*. From these ratios, it can be seen that ATP-bound G-actin is favored to associate whereas ADP-bound actin is favored to dissociate. These dynamics coupled with absolute rate constants for the ATP- and ADP-bound monomer kinetics at each end favor ATP-bound G-actin addition to the barbed end and ADP-bound subunit dissociation from the pointed end. This creates a situation whereby filament growth primarily occurs at the barbed end and shrinkage happens at the pointed end *(33)*. The monomer on and off rates at each end of the filament k_{on}^{p}, k_{off}^{p}, k_{on}^{b}, and k_{off}^{b} define a quantity called the critical concentration, $K_c = \frac{k_{off}^{b} + k_{off}^{p}}{k_{on}^{b} + k_{on}^{p}}$, which determines the G-actin concentration above which filaments grow and below which filaments shrink. K_c for ATP-bound G-actin at the

barbed end is ~ 120 nM, 600 nM for the pointed end, and 170 nM for the filament *(32)*. K_c for ADP-bound actin at the barbed end is ~ 1.9 μM, ~ 1.7 μM at the pointed end, and ~ 1.9 μM for the filament. Because ATP hydrolysis occurs after monomer intercalation, at an ATP-bound G-actin concentration just above K_c for the barbed end (~ 130 nM), filaments will add ATP-bound monomers to the barbed end at exactly the rate that ADP-bound subunits dissociate from the pointed end such that the filament length does not change. This process where monomers cycle through a filament as the bound nucleotide is hydrolyzed while the filament length is unchanged is called treadmilling *(31, 34)*.

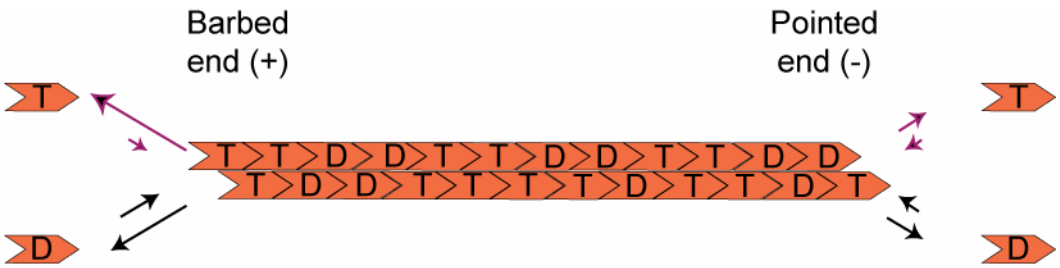

Figure 1.2 Actin filaments grow and shrink at their ends by monomer addition.

Actin filaments contain both ATP (T) and ADP (D) subunits. Polymerization kinetics for both T and D subunits at the barbed end are faster (larger arrows) than at the pointed end (smaller arrows).

1.3.2 Functional actin networks

Numerous proteins interact with both G-actin and F-actin cytoskeletal networks in cells to regulate filament assembly and organization. For example, nucleation (and assembly) of actin filament networks is extremely well regulated by proteins such as Thymosin β4, which binds to and sequesters G-actin to prevent assembly into filaments, and profilin, which binds to G-actin and permits barbed end elongation but not nucleation *(33)*. Filament interacting proteins such as capping protein and ADF/cofilin interact with

barbed ends to stop elongation and destabilize filaments, respectively *(33, 35)*. In addition branching, crosslinking, severing, and bundling proteins regulate filament architecture to organize filaments into particular structures for different cellular processes. Figure 1.3 artistically shows a subset of different actin networks found in cells along with the function/process that is performed.

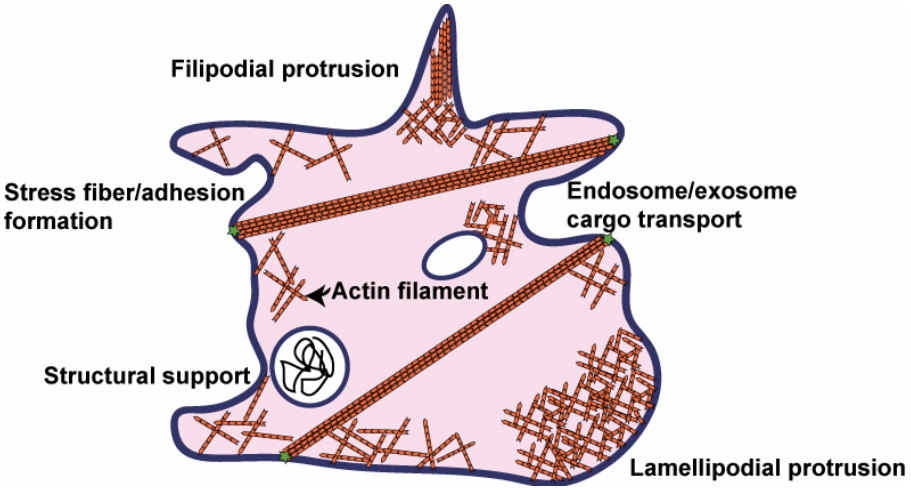

Figure 1.3 Illustration showing different actin network structures and corresponding behaviors.

Organization of the actin filaments varies as cells perform different functions, ranging from lamellipodial protrusions used during motility to stress fibers cables used during adhesion formation.

As shown, actin networks are organized into specific structures for performing different tasks. From bundled actin filaments in stress fibers, often seen in cells bearing tensile loads, to crosslinked and branched networks in lamellipodial protrusions, actin network organization is tightly coupled to its function. The structure-function relationship for the actin cytoskeleton is just beginning to receive attention in terms of understanding how network organization relates to the ability for the network to support different loading conditions *(36, 37)*.

1.3.3 Dendritic actin networks in crawling cells

In the lamellipodia of crawling cells highly branched and crosslinked growing dendritic actin networks provide power for protrusion during cell motility. The canonical example of a crawling cell is the fish epidermal keratocyte, a wound healing cell, which has large (~10 μm x ~2 μm) and flat (~100 nm thick) lamellipodium that contains growing actin filaments organized into a dendritic actin mesh. Individual filaments in this network range from ~ 100 nm – 1 μm in length *(38)*, and their organization with respect to neighboring filaments is well controlled through a host of actin binding proteins. More than 40 years of biochemical research has produced significant progress towards understanding the process of dendritic network formation and maintenance (and is nicely summarized in reference *(35)*). This information has been compiled into the "dendritic nucleation model" for actin network growth (Figure 1.4).

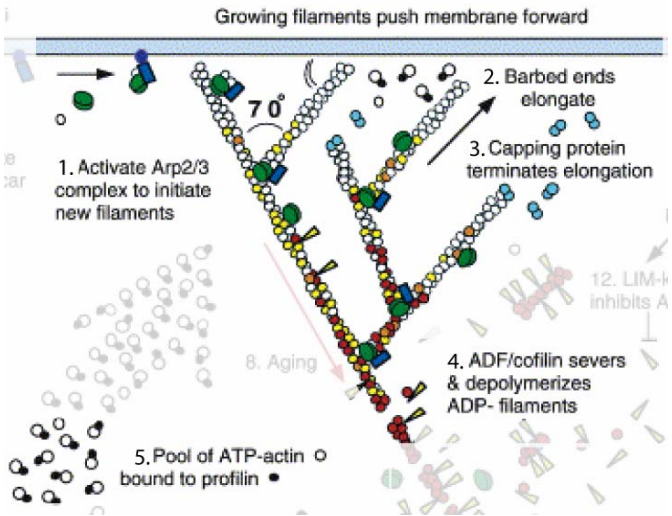

Figure 1.4 Dendritic nucleation model for actin network growth in the lamellipodia of crawling cells. Dendritic actin networks contain short, highly branched filaments with their barbed ends oriented towards the membrane such that filament elongation pushes the membrane forward. Image is modified from reference *(30)* and certain steps have been grayed to emphasize steps 1-5.

A detailed explanation of this model is available in numerous review articles *(30, 33, 35)*. The key proteins involved and a summary of steps 1-5 of this model below will provide a working framework relevant for this dissertation.

Key proteins

Arp2/3 complex

This protein is a seven subunit complex that nucleates new actin filaments in the form of branches off existing filaments in a network *(39, 40)*. Nucleation of filaments via this pathway is thought to be the primary source of growing filaments that produce force during cell motility and occurs at a much higher frequency than spontaneous nucleation of filaments *(35)*. In order to nucleate a daughter filament, the Arp 2/3 complex forms a quaternary complex with a nucleation promotion factor (NPF), a G-actin monomer, and an actin filament. This interaction ultimately results in the creation of a new filament with its barbed end at a 70° angle with respect to the mother filament barbed end. Continued Arp2/3-based nucleation leads to a dendritic array of filaments with their barbed ends oriented at a 45°-55° with respect to the cell membrane *(30)*. In addition to nucleating new filaments, the Arp2/3 complex caps pointed ends of filaments to prevent depolymerization and permit stable barbed-end elongation *(41)*.

NPF

NPFs are a class of proteins that activate the Arp2/3 complex to initiate the formation of a new branch in a dendritic actin network. Since de novo nucleation of actin filaments starts with NPFs activating the Arp 2/3 complex, NPFs have two interesting

properties: 1) they essentially regulate new filament production in the lamellipodia of crawling cells, and 2) activated NPF localized to the membrane is the only requirement for the formation of a dendritic network in the cytoplasm. The pathogenic bacterium *Listeria* uses this second property to hijack the host cell actin machinery and spread during infection *(18)*. *Listeria* expresses a constitutively active surface-bound NPF, ActA *(42)*, which catalyzes formation of a growing actin network that propels them throughout the host-cell cytoplasm. This property was further extended by Cameron *et al*. who showed that polystyrene beads non-specifically coated with ActA exhibited actin-based motility similar to *Listeria* when immersed in cell-free extract from *Xenopus laevis* oocytes *(43)*.

In addition to bacterial ActA, mammalian NPFs including WASP, N-WASP, Scar/WAVE1, Scar/WAVE2, and Scar/WAVE3 *(40)*, Las17p (yeast) *(19, 35)*, and RickA (Rickettsia) *(44)* also activate the Arp 2/3 complex to create new filaments in a dendritic network. The mammalian NPFs differ from ActA in both protein domain organization and the requirement for upstream signaling in order to activate these proteins before they can catalyze new branch formation. In crawling cells, NPF molecules are activated at and localized to the cell membrane by specific lipids in the membrane (PIP_2) and membrane-bound GTPases (CDC42) *(45)*, which necessitates that most (if not all) branching takes place near the load surface.

Capping protein

Capping protein is a two-subunit heterodimer whose primary function is to prevent barbed-end elongation *(46)*. This keeps filaments short and helps localize

filament branching to the load surface. In addition, capping protein also has a secondary function of nucleating filaments that elongate from their pointed ends rather than barbed ends. This occurs because capping protein is thought to resemble a stable actin dimer that has a higher affinity for a G-actin monomer than the affinity between two individual monomers during formation of a typical filament nucleus. These capping protein-actin complexes then elongate from their pointed ends because the barbed end of the bound actin is capped by capping protein *(47)*.

ADF/cofilin

This family of proteins is thought to destabilize actin filaments by physically changing the twist of the actin helix upon binding *(48)* and by promoting release of phosphate from the nucleotide binding pocket of actin *(46)*. By actively severing filaments and exposing an ADP-actin subunit, ADF/cofilin helps to keep the monomer pool replenished for further network growth. Exposed ADP-actin subunits depolymerize much faster than ATP-actin monomers *(32)* so severing leads to subsequent depolymerization. A recently discovered function of this protein is generation of new barbed ends as a result of filament severing. This has been proposed as another method to generate new growing filaments in a dendritic network *(49)*.

Profilin

The primary function of profilin is to exchange ADP for ATP in actin monomers recently removed from the network *(50)*. In addition, profilin-bound G-actin can only elongate existing barbed ends and is unable to participate in filament nucleation.

Together with cofilin, these two proteins form a recycling system to help to keep the monomer pool replenished for sustained network growth as profilin-bound monomers elongate existing filaments *(51)*.

Dendritic nucleation of actin networks

In order to develop the highly branched dendritic structure seen in the lamellipodia of crawling cells, the Arp 2/3 complex must be activated by a NPF, which is localized to the leading edge, to nucleate new actin filaments from existing filaments *(52, 53)*. Once nucleated, the daughter filament is anchored to the side of the mother filament by its pointed end via the Arp 2/3 complex, and both filaments grow from their barbed ends pushing the membrane forward until capping protein terminates further elongation (by associating with free barbed ends). Hydrolysis of ATP in G-actin subunits and ejection of the inorganic phosphate after ~ 350 s is a timer that marks subunits as primed for disassembly *(30)*. ADP-actin subunits are severed/disassembled by (ADF)/cofilin, and severed filaments subsequently depolymerize as they contain primarily ADP-actin subunits (that favor dissociation). ADP-bound G-actin binds to profilin, which catalyzes exchange of ADP for ATP, and these "recharged" monomers replenish the pool of competent actin for further assembly *(46)*. Figure 1.4 shows how these steps are believed to occur during cell crawling.

It is clear that significant progress has been made towards understanding the biochemical maintenance and hierarchical assembly of dendritic actin networks. However many open biophysical questions remain unanswered. What is the mechanism of protrusive force generation? How do external forces couple to the biochemical

pathways in the dendritic nucleation model? What is the rate limiting step in new filament creation? What role do additional crosslinking proteins play in force generation? Do all filaments in the network cooperate to produce force or do some push and others pull? Biophysical studies aimed at investigating the influence of external load on network growth dynamics and structure, which is the focus of this dissertation, will help elucidate how physical signals are transduced by these biochemical reactions.

1.4 Force generation by actin network growth

Force generation by polymerizing actin networks has been postulated for many years, but pioneering theoretical work by Hill and Kirschner showed that filament growth was capable of producing usable energy *(54)*. The sections that follow present a summary of recent experimental measurements of force generation by growth of individual actin filaments and dendritic networks in conjunction with an overview of theoretical developments to explain network force generation.

1.4.1 Force generation by single actin filaments

The basic idea of performing mechanical work by actin filament growth was proposed by Hill and Kirschner in 1982. They posited that the free energy released by monomer association could be used to displace a load. This theory predicted that the polymerization rate (v) of a single filament would decrease with opposing force (f) as $v \sim e^{-f}$. It also predicted that the stall force (force where $v = 0$) of a single filament should scale with the negative logarithm of monomer concentration *(54)*.

Force generation measurements on individual, growing actin filaments *in vitro* have proven experimentally challenging. To date only two measurements have been reported. Footer *et al*. measured the polymerization force of actin bundles containing ~ 8 filaments using an optical trap, and they used phenomenological observations to argue that the stall force was supported by a single filament. Their measurement of the stall force at 2 μM actin, f_{stall} ~ 0.8 pN, was consistent with the theoretical predictions described above. However, their measurements at higher concentrations were confounded by potential Euler buckling of the actin filament prior to stalled growth *(55)*.

In another measurement of single filament polymerization forces Kovar and Pollard used a filament-tethering geometry to hold a growing filament between two attachment points *(56)*. By measuring the length of the filaments as they grew, and observing filament buckling, they calculated a lower bound on force generation of ~1.3 pN at 0.5 μM actin *and* 20 μM phalloidin. This value is inflated because phalloidin, a small peptide, stabilizes actin filaments and noticeably increases the bending rigidity by 2-fold, which correspondingly increases the buckling force by 2-fold *(57)*. While these measurements together show consistency with the stall force scaling concept presented by Hill and Kirschner *(54)*, a direct measurement of individual filament polymerization velocity in response to external force is still lacking. This measurement will provide valuable insights into the mechanism by which polymerization performs mechanical work.

1.4.2 Theoretical developments

In the pioneering work by Hill and Kirschner, the energetic cost of filament elongation against a load manifests as a reduction in the chemical potential for monomer intercalation in the filament *(54)*. Building on these ideas, Peskin *et al.* proposed a Brownian ratchet microscopic mechanism for physically extracting mechanical work from a polymerizing actin filament. In this model, hereto referred to as the Brownian ratchet, the filament is anchored at one end by a rigid actin network and abutted against a load surface at the other. The load diffuses in-and-out of contact with the filament, with monomer addition occurring once a space large enough to fit an additional monomer (2.7 nm) between the filament and load exists, thereby rectifying the Brownian motion of the load surface *(58)*. The energy source for rectifying the random walk of the load is the same binding energy used in the formulation by Hill and Kirschner not the energy from ATP hydrolysis *(59)*. In the Brownian ratchet model, the bottleneck for filament growth and generation of mechanical work rests primarily on the probability that the load surface will diffuse over a sufficient distance against the applied force if the polymerization rate is slow compared to diffusion of the load.

Refining the original Brownian ratchet model, Mogilner and Oster have since developed two related incarnations with added complexity based on a slew of biochemical and biophysical data on dendritic network growth *(43, 60-62)*. The conceptual advance provided by the Elastic Brownian ratchet was the inclusion that, "free" filament ends ~ 30-100 nm in length were allowed to fluctuate in addition to the load to contribute towards generating space for monomer intercalation. In addition, this model incorporated an angular dependence on the force generation by and polymerization

velocity of a growing filament *(60)*. In the most recent version of this model, the Elastic *tethered* Brownian ratchet, a formalism was added to incorporate findings that the actin network is tethered to the load while it concurrently applies a propulsive force *(61, 62)*.

An alternative microscopic mechanism proposed by Dickinson and Purich posits that filament end-tracking motors adhered to the load surface alternately bind and unbind monomers in the network depending on the state of the bound nucleotide. This mechanism allows for use of the energy available from ATP hydrolysis (as compared to just monomer binding) for force generation and is able to capture the stepping behavior of *Listeria (63)* (5.4 nm discrete steps) as well as the adhesion of the network to the load *(64)*. However, the identity of the clamping motor is not identified, and this model does not explain a 2.8 nN attachment force between the actin network and load in a recent experiment performed with 5 pure proteins – none of which is considered an end-tracking motor – where polymerization forces were greater 4 nN *(65)*.

Mesoscopic models that treat entire network growth rather than individual filament growth attempt to explain force generation and actin-based motility as resulting from elastic energy stored in the actin mesh *(66)* and from active network remodeling with increasing load *(67)*. In the elastic gel model, actin polymerization at the surface of *Listeria* stretches the existing dendritic network, which results in an accumulation of elastic stress in the gel. This elastic stress is relieved by forward movement of the bacterium. In this model, actin polymerization is simply a means for developing stress in the actin gel, which in turn provides the energy for pushing the load. While this model accurately predicts network force generation on *Listeria* and NPF-coated beads, it does

not treat to force generation in the lamellipodium of crawling cells or against flat surfaces.

The autocatalytic model proposed in reference *(67)* predicts that actin network growth pushes the load at a constant velocity regardless of opposing force. A competition between filament branching from existing filaments in the branching zone, a localized region close to the load surface, and uniform capping throughout the network regulates the number of force generating filaments in the network. As filaments are capped, they gradually leave the branching zone (because of continued forward movement by the load) and are no longer substrates for nucleation of new branches. In this model, capping and branching maintain a constant average force per filament and thus the polymerization rate is also constant. Individual filaments transiently experience changing loads, but it is unclear what determines the "set point" force that determines the steady-state filament polymerization (and load) speed *(67)*.

1.4.3 Force generation by dendritic actin networks

Propulsive force generation by growing actin networks has received significant attention in the past 10-15 years once it became clear that actin network growth was generating the propulsive force during cell crawling and *Listeria* pathogenesis *(68)*. Attempts to measure the network growth velocity as a function of external force have proven an easier task than for individual filaments, though it is more difficult to ascribe force generation to a simple mechanism because of the complexity of networks. Lower bound estimates of dendritic actin network force generation ($f \sim 4$ nN) were provided

from studies where lipid vesicles were deformed and propelled through cell-free extract *(69, 70)*.

Experiments by McGrath *et al*. were the first to measure load velocity as a function of external force. They found that *Listeria* propulsion speed in cell-free extracts decreased considerably as the viscoelasticity of the extract was increased with methylcellulose (a viscoelastic polymer). Increasing the viscoelasticity of the solution increased the drag coefficient of *Listeria* and their actin tails, which resulted in slower movement under increasing drag forces *(71)*. Though propulsion was slowed by more than 20-fold, bacterium movement was never stalled at the largest opposing forces (f_{max} ~200 pN) in these experiments. A contrary result by Wiesner *et al*. showed that NPF-coated beads propelled by dendritic actin networks formed in purified proteins did not show a significant speed reduction over a similar range of viscosity *(72)*. While instrumental as the first demonstrations of actin network force and growth velocity measurements, both studies lacked the ability to actively apply forces to the network or yield nanometer-level details of motion. Furthermore, with this experimental platform, it is impossible to directly exert arbitrary forces on the network and ask the question: how fast will this network grow?

This shortcoming was addressed by Marcy *et al*. as they developed a system capable of applying forces up to 4.7 nN to a NPF-coated bead with a microneedle force microscope while measuring network growth velocity with video microscopy *(65)*. Once again however, network growth was not stalled in this study, and these measurements were performed with limited spatial resolution. Nonetheless, this study provided direct evidence for nN scale force generation *(65)*. These results were compared to predictions

from the elastic gel model, and the theory was well supported by the observed growth dynamics.

A recent study from our group revealed that Brownian motion of NPF-coated beads is correlated with the velocity of actin-propelled beads. Using laser-based tracking of individual beads, Shaevitz and Fletcher showed that an effective increase in viscosity near the walls of a microscope fluid chamber, reduced the Brownian motion of the beads substantially and resulted in a lower propulsion velocity *(73)*. This finding supports the ideas presented by Peskin *et al*. in Brownian ratchet model.

The AFM investigation of actin network growth presented in Chapter 4 of this dissertation is the first measurement of network stall and demonstrated that loading history affects the network growth velocity *(74)*. This study showed that network growth velocity was constant under increasing loads consistent with the autocatalytic model presented by Carlsson *(67)*. These results will be expounded upon later in this dissertation and will not be discussed further at this time. A summary of the experimental work on force generation by dendritic actin networks and by individual filament growth and the corresponding supported model is provided in Table 1.1.

Experimental platform	Network or filament	Major findings	Model supported	Reference
Timelapse imaging of *Listeria*	Dendritic network	Velocity slowed significantly with increased viscosity and drag force	Elastic tethered Brownian ratchet	McGrath *et al*., 2003
Timelapse imaging of NPF-coated beads	Dendritic network	Velocity was independent of increase in viscosity so force must be in nN range	Elastic gel	Wiesner *et al*., 2003
Timelapse imaging of deformable lipid vesicles	Dendritic network	Total force exerted by network on vesicle is computed as ~ 1nN	None	Giardini *et al*., 2003; Upadhyaya *et al*., 2003
Microneedle force microscopy on NPF-coated beads	Dendritic network	Measured nN force production and actin network growth velocity from spherical beads	Elastic gel	Marcy *et al*., 2004
AFM measurement on NPF-coated cantilever	Dendritic network	Demonstrated mechanical stall of actin network and loading history dependence	Autocatalytic growth	Parekh *et al*., 2005
Laser tracking of NPF-coated beads	Dendritic network	Viscosity affects Brownian fluctuations of bead motion and propulsion velocity	Brownian ratchet	Shaevitz and Fletcher, 2007
Optical trapping of acrosomal bundle	Filament	Stall force measurements of single filaments obeys the principles proposed by Hill and Kirschner	Hill and Kirschner	Footer *et al*., 2007
Timelapse imaging of filament growth	Filament	Filaments buckle at forces below the stall force	Hill and Kirschner	Kovar and Pollard, 2005

Table 1.1 Summary of force measurements on actin filament and dendritic network growth.

It is likely that a combination of continuum gel-based theories and microscopic models of filament growth are both relevant to steady-state force generation by dendritic actin networks, but only the autocatalytic theory presents a dynamic coupling between growing filaments that push the load and new filament creation. Questions regarding how filament density changes with load and the influence of surface curvature on force

generation remain largely unanswered. Furthermore, if the network can mechanically adapt to increasing loads as suggested by Carlsson, what is the rate limiting step in filament creation? What protein complex provides the internal "friction" in the elastic gel and elastic tethered Brown ratchet? How does the stall force of dendritic network growth scale with the area of the nucleation surface? This dissertation sheds light on the affect of load on actin network structure and growth velocity.

1.5 Actin network mechanics

Often considered an ideal semiflexible polymer because of its intrinsic physical properties and physiological filament lengths individual actin filament and whole network mechanics have received considerable attention from both physicists interested in polymer physics and biologists interested in cellular structure. The sections that follow will briefly introduce the polymer physics and actin rheology fields.

1.5.1 Actin filaments are semiflexible polymers

Actin filaments are polymers composed of noncovalently bound monomer subunits. Each monomer in a filament is bound to its neighboring monomers through the same interactions (neglecting the two end monomers), and it is the nature of these interactions that gives these filaments their mechanical rigidity. Based on the thermal fluctuations of individual actin filaments, it was shown these filaments have a persistence length, $L_p \sim 17$ μm *(75)*. The persistence length of a polymer chain defines the length over which correlations in the direction of the tangent to the chain are lost when at thermal equilibrium. In other words, for length scales below L_p the polymer behaves

more like an elastic rod whereas at longer length scales, it assumes a random walk. Because actin filaments are very well regulated for different cellular functions, a range of filament lengths, called their contour length, L_c, as low as ~ 100 nm and as large as ~ 70 μm *(76)* is seen *in vivo*.

A common metric for classifying a polymer is the ratio L_c / L_p. When this ratio is much greater than unity, the polymer is considered flexible and when the ratio is much less than unity, the polymer is considered rigid. Actin filaments lie at a point where the ratio is ~ 1 so they are considered "semiflexible". As an example, DNA has an L_p ~ 50 nm *(77)* and is classified as a flexible polymer under physiological conditions, and thermal fluctuations dominate its mechanical resistance to deformation. Microtubules polymers have a persistence length of order mm are examples of rigid biopolymers *(75)* whose resistance to deformation is dominated by bending and compression. While the mechanics of flexible polymer gels and rigid polymers networks are relatively well understood *(78)*, resistance to deformation of semiflexible networks is much less understood. For actin filaments under physiological conditions $L_c / L_p \sim 1$, both thermal fluctuations and the bending stiffness of individual filaments contribute substantially to the overall mechanical response, which is not the case for flexible or rigid polymers where only one or the other is dominant.

1.5.2 Rheological studies of actin networks

Rheology of polymer networks is often used to measure their linear frequency dependent viscoelasticity and non-linear viscoelasticity at increasing loads. In cells, it is

now well accepted that actin networks are the major load bearing element of the structural cytoskeleton *(79)*. The mechanical properties of actin networks have been studied over a wide range of frequencies at the cellular level *(80, 81)* and in purified mixtures *in vitro (82-85)*. Though this section will focus on mechanical property measurements of actin networks, recent reviews by Janmey and Weitz offer more information on whole cell mechanics *(79, 86)*.

A common approach for investigating the viscoelasticity of actin gels has been performing rheological studies on purified solutions containing actin and selected actin-binding proteins in "bulk" assays – mixtures of purified proteins measured as equilibrium solutions *(83, 87)*. Rheology measures the material response to given stress or strain and yields values for the storage (elastic) modulus *G'* and the loss (viscous) modulus *G"* at various frequencies (Figure 1.5).

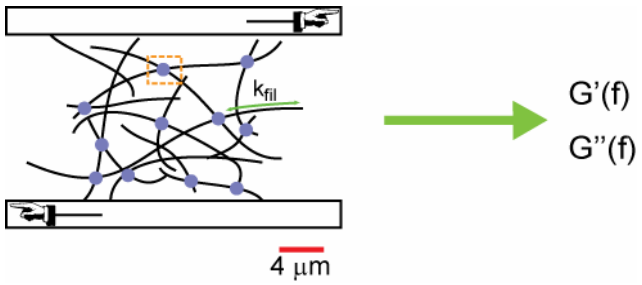

Figure 1.5 Schematic illustration of bulk rheology assays.

Actin filaments (black curved lines) and crosslinking proteins (blue circles) are mixed in solution and placed between two plates that are sheared (arrows) with respect to each other. Imposing a deformation on the network and measuring the resulting stress yields measurements for the shear moduli *G'* and *G''*.

Such studies have led to significant advances in understanding the mechanical role of various crosslinkers *(88-90)*, and of how the elasticity of in vitro networks scales with

concentration of different proteins, including actin itself *(91)*. Recently, Gardel and colleagues presented findings showing that actin filaments that are bundled or weakly crosslinked with scruin, an irreversible and rigid crosslinking molecule, exhibit mechanics dominated by resistance to deformation of the individual actin filaments *(83)*. This and other studies have proposed that individual actin filaments are essentially entropic springs that stress-stiffen with increasing strain primarily as a result of the resistance to extension expected from a wormlike chain polymer *(77, 83, 87)*.

While extremely useful for understanding the fundamental physics of semiflexible polymer melts, these experimental platforms primarily investigate actin networks with a random architecture that does not resemble those seen *in vivo* during dynamic processes such as motility *(36)*. As shown in Figure 1.3, actin networks exhibit dramatically different organization for specific processes. For example, at the leading edge of a crawling cell, dendritic actin networks are formed through the carefully regulated action of actin binding proteins (as described in section 1.3.3). They are different in several ways from the actin networks studied in bulk assays: they are non-equilibrium, dynamic, and display a very specific dendritic architecture (short, branched, and crosslinked filaments) that is intimately linked to their ability to generate directional forces *(35)*. Recent work by Mizuno *et al*. has commented on the behavior of non-equilibrium actin networks and shown that active stretching of filaments by myosin minifilaments results in different frequency scaling behavior for the elastic modulus than expected for semiflexible polymers at equilibrium *(92)*. Other studies have investigated the viscoelasticity of stress fibers, which are actin rich cables formed during cellular adhesion to the underlying substrate. Stress fibers contain parallel actin filaments held

together by myosin minifilaments. The Young's (tensile) modulus of these assemblies was found to be 1.45 MPa, which is more than 1,000,000 fold greater than the moduli reported from bulk rheology assays of purified actin networks *(93)*. Furthermore, cellular elasticity is ~ 1kPa whereas the elasticity of purified actin networks is generally 1 – 10 Pa. These results demonstrate that many parameters such as loading direction and filament organization, or architecture, strongly affect the mechanical properties of actin networks. Therefore, it is unclear how different actin structures will respond to a given deformation.

1.6 Atomic force microscopy in life science

Building on the ideas and principles of the scanning tunneling microscope, which was used to measure charge distributions and nanometer scale features of a specimen but required conductive materials for both the probe and specimen, the AFM has seen a consistent gain in popularity in recent years. Though initial versions of AFMs still employed tunneling detection on top of a microcantilever (hereafter called cantilever) probe *(94)*, significant technical innovation has lead to a wide array application to life sciences. AFM has received increasing attention from biologists, physicists, and engineers interested in answering questions about molecular forces and the sizes of biomolecules because of the biocompatibility of the technique: aqueous solutions, and physiological temperatures. The sections that follow will briefly introduce the basic concept of AFM and describe some popular applications of AFM in biology.

1.6.1 Atomic force microscopy concept

AFM uses cantilever beams as physical probes to measure atomic scale forces and dimensions of a sample, and in turn, can be used to manipulate features of delicate samples. Similar to classical Hookean springs, the deflection of a cantilever is linearly related to the applied force for small deflections (up to ~10% of its length). Deflection is typically measured with the optical level method in which a laser is focused onto the end of a cantilever, and the position of the reflected beam on a position sensitive photodiode (a segmented photodiode is shown in Figure 1.6) gives the displacement of the cantilever *(95)*. The force exerted on a sample is calculated by measuring the deflection of the cantilever and multiplying by the spring constant, k_{cant}, of the cantilever (Figure 1.6).

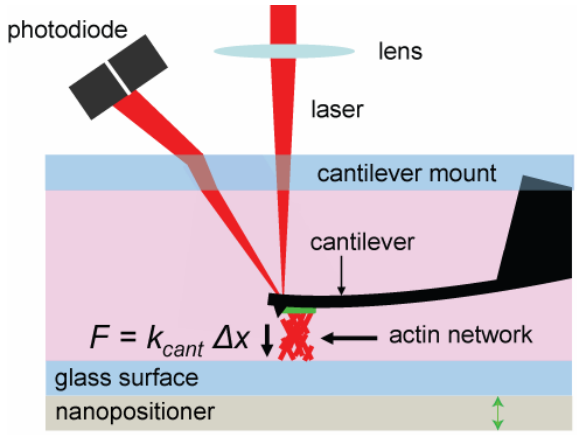

Figure 1.6 Schematic of AFM measurement of actin network growth.

Deflection of the cantilever (Δx) is observed by monitoring the position of the reflected laser on the segmented photodiode. By measuring the deflection of the cantilever and knowing k_{cant}, the force exerted on the sample can be calculated using Hooke's law as $F = k_{cant} * \Delta x$.

The stiffness of a cantilever beam varies with its geometry as $k_{cant} \propto E \frac{t^3 w}{l^3}$ where E is the Young's modulus of the material, t is thickness of the beam, l is the length of the

beam, and w is the width of the beam. Typical values for cantilevers used in biological applications ($l \sim 100$ μm, $w \sim 10$ μm, $t \sim 500$ nm, and $E \sim 200$ GPa) yield spring constants that range from 10 pN/nm - 1 nN/nm. This stiffness range allows measurement of forces from pN well into the nN regime, giving AFM a large dynamic range compared to other force measurement techniques *(96)*. A thorough analysis of the beam physics and other phenomena that affect the dynamic range in AFM measurements is discussed in reference *(97)*.

1.6.2 Atomic force microscopy applications in biology

Because of the large force range and its compatibility with many environments from ultra-high vacuum to aqueous surroundings, AFM has found extensive use in fields from semiconductor processing and inspection to single molecule biophysics. Applications in biology include force spectroscopy measurements of the intra-molecular forces that hold protein molecules together *(98, 99)*, cellular elasticity measurements *(100, 101)*, imaging of biomolecules such as DNA on solid supports *(102)* as well as protein receptors in cell membranes *(103)*, and receptor-ligand binding forces *(104, 105)* among many others.

In typical force spectroscopy measurements, a single protein molecule (such as titin *(106)*) is stretched between the cantilever and bottom surface by moving the bottom surface away from the cantilever tip at a known rate *(98)*. The information from these experiments is used to derive information about the equilibrium kinetics for the protein folding and unfolding rates. Similar experiments where a ligand is attached to the cantilever tip and receptors are anchored to the bottom surface provide the ability to

measure the binding strength between complementary molecules such as antibodies and antigens *(104)*. AFM measurements of cell mechanics monitor deflection of the cantilever as a cell is indented with the cantilever. By measuring the so-called force-indentation curves and using appropriate theory, it is possible to determine various mechanical moduli of the cell *(101)*.

Because dendritic actin network growth was previously shown to produce nN forces *(65)* and AFM possesses both the ability to exert forces from ~ 10 pNs to ~ 100 nNs and measure nanometer-scale displacements, it is an appropriate technique for investigating actin network force production. The nanometer-scale resolution is extremely useful for performing rheology of dendritic networks and studying network growth dynamics. While AFM is well-suited for the actin network studies presented in this dissertation, it is not suitable for measuring motion of single molecule motors or low force unfolding kinetics of proteins due to the large drag coefficients (and subsequent limited force resolution) of AFM cantilevers *(96)*. Further information about AFM applications in biology can be found in reference *(107)*.

CHAPTER 2: BUILDING AN ATOMIC FORCE MICROSCOPE

2.1 Introduction to atomic force microscopy construction

Chapter 1 briefly introduced the idea and concept of an AFM and described typical life science applications. This chapter discusses the issues one should consider when constructing a custom AFM. First and foremost, DO NOT build a custom instrument if a commercial alternative is adequate for your purposes and there is sufficient funding (~ $250,000) for such an instrument. While I firmly believe that all PhD students in Bioengineering/Biophysics should obtain experience with sensitive and cutting-edge equipment, sometimes it's better to use what already works rather than reinvent the wheel. With that said, I have had the opportunity to build three different AFMs while in the Fletcher lab, and each experience has taught me new tricks and broadened my perspective on the design process.

With the adaptation of the scanning tunneling microscope to the AFM, where samples could be imaged and interrogated under ambient conditions and in aqueous environments as well as improvement in probe manufacturing, AFM is now a well

established biophysical and semiconductor inspection tool. In 1986, Binnig *et al*. demonstrated the first AFM by imaging insulators and inorganic materials *(94)*. Since this initial study, significant innovation by numerous academic laboratories *(95, 108-111)* and by industry manufacturers such as Veeco, Park Scientific, and Asylum has helped AFM mature into an extremely versatile technology for biological applications. The following sections are by no means a comprehensive review of AFM design or construction but are a compilation of notes and considerations for building a custom instrument.

2.2 Anatomy of an atomic force microscope

The basic setup of an AFM is shown below in Figure 2.1A. The figure below shows a typical configuration where a nanopositioner moves the sample relative to the cantilever, laser, and position-sensitive detector (PSD). This need not be the case, and in fact, the Veeco Bioscope I and II use the opposite configuration where the nanopositioner moves the cantilever and laser relative to the detector and sample. Moreover, in current generation commercial instruments from Veeco and Asylum, there are two nanopositioners: an XY positioner that moves the sample relative to the cantilever, laser, and detector, and a Z positioner that moves the cantilever, laser, and detector relative to the sample.

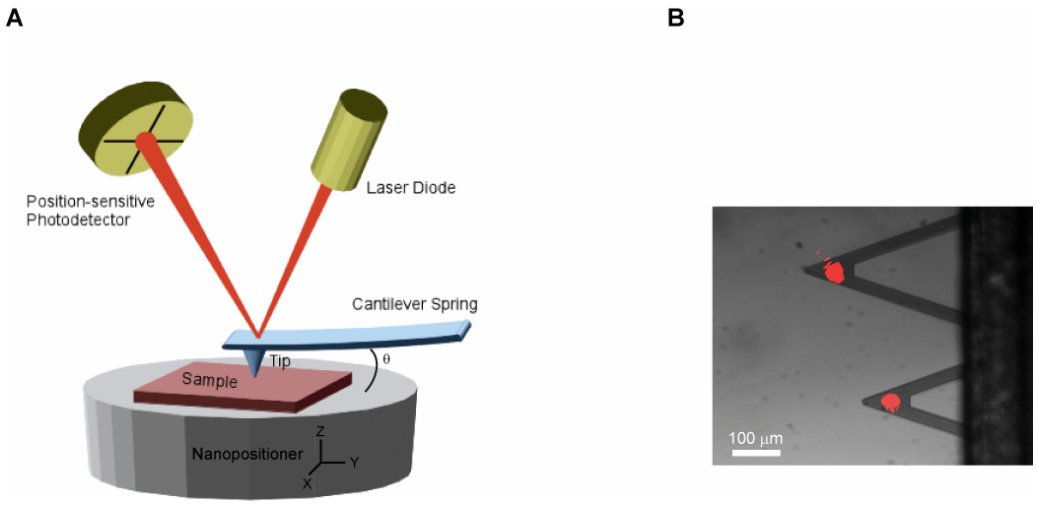

Figure 2.1 Basic AFM setup.

(A) A diode laser is focused onto the end of a microfabricated cantilever, and the reflected laser position is measured on a position-sensitive detector (PSD). The nanopositioner beneath the sample moves the sample with respect to the cantilever. As the cantilever is positioned in contact with the sample, it bends as it applies a force to the sample, and the reflected laser beam translates on the PSD surface. Drawing is modified from *(112)*. **(B)** Image showing well-contained, focused lasers on two independent cantilevers (discussed further in Chapter 3). Optimal beam alignment is accomplished when the laser spot is slightly smaller than the reflecting surface *(113)*.

2.2.1 Laser

The AFM laser can be as simple as a laser pointer (long coherence length) or as complicated as a Ti:Sapphire solid state (short coherence length) laser depending on the application. In general, the center wavelength (λ_c) and spectral characteristics should allow for a focused spot that fits well onto the free end of the cantilever (Figure 2.1B) and such that the PSD operates in a regime where the bandwidth is sufficiently high. Red/near infra-red laser diodes with λ_c between 630 nm and 785 nm and bandwidth ~ 1 nm perform more than adequately for both requirements. However, because of the narrow bandwidth of many diode lasers, their large coherence length (~ 1 m) permits

interference between the reflected beam from the cantilever with that from sample when using an uncoated silicon nitride cantilever. This interference is seen as a periodic signal on the PSD with periodicity $\lambda_c/2n$ (where n is the refractive index of the medium) in the Z direction as the distance between the cantilever and sample is changed *(114)*. Interference fringes can often persist over significant distances (beyond 10 μm from the contact point between the cantilever and sample). The fringe pattern leads to errors in determining the true contact point during sample approach and release, which is very important in a number of applications. A solution to this problem is using a super luminescent diode (SLD) or solid-state laser. SLDs have 50-60 nm bandwidth (but often sacrifice power), which greatly reduces their coherence length and the distance over which interference occurs. In addition, one may choose a mode-locked Ti:Sapphire (solid-state laser), with a 200 nm bandwidth, to reduce the coherence length even further but this solution is extremely expensive (over $100,000 compared with less $3000 for a high end narrow bandwidth laser diode module). Another (often less practical) solution is changing angle between the cantilever and the sample (θ in Figure 2.1A) to physically displace the two reflected beams by a greater distance at the PSD plane such that only the beam reflected from the cantilever is incident upon the detector.

In addition to interference, it is also important to use a temperature-stabilized laser. Lasers generate significant heat, which can change the dimensions of the cavity (for solid-state lasers) or the size of the band gap (for diode lasers), resulting in mode hopping. If a temperature-stabilized laser is used, this reduces problems resulting from temperature induced mode-hopping, which include power fluctuations and pointing stability errors. Numerous vendors (Blue Sky Research and Point Source for example)

offer temperature-controlled narrow bandwidth laser diode modules with reasonable laser powers (5-25 mW) for $1500 - $2500, depending on wavelength and output power desired. These modules use Peltier coolers on the diode housing to keep it at a fixed temperature. Temperature-controlled solid state lasers maintain the gain crystal at fixed temperature using a flow-based heat exchange system in the crystal housing.

Another important laser quality is the beam power. The reflected beam should be sufficiently powerful so as to generate a reasonable photocurrent in the PSD. Depending on the detector type (discussed below) and the cantilever coating, this requirement can be non-issue or quite limiting. A good rule of thumb is to purchase a laser with output power control where more than enough power can be delivered because one can always turn the power down and use neutral density filters to further reduce the power. It is important to check the output power specification with the laser manufacturer, especially when purchasing a fiber-coupled laser because vendors will occasionally quote the output power from the diode rather than the fiber.

Fiber-coupled lasers are highly desirable in AFM design because they eliminate any spatial variations in the laser beam from the diode and convert mechanical vibrations of the diode (pointing instability) into small power fluctuations (which can be eliminated with appropriate normalization). Current technology from diode-only modules is often sufficient, but a fiber-coupled source is a nice feature if available. One should not purchase a low/medium quality diode and rely on fiber coupling to compensate for poor beam quality from the diode itself. All custom AFMs in the Fletcher lab use Blue Sky Research temperature-stabilized, fiber-coupled diode lasers with the pointing stability

less than 10 μradians/°C, power stability better than 0.8% of the maximum power over 1 hour, and diffraction limited divergence as measured from the output of the fiber.

2.2.2 Position-sensitive detection

Below, two types of PSDs are discussed: segmented photodiodes and lateral effect photodiodes. The former is the more common PSD sold with commercial AFMs and much cheaper. The latter is the PSD used in all custom AFMs in the Fletcher lab for reasons discussed below.

Segmented photodiode

After the demonstration of the optical lever detection scheme by Amer and Meyer in 1988 *(95)*, this has become the industry standard method for tracking cantilever deflection. The operating principle is illustrated in Figure 2.2. As the cantilever is deflected through an angle α due to interaction with the sample, the angle of the reflected beam changes by an angle 2α, which translates the beam on the SPD. This translation shifts power between elements A and B and is detected as a change in the photocurrents generated in each element. The position of the beam is then calculated as the difference in photocurrents $I_A - I_B$. This signal is calibrated to a physical displacement using a nanopositioner to control the deflection of the cantilever. In signals and systems, typically one measures voltages rather than current so the photocurrent from each element is first converted into a voltage using a standard transimpedance amplifier (discussed below), and the voltage difference is the quantity actually measured. Under optimal conditions, this detection scheme can resolve a 100 nm displacement of the

beam, which corresponds to sub-nanometer displacements of the cantilever when the detector is placed in the far field of the laser reflected from the cantilever surface. This sensitivity is sufficient to monitor thermally driven deflections of the cantilever.

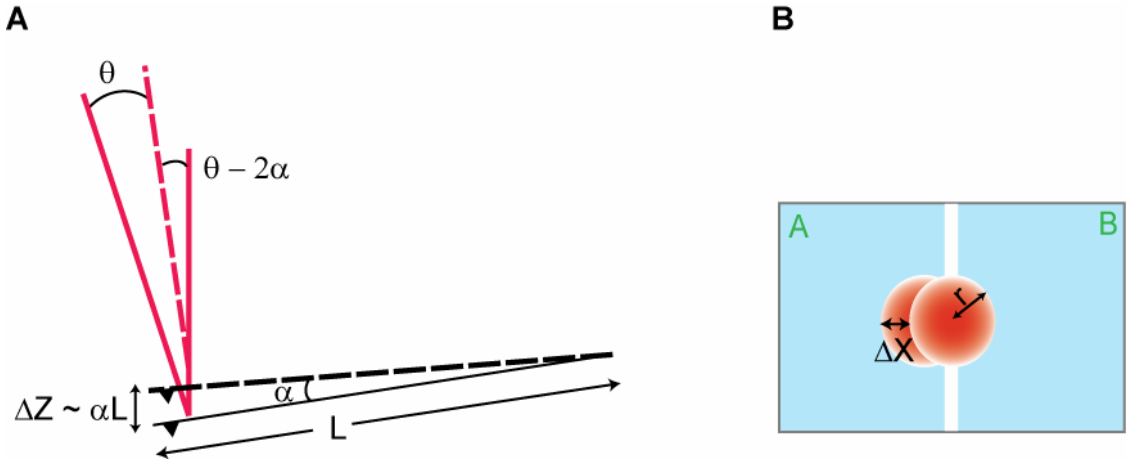

Figure 2.2 Cantilever deflection and beam translation on a SPD.

(A) Deflection of the cantilever through an angle α, results in deflection of the cantilever tip by ΔZ and an angular shift 2α in the reflected beam. Solid lines show the undeflected state and dashed lines show the cantilever and laser after deflection through α. **(B)** The angular shift translates the beam by ΔX on the SPD and changes the amount of light impinging upon each half of the detector (A and B). The two elements of the detector are physically separated by a "dead spot" (white bar), and the relative position of the beam is calculated as the difference in photocurrents generated on each detector element. While ΔX can be made arbitrarily large by simply moving the detector further from the cantilever surface, this does not improve signal-to-noise ratio (SNR) because the beam radius (r) also increases linearly with distance.

While this method is extremely sensitive, the use of adjacent, independent photocells with a "dead spot" between them imposes limitations on beam characteristics: 1) the beam diameter must be larger than the dead spot, 2) once the beam completely passes onto one element, position information is no longer available, and 3) the best SNR is obtained when maximum power is transferred between the two elements i.e. when the

beam is smallest on the detector. Thus there exists a tradeoff between SNR and large dynamic range *(113, 115)*. One should note that quadrant SPDs are also available in addition to the bi-cell style shown in Figure 2.2B. Quadrant SPDs are useful for detecting torsional motion of the cantilever *(116)*.

Lateral effect photodiodes

Another type of PSD used for positioning applications is the lateral effect photodiode (LEPD). These detectors yield position information based on the position of the "centroid" (intensity maximum) of the laser spot independent of spot size and beam profile *(117)*. The basic idea is illustrated in Figure 2.3.

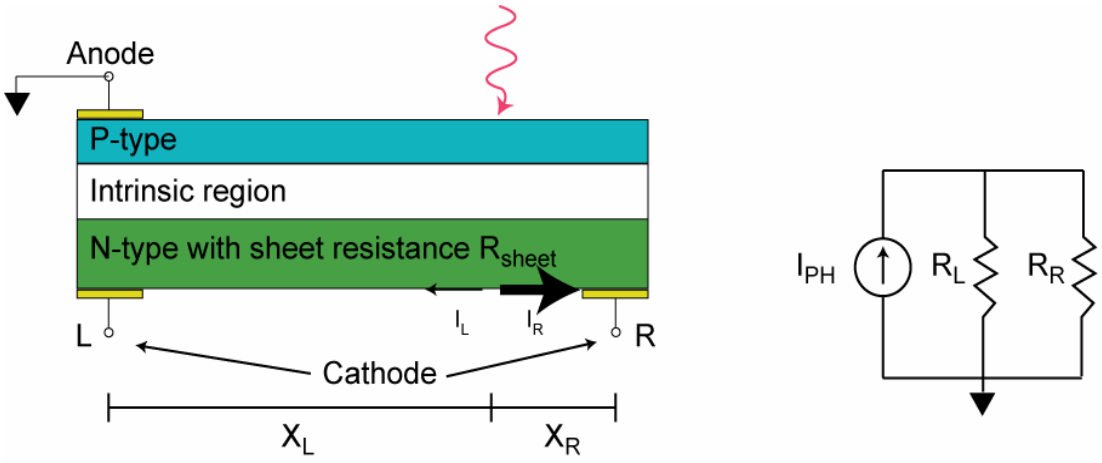

Figure 2.3 LEPD operating principle.

Light impinging upon the photodiode surface is absorbed in the intrinsic region and generates photocurrents. Current flows to the L or R cathode contact (in photoconductive mode) through the N-type material with resistance R_{sheet}. The amount of current flowing to towards each cathode depends approximately linearly on the distances, X_L and X_R, from each electrode (because the paths to the two cathodes essentially present two parallel resistors with $R \propto X$ (right)). Thus beam position is derived by subtracting the photocurrents flowing through each cathode contact.

Incident light generates photocurrent in the LEPD, and the current at each cathode is inversely proportional to the distance between the contact and the centroid of the beam. Position information is obtained by subtracting the photocurrents (actually voltages) generated at the two cathode contacts. LEPDs exhibit better than 1% deviation from absolute linear performance over the active area, and one can obtain continuous position information over nearly the entire device independent of beam profile because photocurrent is only generated at the centroid, unlike in SPDs. However, these devices suffer from lower sensitivity than SPDs because of the inherent Johnson noise added by R_{sheet} in the N-type layer. As this Johnson noise is usually the dominant noise in the device, LEPDs are inherently signal to noise (S/N) limited such that $\Delta q \approx \frac{L}{2(S/N)}$, where Δq is the minimum movement of the laser centroid and L is the length of the LEPD, meaning that a stable, high (but not saturating) laser power is recommended to maximize detector performance. The practical limit of position detection is $\Delta q \sim 0.5$ μm of centroid movement with LEPDs *(115)*.

Despite diminished sensitivity, these detectors offer a distinct advantage over SPDs because they provide continuous position detection over the entire active area *and* localized generation of photocurrents from the centroid of the laser spot. These characteristics present a unique property whereby the dynamic range can be optically tuned. Using optical telescopes, one can magnify or minify the amount of beam displacement on the detector element and thus change the dynamic range and sensitivity independent of the beam displacement resulting from cantilever deflection. This property is illustrated in Figure 2.4. The drawing shows that the beam centroid translates by

$h' = h * (f_2 / f_1)$ at the LEPD where h is the displacement of the beam due to cantilever deflection and f_1 and f_2 are the focal lengths of L1 and L2, respectively.

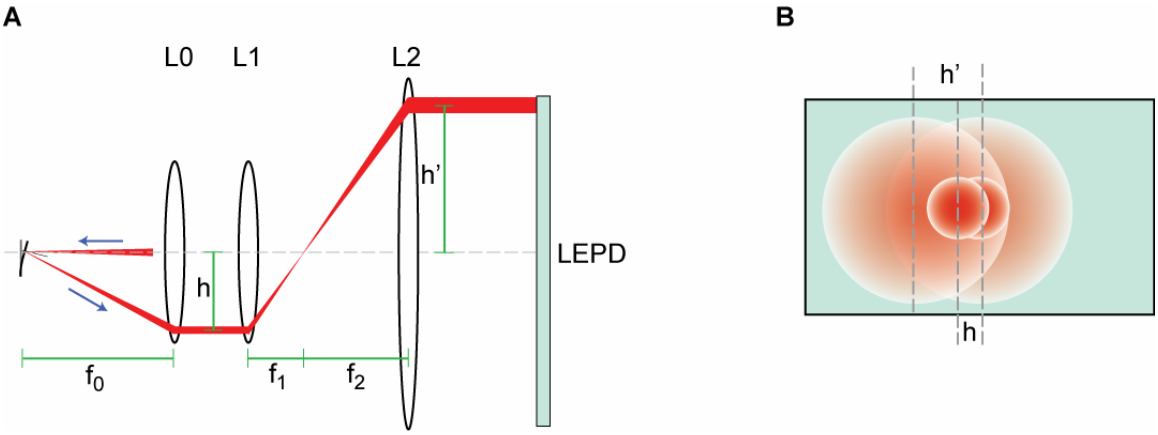

Figure 2.4 Using a telescope can modulate beam displacement on LEPDs.

(A) The focused laser (through L0) is reflected from a deflected cantilever surface (black curved line) and is displaced a distance h relative to the reflected beam from the straight cantilever (gray solid line). Using a Keplerian telescope (L1 and L2), the laser displacement is modulated by a factor (f_2/f_1) to h' on the LEPD, where f_1 and f_2 are the focal lengths of L1 and L2, respectively. **(B)** The centroid of the beam is translated a distance h' on the LEPD, and due to the centroid tracking feature in these devices, the position signal is amplified by a factor (f_2/f_1). In this way, the active area of the LEPD can be masked to measure laser displacement with a higher sensitivity ($f_2 > f_1$) or larger range (($f_2 < f_1$).

In this way, one can create an arbitrary dynamic range. This particular property is very useful for the actin experiments presented in Chapters 3-5 because network growth results in cantilever deflection that is greater than measurable with a SPD. A magnifying telescope before the LEPD allows use of the entire 10 mm x 10 mm active area in order to optimize both the dynamic range and sensitivity. However, it is important to note that as h' increases, the intensity of the laser spot decreases quadratically with h'/h, which

reduces the S/N of the detection system because of the reduced power at the centroid. Thus, one may need to increase the optical power when using a magnifying telescope to maintain appropriate S/N. Table 2.1 summarizes the benefits and drawbacks of each detector type and provides a short list of vendors.

	SPD	LEPD
Beam displacement resolution	100 nm	500 nm
Advantages	▪ better resolution ▪ lower detector noise ▪ smaller dependence on laser intensity ▪ uniform photo elements ▪ excellent short range performance	▪ continuous position detection over active area ▪ centroid tracking ▪ position information independent of intensity profile ▪ superb linearity ▪ variable dynamic range with telescopes
Disadvantages	▪ intensity profile affects linearity ▪ beam must be larger than dead spot ▪ limited dynamic range	▪ position resolution depends on detector size and intensity ▪ added Johnson noise due to sheet resistance ▪ reduced resolution
Vendors	UDT Sensors, Pacific Silicon Sensors, Thorlabs, New Focus, Newport	

Table 2.1 SPD and LEPD characteristics.

Transimpedance amplification and signal acquisition

In order to measure position with either type of PSD, a current-to-voltage amplifier, or transimpedance amplifier (TIA) is often used. Following the TIA conversion of photocurrents to voltages, one has the choice to either 1) digitize the signals with a data acquisition board (DAQ) or 2) perform further analog computation

before digitization. Each method offers benefits and drawbacks, and often either is acceptable. The issues that ultimately determine the appropriate method are: 1) the bit-depth and quantization error of the DAQ versus the deflection sensitivity of the optical lever and PSD (ΔV/nm of cantilever deflection), 2) the speed requirement for the AFM, and 3) circuit construction experience of the builder. Analog signal processing should be done carefully for sensitive and accurate detection otherwise unnecessary noise will corrupt the deflection signal. Independent of the method chosen, before any signals are sampled with a DAQ, they *must* pass through an analog anti-aliasing filter to remove any high frequency content above the Nyquist frequency (equal to 0.5 times DAQ sampling frequency). This information can not be legitimately sampled and will convolute the data in an irreversible way.

When recording monitoring cantilever position over longer times (minutes to hours), the difference voltage, $V_L - V_R$ (LEPD) or $V_A - V_B$ (SPD), should always be normalized by the total amount of light incident on the detector. Thus for the X position of the beam: $X_{pos} = \frac{V_A - V_B}{V_A + V_B}$ for **SPDs** and $X_{pos} = \frac{V_L - V_R}{V_L + V_R}$ for **LEPDs**. This normalization accounts for any temporal power fluctuations and slow drift in the laser power, which become a significant problem for long time-scale measurements. A beam power fluctuation during an experiment will change the raw difference voltage by a factor α, which would correspond to a different cantilever deflection based on difference voltage alone, even though the cantilever deflection has not changed. The normalization shown above negates this issue because both the sum and difference voltages will be changed by α so the normalized difference will not change. Normalization can be performed in the analog or digital domain depending on preference. More information on

TIA circuits and other electrical tutorials are available in the *Art of Electronics* by Horowitz and Hill *(118)*.

Current product lines from Pacific Silicon Sensor offer on-board TIAs and normalization circuitry for two-dimensional position detection (X and Y) in both SPDs and LEPDs. These products are offered in a compact package and require only soldering a connector in order to access the voltages. Optical component distributors such as Thorlabs, Newport, and New Focus offer plug-and-play PSDs where the voltage outputs can be directly digitized from the unit, but the package is significantly larger. More information regarding PSDs can be found on the UDT website *(115)*.

2.2.3 Nanopositioning systems

Quite possibly the most important part of all scanning probe microscopes is the nanopositioner because these devices move the sample relative to the cantilever and all calibrations are based on their performance. By far the most common nanopositioners are piezoelectric actuators (piezos). Piezos essentially change their length in proportion to an applied voltage (Figure 2.5) and the minimum incremental movement is ultimately determined by the noise in the driving electronics – not by the piezo itself.

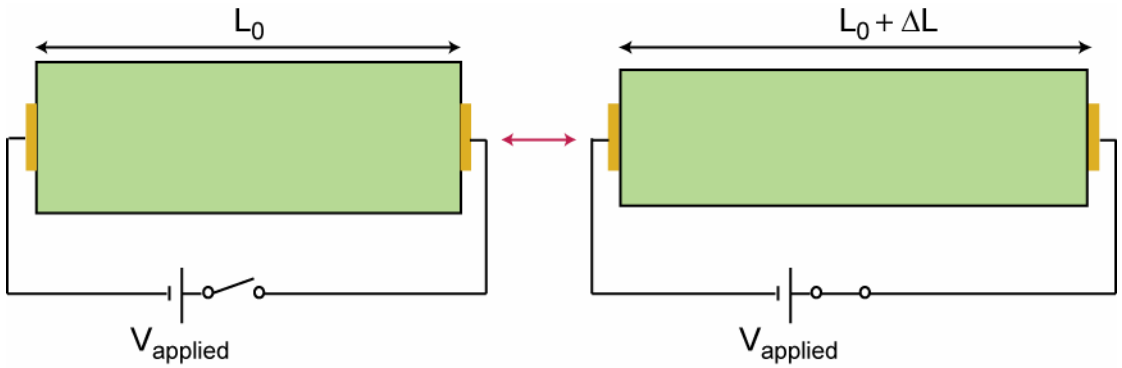

Figure 2.5 Basic piezo expansion principle.

Piezos used in AFM applications expand with applied voltage where $\Delta L \propto V_{applied}$. In principle ΔL can be arbitrarily small because there is no friction or stiction during movement, and the minimum incremental movement is only limited by the SNR of $V_{applied}$.

The ability to execute well-controlled, repeatable nanometer-scale motion is imperative for measurement of molecular forces important in biology. Single actin filaments measure 6 nm in diameter and produce pN propulsive forces so it is absolutely necessary that to have high resolution movement of the sample relative to the cantilever.

Closed-loop piezos are the ideal choice for AFM applications. Raw piezo stacks are not well suited for high-resolution and stable use because of the following limitations: non-linear expansion, hysteresis, backlash, creep, and poor bidirectional repeatability. Significant technological advancement in position sensor technology and guiding flexures has resulted in closed-loop piezos that exhibit very precise movements and unprecedented bidirectional repeatability over large travel ranges. Piezos operating in closed-loop mode with high resolution capacitive, strain gauge, and linear voltage differential transformer sensors and guided with precision designed flexures to linearize motion offer sub-angstrom incremental movement and bi-directional repeatability of less

than 1 nm over 100 μm of linear travel. In addition creep, hysteresis, and backlash are all virtually eliminated under closed-loop control. In general, all modern AFM biophysical applications demand closed-loop performance, but it should be noted that this inherently reduces position resolution because of electrical noise in the feedback circuit while also increasing the response time of positioning system *(119)*.

The appropriate piezo for an AFM is highly dependent on the intended application (imaging, force spectroscopy, etc). For example, if fast (1 kHz), high resolution (1 nm), and repeatable sample scanning is desired over a limited range (less than 10 x 10 x 10 μm in X, Y, and Z), then one should use a direct-drive piezo with a sufficiently high resonance frequency and accuracy. In a direct-drive system, piezo expansion directly moves the payload (1:1 ratio of piezo to load movement). In general, direct-drive systems are more accurate, exhibit significantly faster settling time (and a higher resonance frequency), exert considerably more force, support greater torque, and are much stiffer. However, these systems also cost more and often occupy more physical space because they must house large piezo stacks. For example, a 20 mm piezo stack has a nominal expansion of ~ 20 μm so one would need a ~ 100 mm piezo stack to create ~ 100 μm of direct-drive motion. This can be a significant limitation in certain situations where space is at a premium.

On the other hand, if an application calls for significant range (100μm of Z motion) and high resolution (1 nm precision and accuracy), but high speed is not a requirement, then one may opt for a lever-arm amplified system to save space and money. Lever-arm amplified systems move the payload by lever action over some distance from actual piezo movement. An important note that is often overlooked for

lever-arm amplified systems is the location of the position sensor. In these systems, the sensor is often on the piezo stack NOT the moving payload, which can result in systematic errors with larger loads. In direct drive systems, this is not an issue since piezo motion directly couples to payload motion. A nice (and slightly biased) overview of the piezo technology and physics is provided on the Physik Instrumente website *(120)*.

2.2.4 Macroscopic alignment

When building an instrument from scratch, one should have at least two one-dimensional translation stages (Thorlabs MT1 – 0.5" motion), one for moving the cantilevers into the focus of the incoming laser and another for positioning the PSD relative to the reflected laser. In addition, standard beam steering kinematic mirror mounts (Thorlabs KS1 – 1" optic kinematic mounts) and mirrors (Thorlabs PF10-03-G01 – 1" inch mirrors) will be useful steer the laser onto the cantilever surface. Finally, a basic imaging system: a simple finite tube length objective, a basic light source, and CCD sensor (Edmund Optics) (if one is not using a microscope base) is invaluable for locating the focus of the laser and positioning the beam onto a cantilever. Once the beam looks positioned in the imaging system, the alignment should be checked by inspecting the reflected beam quality. If the appropriate laser and focusing optic have been chosen such that the focused spot is well contained on the cantilever surface, then the reflected and incident beams should look qualitatively similar at one focal length away from the cantilever surface because the undeflected cantilever is essentially a mirror. Any beam clipping or speckle pattern is not acceptable. Lastly, it is important to align the laser near the free end of the cantilever. An empirical method for determining the appropriate beam

position is to observe the reflected beam vanish and appear as the incident beam is moved in X and Y on-and-off the cantilever surface. The reflection of a well focused and aligned beam will vanish and appear very cleanly and quickly as the incident beam is scanned over the cantilever surface.

2.3 Optical imaging

Combining AFM with wide-field epifluorescence imaging is straightforward and leverages fluorescent labeling techniques attractive in cell biology applications and biomolecule imaging. More advanced imaging techniques such as total internal reflection fluorescence microscopy *(99)* and two-photon microscopy *(121)* were recently shown to work well with AFM. However, it wasn't until the release of the BioScope II AFM from Veeco that commercial AFMs allowed use of any specific brightfield imaging techniques such as differential interference contrast, Hoffman contrast, and phase contrast. These developments increase both the utility of AFM for cell biology applications and reduce the time/effort for laser spot alignment onto the end of the cantilever thereby making AFMs more attractable for non-experts users.

2.4 Noise and calibration

2.4.1 Noise

Four primary sources of noise must be minimized when constructing a high-resolution AFM: acoustic, electrical, mechanical, and optical noise. The easiest method for diagnosing noise-related issues is acquiring power spectra of the thermal fluctuations

of the cantilever. Each type of noise has specific frequency signatures that make noise diagnosis and reduction much easier in the spectral domain.

Acoustic enclosures offered by Technical Manufacturing Corporation provide well-manufactured solutions specifically designed to house sensitive instrumentation. These units provide a stainless steel platter inside of an acoustically insulated enclosure with an optional pneumatic isolation system. In the frequency domain, acoustic noise can excite resonances in the AFM and these peaks are generally located between 20 Hz and 20 kHz. The peaks are reasonably broad and do not exhibit the sharp signature associated with electrical noise. If an acoustic enclosure is not available, then an acrylic box lined with sound insulating foam can be used to minimize acoustic coupling from ambient noise.

Electrical isolation can be achieved by assuring that no ground loops are present in the entire instrumentation system; there should only be one analog and one digital ground. Providing power to the entire system through a universal power supply (UPS) unit reduces the power fluctuations and protects expensive equipment from potential harm in the event of a power outage. If a UPS is not available, surge protectors (TrippLite or other brands) with filter banks should be used to reduce 60 Hz electrical noise. Besides the 60 Hz noise, electrical noise sources generally appear as sharp peaks at frequencies beyond of a few kHz in the power spectrum. Because most other sources of noise do not manifest as extremely narrow bandwidth spikes, these sources are diagnosed in a fairly straightforward manner compared to the other sources.

Optical noise, i.e. ambient light should be reduced as much as possible to avoid the significant 120 Hz noise associated with most room incandescent and fluorescent

lamps. This is usually accomplished in one of the following ways: 1) turning off the lights, 2) enclosing the PSD with a black box only allowing a hole for the laser light to enter, or 3) using an interference filter that allows only the laser wavelength to impinge on the detector.

Mechanical noise is by far the most common culprit of noise sources in AFM instruments. Insecure mounting of any component: the laser, piezo, detector, lens, mirrors, etc. can give rise to peaks in the power spectrum similar in appearance to acoustic peaks. The AFM should be constructed on a pneumatically-isolated optical table if possible to mechanically uncouple the AFM from building and ground vibrations. The basic idea for mechanical isolation in an AFM is to use the "floated" table as a low-pass filter and stiff construction materials for the AFM as a high-pass filter such that the net result is a band-reject filter over the frequency band of interest. In addition to pneumatic isolation, stresses due to very stiff, taught cables should be avoided and cables should be stress relived as close to the AFM as possible. This minimizes external coupling (by accidentally touching remote portions of the cables). Mechanical noise peaks generally have noticeable bandwidth compared to electrical peaks and are seen over a similar range as acoustic peaks. The noise levels in the AFM environment should be optimized and removed commensurate with the level of performance desired. A review by Neuman and Block discusses similar noise issues for optical traps and serves as a good reference *(122)*.

2.4.2 Stiffness calibration

Stiffness calibration of AFM cantilevers is a well studied topic and a recent article by Lévy and Maaloum provides a nice summary *(123)* of the different computational and experimental methods. It is essential to calibrate cantilevers before use because without a reliable stiffness, it is impossible to know the amount of force applied to a sample. The thermal spectrum method pioneered by Hutter and Bechhoefer *(124)* is common non-destructive method for obtaining cantilever spring constants. This calibration method fits the power spectrum of the thermal fluctuations of the cantilever with a model of a damped, thermally-driven harmonic oscillator. This model can be derived by writing the equation of motion (1) of a thermally driven mass m with drag coefficient γ attached to the end of a cantilever spring with stiffness k_{cant}

$$F_R(t) = m\frac{d^2z(t)}{dt^2} + \gamma\frac{dz(t)}{dt} + k_{cant}z(t) \qquad (1)$$

where $F_R(t)$ is the thermal driving force and $z(t)$ is position of the mass at the end of the cantilever. After taking the Fourier transform of (1), multiplying by the conjugate quantities, and some algebraic manipulation, one obtains the power spectrum for the fluctuations as

$$\left|\tilde{Z}(\omega)\right|^2 = \frac{4k_BT\gamma}{(k_{cant} - m\omega^2)^2 + \omega^2\gamma^2} \qquad (2)$$

where ω is the angular frequency in radians/s. In practice, one obtains the power spectrum and fits (2) to the first resonance of peak to obtain an estimate of k_{cant} because higher modes are assumed to contribute very little to thermal fluctuations *(124)*.

A second calibration method for AFM cantilevers that also uses power spectral data takes advantage of the equipartition theorem that states that each harmonic potential

in the Hamiltonian contributes *(1/2)k_BT* of energy on average, where k_B is Boltzmann's constant and T is temperature in Kelvin. The Hamiltonian for a thermally vibrating cantilever can be written as *(124)*

$$E = \frac{p^2}{2m} + \frac{1}{2}k_{cant}z^2 \qquad (3)$$

where the first term on the right describes the kinetic energy and the second term describes the potential energy for a cantilever with mass m, momentum p, stiffness k_{cant}, and tip position z. Thus, the equipartition theorem states that the potential energy in (3)

$$U = \frac{1}{2}k_{cant} < z^2 >= \frac{1}{2}k_BT \qquad (4)$$

In order to obtain the $<z^2>$ of the cantilever tip, the first cantilever resonance mode in power spectrum is fit with a Lorentzian, and the resulting fit is integrated over frequency to obtain $<z^2>$ and subsequently calculate k_{cant}. The accuracy of these two models is within 20-30% of actual value *(123)* (see Figure 3.2), possibly due to the complicated shape of a thermally vibrating cantilever *(125)*. It is *extremely* important that the sampling rate of the DAQ system is sufficiently high to capture at least the first resonance of the cantilever vibration when acquiring thermal data. Otherwise it is impossible to fit the power spectrum with a Lorentzian and obtain an estimate for k_{cant} with these methods.

2.5 Conclusion

I have participated in construction of three custom AFMs with each system offering unique functionality. The differential AFM (discussed in Chapter 3), which monitors position of two cantilevers simultaneously (Figure 2.1B), was the first

instrument that I built. The motivation for this instrument was to use one cantilever as a sensor for the glass surface to improve the positional stability of the cantilever-surface distance over long times. Because actin network growth occurs over hours and thermal drift is on the same order as network growth, this improvement was necessary to make long these time-scale measurements possible. This instrument is well-suited for measurements of dynamic processes that can be localized to a cantilever where no scanning or sample positioning is required.

The next AFM that I worked on was a sideview imaging AFM, which incorporated a side-profile imaging path that allows imaging of the sample along the direction of applied force without the complexity of an optical sectioning system and computational reconstruction *(3)*. This AFM combines pN level sensitivity with high resolution optical imaging to visualize deformations along the loading direction. Because of this unique combination, this system is well-suited for cell mechanics and adhesion measurements where it is unclear how cell deformability and internal cellular features respond under different loading conditions.

Finally, I have recently begun construction of a system that permits independent, nanometer-scale spatial control of two cantilevers simultaneously. Information processing through a cell or among many cells is typically investigated with fluorescent microscopy. Recent developments in our lab have allowed measurements of mechanical coupling within a single cell, but these measurements do not have nanometer level accuracy *and* millisecond time resolution. This latest AFM will allow for arbitrary spatial positioning of each cantilever with respect to the sample and with respect to the other cantilever, providing the ability to monitor information transfer in a high bandwidth

over length scales from 10 nm to 100 μm in response to a variety of mechanical inputs. Each instrument has presented a different set of design challenges, but common metrics such as the power spectrum of cantilever fluctuations, cantilever-surface drift, piezo linearity, laser power stability, control system response time, and many others have proven very useful for optimizing performance.

CHAPTER 3: DIFFERENTIAL FORCE MICROSCOPE FOR LONG-TIMESCALE BIOPHYSICAL MEASUREMENTS

Reprinted with permission the American Institute of Physics from article "Differential force microscope for long-timescale biophysical measurements" by Jason L. Choy Sapun H. Parekh, Ovijit Chaudhuri, Allen P. Liu, Matthew J. Footer, Julie A. Theriot, Carlos Bustamante, and Daniel A. Fletcher in *Review of Scientific Instruments* **78**(4), April 2007.

3.1 Abstract

Force microscopy techniques including optical trapping, magnetic tweezers, and atomic force microscopy (AFM) have facilitated quantification of forces and distances on the molecular scale. However, sensitivity and stability limitations have prevented the application of these techniques to biophysical systems that generate large forces over long times, such as actin filament networks. Growth of actin networks drives cellular shape change and generates nano-Newtons of force over timescales of minutes to hours, and consequently network growth properties have been difficult to study. Here we present an AFM-based differential force microscope with integrated epi-fluorescence imaging in which two adjacent cantilevers on the same rigid support are used to provide increased measurement stability. We demonstrate 14 nm displacement control over measurement times of 3 hours and apply the instrument to quantify actin network growth *in vitro* under controlled loads. By measuring both network length and total network fluorescence simultaneously, we show that the average cross-sectional density of the growing network remains constant under static loads. The differential force microscope presented here provides a sensitive method for quantifying force and displacement with long-timescale stability that is useful for measurements of slow biophysical processes in whole cells or in reconstituted molecular systems *in vitro*.

3.2 Introduction

Cells possess an array of highly specialized protein machines that orchestrate and perform essential cellular functions such as division and motility. In recent years, force microscopy techniques including optical trapping, magnetic tweezers, and atomic force microscopy (AFM) have provided insight into the importance of physical forces and mechanical properties in the functioning of biological systems at the molecular level *(126)*.

A common limitation of these techniques is thermal drift of the probe (a bead in case of optical and magnetic tweezers and a cantilever in the case of AFMs), as well as drift of the surrounding microscope components. If the drift rate is similar to the mechanochemical timescale for the biological system of interest, then it is impossible to obtain high fidelity force and position data. This limitation has recently been addressed for high-resolution tracking of molecular motors, such as RNA polymerase, through the use of a levitated optical trapping geometry *(127)*. Other attempts to reduce the influence of thermal effects include differential back focal plane detection for optical traps and differential cantilever or interferometric detection in single-molecule and imaging AFM applications *(128-132)*. However, these techniques have been demonstrated to probe systems that produce small forces (~ nN) over short times (~ seconds).

Here we present the design and verification of an AFM-based differential force microscope that can achieve 14 nm absolute stability between the cantilever and surface for at least 3 hours. The instrument, which has recently been used in studies of actin network force generation and mechanics *(37, 74)*, is integrated with an epi-fluorescence microscope and used here to obtain new measurements showing that average network

density (as measured by total fluorescence divided by network length) is constant under a controlled load.

3.3 Atomic force microscopy for biophysical measurements

Coordinated multi-molecule biological processes, such as actin polymerization, generate and respond to large forces over long times, and single-molecule force microscopy techniques are generally not appropriate for studying these processes. Actin filament networks, which generate protrusions during cell crawling and shape changes during phagocytosis, can generate nano-Newtons of force over timescales of minutes to hours through the addition of nanometer-scale actin monomers *(65, 74)*. Study of their force generation capabilities has been hindered by the lack of suitable techniques for probing them while at the same time imaging spatial and temporal changes in the organization of fluorescently labeled proteins.

AFMs are attractive tools for investigating biophysical processes in cells like actin network growth since they are capable of measuring nanometer-scale displacements and a wide range of forces. Typical AFMs can measure forces well into the nano-Newton range, the scale of forces believed to be generated by cellular processes such as pseudopod formation *(133)*. Furthermore, AFMs are easily integrated with fluorescence microscopes. In an ideal AFM force-distance measurement, the position of the surface is fixed, and changes in deflection of the cantilever's tip are equal to changes in the end-to-

end distance of the sample under study and are related to the force exerted on the sample by Hooke's law.

In practice however, drift caused by temperature fluctuations in the surrounding environment can cause spontaneous cantilever bending and unpredictable drift between the cantilever and surface. Cantilevers bend as temperature fluctuates, even in the absence of an externally applied force, which can result in a shift of the zero-force position of the cantilever *(134)*. Treatments such as thermal annealing, use of cantilevers without reflective or other asymmetric coatings, or torsional cantilevers can be used to reduce this effect *(134-136)*.

Over long times, temperature fluctuations and gradients can cause drift of the entire microscope apparatus, resulting in unwanted changes in the distance between the cantilever and surface that are much larger than cantilever bending and preclude accurate measurements of sample length *(129)*. Conventional AFM measurements with single cantilevers cannot distinguish between this cantilever-surface drift and actual sample length changes since both may result in cantilever deflection. Drift in commercial systems can exceed 20 nm/min, which is on the same order as actin network growth rates and can therefore mask changes in network length (data not shown). Cantilever-surface drift is a recognized limitation of AFM and has been addressed in a variety of ways for imaging, electrochemical, and single-molecule force spectroscopy applications *(129, 131, 137, 138)*. Our differential force microscopy technique with integrated epi-fluorescence addresses cantilever-surface drift for molecular systems that generate large forces over long times.

3.4 Instrument design and performance

3.4.1 Design principles

The instrument consists of an epi-fluorescence-equipped AFM modified to measure the deflection of two cantilevers simultaneously. In our system, two cantilevers – a "reference" and a "measurement" cantilever – attached to the same rigid support are mounted above a surface at a 10° angle (Figure 3.1, inset) similar to the experimental geometry described previously in Altmann *et al (129)*. When undeflected (Figure 3.1, inset gray dotted lines), the reference cantilever is closer to the surface than the undeflected measurement cantilever by a distance D_o and is the first to make contact when the surface is raised.

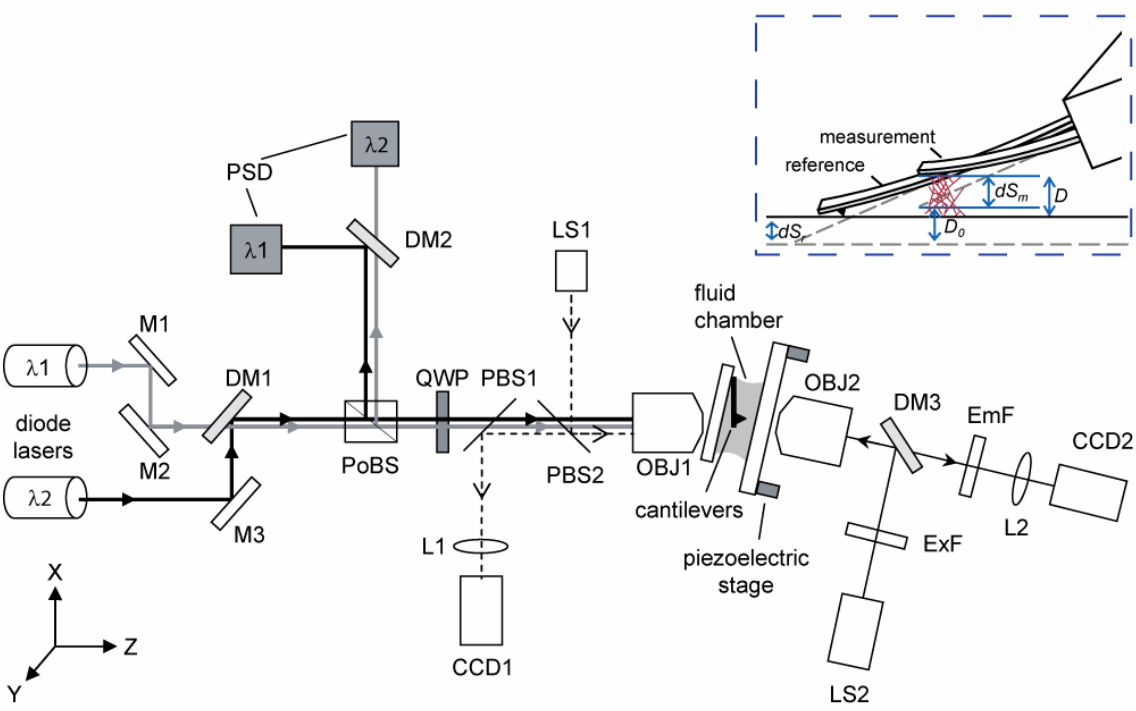

Figure 3.1 Optical schematic of the differential force microscope.

Two similarly polarized diode lasers (λ1,λ2) are steered by mirrors (M1, M2,M3), combined by a dichroic mirror (DM1), and focused through a microscope objective (OBJ1) onto the two cantilevers. The reflected

beams are collected by the same objective, reflected by a polarization beam splitter (PoBS), and separated by a dichroic mirror (DM2) onto two position sensitive detectors (PSD). The cantilevers and sample can be illuminated with a broad band LED source (LS1) via a pellicle beams splitter (PBS2) and OBJ1, enabling both reflection (OBJ1, PBS1, L1, CCD1) and transmission (OBJ2, L2, CCD2) imaging. Epi-fluorescence imaging of the sample (OBJ2, L2, CCD2) is obtained by fluorescence illumination with a mercury arc lamp (LS2) via OBJ2 through an excitation-emission cube (ExF, DM3, EmF). A feedback-controlled piezoelectric stage is used to control surface position. (Inset), Diagram showing the two-cantilever geometry of the differential AFM technique and drift correction principle. Actin network (red lines) length (*D)* can be accurately quantified over long times without the influence of cantilever-sample drift by monitoring deflection of a measurement (dS_m) and reference cantilever (dS_r) simultaneously. Because the reference cantilever is in contact with the surface at all times, any common-mode cantilever-surface movement will be directly quantified as a change in dS_r making it possible to eliminate this error from measurements of actin network growth. Dotted lines (gray) depict the original position of the surface position and undeflected cantilevers.

If dS_r is the deflection of the reference cantilever when in contact with the surface and dS_m is the deflection of the measurement cantilever when in contact with the sample, the distance D between the tip of the measurement cantilever and the surface is

$$D(t) = D_o - dS_r(t) + dS_m(t) \qquad (1)$$

Any drift in the position of the surface with respect to the measurement cantilever is detected by a change in dS_r. Feedback on dS_r or dS_m can be used to create three different modes of operation:

(1) Drift clamp: Surface position is adjusted to keep dS_r constant, thus minimizing common-mode cantilever-surface drift from measurements of sample length and force over time.

(2) Force clamp: Surface position is adjusted to keep dS_m constant, thus maintaining a constant force applied by the measurement cantilever over time, regardless of cantilever-surface drift. With dS_m fixed, changes in length are directly measured by changes in deflection of the reference cantilever (ΔdS_r).

(3) Position clamp: Surface position is adjusted to keep (dS_m - dS_r) constant, thus maintaining a constant separation between the measurement cantilever and the surface over time, compensating for all cantilever-surface movement.

3.4.2 Optical lever detection

Deflections of the two cantilevers are monitored simultaneously with an objective-based optical lever system similar to that used by Wikramasinghe *et al.* and Schaffer *et al*. to monitor one cantilever *(139, 140)* (Figure 3.1, see Methods for a list of components). In our system, the cantilevers are positioned in the focal plane of a single infinity-corrected objective lens, and two independent lasers with different wavelengths are focused through the objective onto the two cantilevers. The beams reflected by the cantilevers are collected by the same objective and separated by a polarization-dependent beam splitter and dichroic mirrors onto two independent position sensitive photodetectors. Application of an external force to either cantilever causes that cantilever to bend, changing the angle of its reflecting surface. This change in angle is converted by the objective lens into a lateral shift in the position of the reflected beam on the position sensitive photodetector (Figure 3.2A,B). For a given change in cantilever angle α, the angle of the reflected beam with respect to the optical axis changes by 2α. The

corresponding shift in the position Δh of the beam on the detector can then be expressed as

$$\Delta h = f\left[\tan(\theta) - \tan(\theta + 2\alpha)\right] \qquad (2)$$

where f is the focal length of the objective lens and θ is the angle of incidence of the laser on the cantilever relative to the optical axis. The bending angle of the cantilever can further be related to the displacement of the cantilever's tip, y, using the relation

$$\alpha = \tan^{-1}(3y / 2l) \qquad (3)$$

where l is the length of the cantilever*(97)*. The sensitivity of this detection scheme is similar to that of traditional optical lever designs as demonstrated by the instrument's ability to resolve thermally-limited deflections of the cantilever during cantilever calibration (Figure 3.2C) *(95, 124, 141)*.

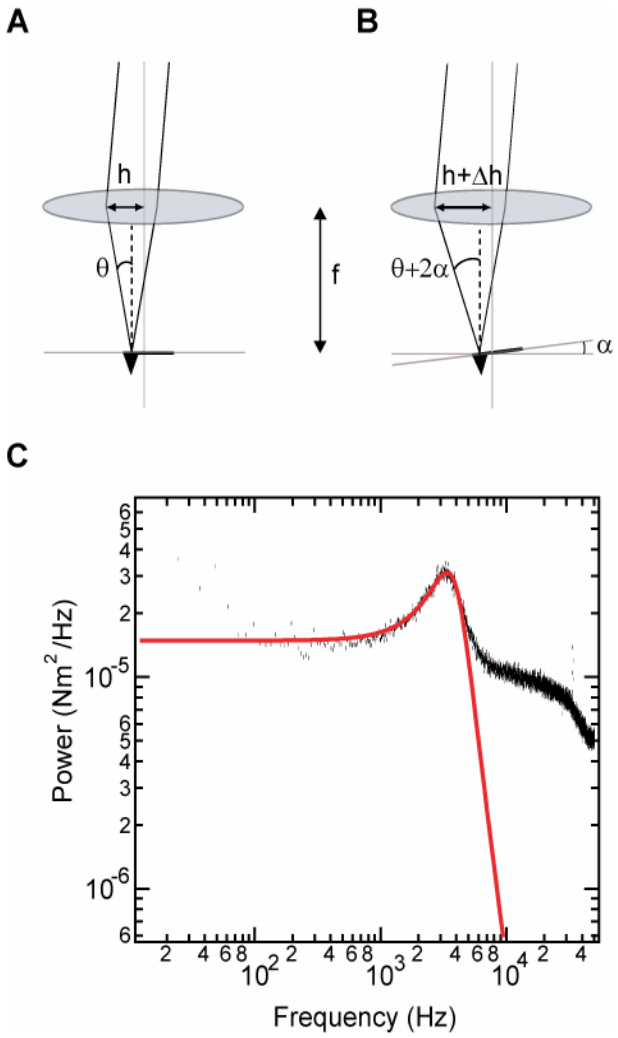

Figure 3.2 Ray optics diagram of the objective-based optical lever and power spectrum of cantilever noise, both shown for a single cantilever.

(A) Light incident on the undeflected cantilever reflects at an angle θ and is displaced from the optical axis upon reflection by a distance $h = f\ tan(\theta)$ at the principal plane of the objective (shown here as a single lens). **(B)** Upon bending, the cantilever reflecting surface changes by an angle α, shifting the angle of the reflected beam by an amount 2α and changing the lateral displacement of the beam at the principal plane of the objective to $h = f\ tan(\theta+2\alpha)$. Thus, the cantilever bending angle α is detected as a lateral displacement $\Delta h = f\ [tan(\theta) - tan(\theta + 2\alpha)]$. **(C)** Power spectrum of a freely suspended cantilever in *Xenopus* buffer (see Methods). The first resonance of the raw power spectrum (black dots) is fit by a Lorentzian function (red line), which is characteristic of a damped, driven harmonic oscillator, demonstrating that our differential AFM setup is thermally limited. Data was acquired at 100 kHz and anti-aliased to 50 kHz. Spring

constants were extrapolated from the fitted power spectrums using the equipartition theorem and ranged from 29-33 pN/nm, which is within 20% of the manufacturer's value of 30 pN/nm *(124)*.

The use of an objective lens to both focus the incident beams and collect the reflected beams provides several advantages over a free-space design for monitoring two cantilevers and interferometer-optical lever combination *(129, 130, 132)*. First, the lasers share a beam path over much of their trajectories, simplifying the optical path and enabling additional lasers to be added with minimal perturbation *(110)*. Second, our system is compatible with smaller cantilevers that offer improved force resolution *(110, 142)*. An objective lens with a higher numerical aperture could be used to focus the lasers more tightly onto the reduced dimensions of the small cantilevers. Finally, use of an objective lens enables reflection and transmission imaging (Figure 3.1) of the cantilevers and sample for easy alignment. We note that this instrument is designed to measure sample displacement and force and is not intended for topographical imaging applications in its current form.

3.4.3 Spatial stability characterization

As a demonstration of the utility of our differential force microscope, we present its ability to control cantilever-surface separation over long times. This was done by monitoring how the distance between the measurement cantilever and the surface changed with time immediately after the cantilevers were immersed in a standard biological buffer. We compared the cantilever-surface drift when the instrument was operated as a position clamp to when no differential feedback was used (Figure 3.3). During the test, the measurement cantilever was freely suspended above the surface, and

the reference cantilever was held in contact to monitor the surface the position. At regular intervals, cantilever-surface separation was measured by bringing the surface into contact with the measurement cantilever.

When the position clamp (feedback) was active (Figure 3.3A, inset), the root-mean-square (RMS) deviation in the cantilever-surface separation with respect to the initial value was fewer than 14 nm over 3 hours (n=8, Figure 3.3A) and showed no clear time dependence. This is in sharp contrast to the results obtained when the clamp was not used where position error accumulated with time and was often more than 2000 nm at the end of a measurement (n=8, Figure 3.3B). This two order of magnitude reduction in drift demonstrates the ability of our AFM-based differential force microscope to dramatically minimize unwanted cantilever-surface drift for long-timescale experiments. While these results illustrate the advantage of this differential AFM technique, we note that even better performance may be obtained by using two cantilevers with the same physical dimensions and adjusting the angle of the sample surface to impose an asymmetry in the cantilever-surface distance between the cantilevers. In principle, this approach could reduce differential cantilever drift, which may be responsible for the residual 14 nm error in our spatial stability measurements with the position clamp active.

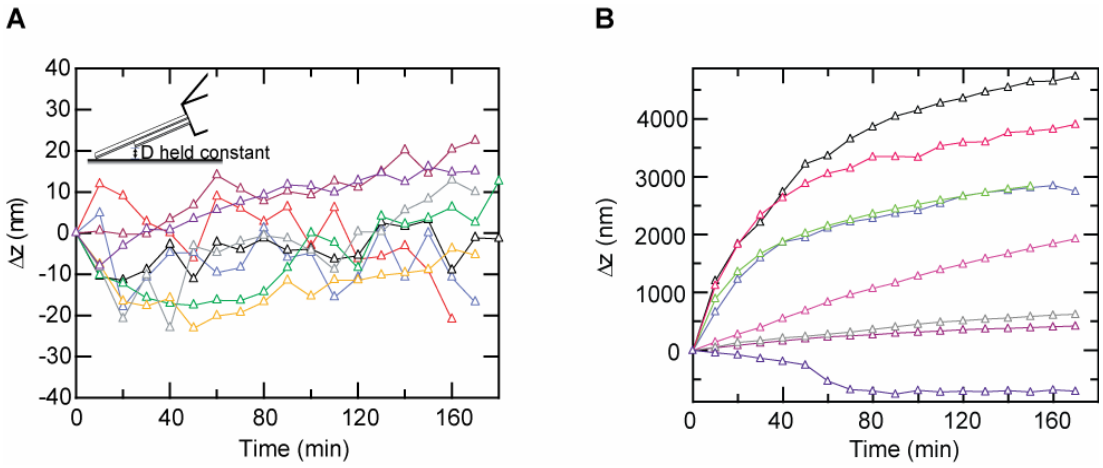

Figure 3.3 Cantilever-surface drift, Δz, with position clamp active.

In all experiments, data acquisition (100 Hz) was initiated 2-4 minutes after the cantilevers were immersed in Xenopus buffer, and the measurement cantilever was freely suspended while the reference cantilever was held in contact with the surface. To quantify drift, the cantilever-surface separation was sampled at 10 minute intervals by moving the surface into contact with the measurement cantilever. Individual data points (open triangles in both panels) are connected with line segments, and different colors indicate different experiments. **(A)** Graph showing Δz vs. time for position clamp experiments where differential feedback was used to keep cantilever-surface separation, D, constant (inset). The RMS Δz was always less than 14 nm over an individual 3 hour measurement period, and the absolute Δz never exceeded 22 nm (n = 8). **(B)** Experiments where the position clamp was inactive showed an absolute Δz often greater than 2000 nm after 3 hours (n = 8). Experiments where the position clamp was active demonstrate the operational advantage of this differential AFM technique to improve positional stability by better than 2 orders of magnitude.

3.5 Application to actin network growth

As an application of this instrument to probe force-generating biophysical systems, we used the differential force microscope in force-clamp mode to monitor actin network growth between the measurement cantilever and surface. We detected changes

in the actin network length with the reference cantilever and held a force of 36 nN on the network with the measurement cantilever (Figure 3.4, upper inset). Actin network growth was localized to the measurement cantilever by nonspecifically adsorbing the bacterial nucleation promoting factor, ActA, directly onto the measurement cantilever's surface (see Methods). No ActA was adsorbed onto the reference cantilever. Both cantilevers were then immersed in *Xenopus laevis* cytoplasmic extract, in which ActA activates the Arp2/3 complex to stimulate growth of a branched actin filament network *(68, 74)*.

A low concentration of rhodamine-actin was added to the extract and incorporated into the network, allowing network growth to be visualized through the integrated epi-fluorescence microscope. Cantilever deflection was recorded continuously while fluorescence images were taken at 10 minute intervals to quantify the amount of polymerized actin at the cantilever's surface (Figure 3.4, lower inset). The measured network length was found to directly correlate with increasing fluorescence intensity (Figure 3.4, solid line and crosses). The ratio of fluorescence intensity to length varied little over the experiment with a standard deviation less than 2.7% of the mean, demonstrating that the average cross-sectional network density did not change noticeably as the network elongated under a constant force.

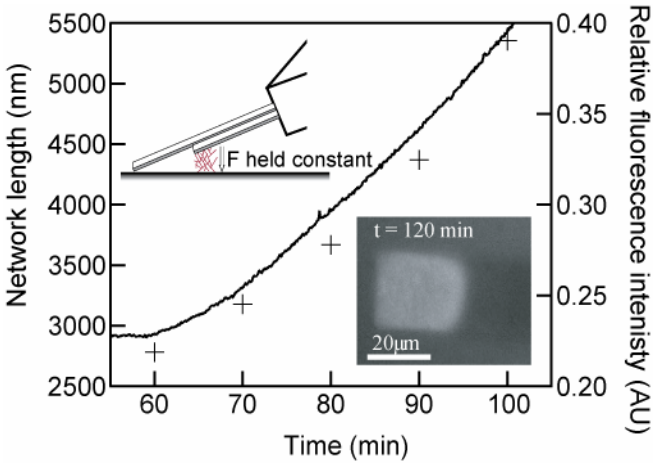

Figure 3.4 Simultaneous force and fluorescence microscopy of actin network growth in a force clamp.

Length vs. time (solid line) plot of actin network growth under a constant force F = 36 nN load applied by the measurement cantilever (upper inset). Length changes were measured continuously by the reference cantilever, and fluorescence images of rhodamine-actin (lower inset) in the network were taken at 10 minute intervals. Total fluorescence intensity (crosses) directly correlated with network length as the network elongated, indicating that the average cross-sectional density of the network did not change as the network grew against the applied force.

This finding suggests that network density is independent of extrinsic variables such as network length and depends solely on opposing force, which sheds light onto the dynamics of the actin cytoskeleton in motile cells experiencing stable loading conditions. This combination of length, force, and fluorescence measurement capabilities provides a platform for quantifying how average network density changes as a function of force and as a function of time when the network is subjected to various loading conditions.

3.6 Discussion & conclusions

The instrument presented here employs a differential cantilever geometry in which two cantilevers on a single substrate were used to stabilize AFM measurements of force and distance. The stabilization geometry we describe is conceptually similar to that used in Altmann *et al*. *(129)*, though we measure beam-bounce deflection through a single objective lens that can be used for simultaneous imaging and alignment of the cantilevers. Furthermore, our instrument is targeted at biological processes that operate over significantly longer times (at larger forces) than the ~10 second stability necessary for force spectroscopy measurements of protein unfolding *(129)*. In the stability demonstrations from Altmann *et al*. the authors utilize a feedback loop in which the reference cantilever alone provides the feedback signal for drift stabilization over short timescales, which neglects spontaneous differential cantilever drift between the two cantilever sensors over longer timescales. We show that both sources of drift can be addressed by employing a position clamp using differential feedback, achieving a 2 order of magnitude improvement in precision over the case without differential feedback. To our knowledge, this is the first direct demonstration of drift control between the cantilever substrate and surface over timescales of several hours.

In summary, we have developed an AFM-based differential force microscope for probing coordinated, time-dependent multi-molecule systems with a position stability of 14 nm over 3 hours. In the case of actin network growth, this stability corresponds to measurement uncertainty of less than 4 actin monomers. The ability to measure precise displacements combined with simultaneous time-lapse fluorescence imaging and existing strategies for localization of molecules to the cantilever make this instrument useful for

measuring mechanical and spatial biophysical changes in multi-molecule systems over long times *(143-145)*. In addition to the actin network growth measurements that we present here, the differential force microscope could be used to quantify forces and nanometer-scale displacement during other cellular processes such as filopodia extension, phagocytosis, cytokinesis, and mitotic spindle formation.

3.7 Methods

3.7.1 Differential force microscope components

An optical schematic of the the differential force microscope is shown in Figure 3.1. The entire microscope is constructed horizontally on an optical breadboard housed in an acoustic enclosure (Technical Manufacturing Corporation) and vibrationally isolated with pneumatic support (Newport, Inc.). The main components in the schematic are the lasers, λ1 (λ = 670 nm, Point Source, Ltd.) and λ2 (λ = 635 nm, Thorlabs, Inc.), the closed-loop Z-axis piezoelectric stage (range = 12 μm, accuracy = 0.05 nm, Physik Instrumente, LP), commercial cantilevers (Veeco Metrology, Inc.), position sensitive detectors (PSDs) (Pacific Silicon Sensors, Inc.), and the objectives, OBJ1 (Mitutoyo, 10x, 0.28 NA) and OBJ2 (Zeiss, 32x, 0.4 NA). All other components were purchased from standard optics suppliers (Thorlabs, Inc. and Edmund Optics, Inc.) or custom made. The entire instrument is controlled with custom written software in LabView (National Instruments, Inc.)

3.7.2 Protein preparation

Actin was purified from rabbit skeletal muscle *(146)*, labeled on random lysines with NHS-rhodamine (Pierce Biotechnology, Inc.), and cycled repeatedly to ensure polymerization competency. *Xenopus laevis* extract was prepared as previously described *(43)*. Following isolation, crude extract was ultracentrifuged for clarification, aliquoted, and stored at -80°C. Extract mix was prepared by diluting the extract to 50% with *Xenopus* buffer (100 mM KCl, 0.1 mM $CaCl_2$, 2 mM $MgCl_2$, 5 mM EGTA, 10 mM HEPES pH 7.7), spin-filtering through 100 nm pores (Millipore) to remove large particulates, and adding 37.5 µl of 50% extract to 1.7 µl of energy mix (150 mM creating phosphate, 2mM EGTA, 20 mM $MgCl_2$, 20 mM ATP pH 7.4) and 2 µl of rhodamine-actin (2 mg/ml).

3.7.3 Actin network force-clamp measurements

The measurement cantilever had a stiffness of 20 pN/nm and the reference cantilever had a stiffness of 30 pN/nm based on the manufacturer value and confirmed with thermal noise measurements (Figure 3.2C) *(124)*. The cantilever was functionalized by dipping the end into a solution of ActA (0.4 mg/ml) for 30 seconds, placed in a fluid cell, and immersed in *Xenopus laevis* extract after the surface was moved within ~100 µm of the cantilevers. Subsequently, cantilever deflection was calibrated, and the surface was finely adjusted with the piezoelectric stage until the desired force was reached on the measurement cantilever, after which data acquisition, force-feedback, and time-lapse fluorescence microscopy commenced. Data was anti-aliased at 50 Hz (Krohn-hite, Inc.), recorded at 100 Hz using a PCI-6036E data acquisition board (National Instruments,

Inc.), used for real-time software-feedback, and saved for offline processing in Igor Pro 5 (Wavemetrics, Inc.).

3.8 Acknowledgements

We would like to thank M.J. Rosenbluth and J.W. Shaevitz for helpful discussions and the entire Fletcher laboratory for support. This work was supported by a Achievement Rewards for Collegiate Scholars fellowship S.H.P., a National Science Foundation (NSF) and National Defense Science and Engineering fellowship to O.C., a Natural Sciences and Engineering Research Council of Canada fellowship to A.P.L., and an NSF CAREER Award and National Institute of Health grant to D.A.F.

CHAPTER 4: LOADING HISTORY DETERMINES THE VELOCITY OF ACTIN NETWORK GROWTH

Reprinted with permission Nature Publishing Group from article "Loading History Determines the Velocity of Actin Network Growth" by Sapun H. Parekh, Ovijit Chaudhuri, and Daniel A. Fletcher in *Nature Cell Biology* **7**(12): 1219-1223, December 2005.

4.1 Abstract

Directional polymerization of actin filaments in branched networks is one of the most powerful force-generating systems in eukaryotic cells *(30)*. Growth of densely cross-linked actin networks drives cell crawling *(16)*, intracellular transport of vesicles and organelles *(147, 148)*, and movement of intracellular pathogens such as *Listeria monocytogenes (149)*. Using a modified atomic force microscope (AFM), we obtained force-velocity (f-v) measurements of *in vitro* growing actin networks through stall. We found that the growth velocity of a branched actin network against increasing forces is load independent over a wide range of forces prior to a convex decline to stall. Surprisingly, when force was decreased on a growing network, the velocity increased to a value greater than the previous velocity, such that two or more stable growth velocities can exist at a single load. These results demonstrate that a single f-v relationship does not capture the complete behavior of this system, unlike other molecular motors in cells, because the growth velocity depends on loading history rather than solely on the instantaneous load.

4.2 Introduction

Over the past decade, *in vitro* reconstitution of actin-based motility using bacteria and functionalized micron-sized beads *(43)* has led to the characterization and identification of proteins essential for directed movement *(150)*. However, the physical basis and regulation of force generation by branched actin networks is still under debate *(151)*. Conversion of chemical energy into mechanical work by molecular motors or

filament polymerization is typically characterized by f-v relationships, which describe velocity in a given biochemical system as a function of only the instantaneous applied force *(152)*,*(153)*. Multiple theoretical models posit such f-v relationships for growing actin networks *(60, 61, 66, 67, 154)*, but the predictions of these models vary widely because of different assumptions about the effects of filament branching and capping, network elasticity, and network-load tethering. McGrath *et al. (71)* and Wiesner *et al. (72)* have reported f-v relationships using reconstituted motility assays of *Listeria* and beads, respectively, in which the viscoelasticity of the medium was varied to control the drag force. More recently, Marcy *et al.* directly measured a f-v relationship for actin network growth using a glass microneedle force probe *(65)*. Both the *Listeria (71)* and glass microneedle *(65)* experiments show a concave decline in velocity with increasing force as predicted by the tethered Brownian ratchet *(61)* and elastic gel *(66)* models. However, no previous work has stalled actin network growth. Consequently, the extent to which the full force-velocity landscape has been measured is unknown, making the interpretation of these results difficult and raising questions about the behavior of actin networks under higher loads approaching stall.

Here we present measurements of actin network growth through stall against a flexible cantilever in a differential AFM assay that uses two cantilevers to measure displacement over long times. In each experiment, the nucleation promotion factor ActA was nonspecifically adsorbed onto one cantilever (see Methods), initiating formation of a localized, branched actin network between the cantilever and a nearby surface *(68)* (Figure 4.1A). The second cantilever is used to compensate for unpredictable drift

between the surface and cantilevers to ensure spatial stability throughout the experiment (see Methods, Figure I.1).

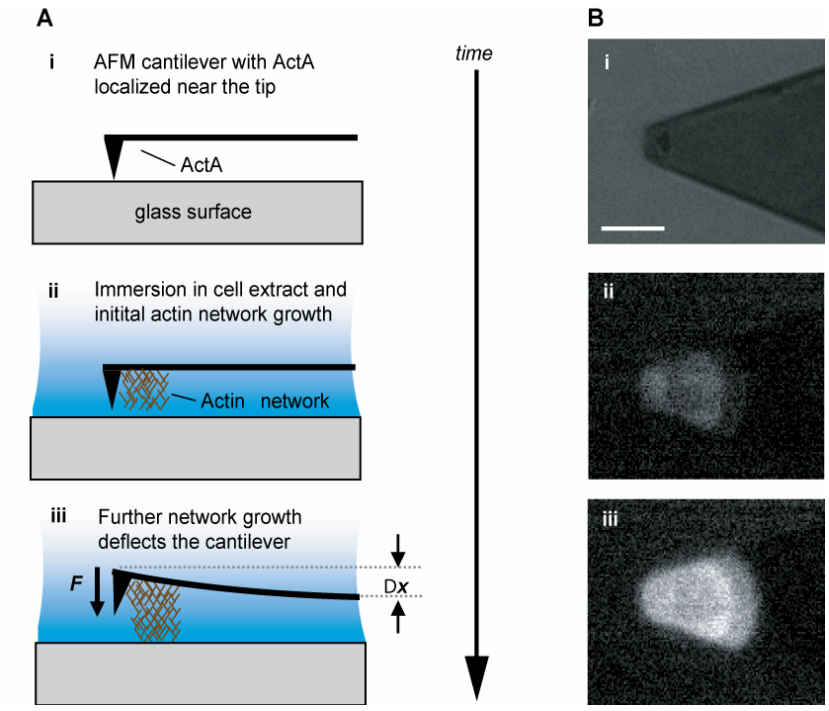

Figure 4.1 Growth of an actin network from an AFM cantilever.

(A) Illustration of the experimental geometry. (i) A cantilever functionalized with ActA is mounted in a fluid cell and positioned near a glass surface. (ii) *Xenopus laevis* cytoplasmic extract mix is delivered to the fluid cell and forms a liquid chamber in which the cantilever is immersed. Upon immersion, ActA activates the Arp2/3 complex, which initiates formation of a branched actin network. Actin polymerizes at the cantilever surface pushing the existing network towards glass surface. (iii) After the network reaches the glass surface, further growth deflects the cantilever, Δx, which is monitored by an optical lever (not shown). The deflected cantilever behaves like a spring, exerting a restoring force proportional to its displacement, or $F = k\Delta x$, where k is the stiffness of the cantilever. **(B)** Images of a cantilever before and during polymerization. (i) Brightfield image showing the triangular end of the cantilever. (ii) Fluorescent image of rhodamine labeled actin growing from the cantilever during the initial stages of actin network growth. (iii) Fluorescent image of the actin network at a later time. Scale bar is 10 μm.

4.3 Results and Discussion

We measured actin network growth from the actin-associated cantilever deflection, using an optical lever design sensitive to nanometer-scale displacements. While actin polymerization resulted in both cantilever deflection and compression of the existing network, compression is expected to be small and is not considered in further analysis (APPENDIX I:). Network growth was monitored simultaneously with epi-fluorescence imaging of labeled actin (Figure 4.1B). This force microscopy technique offers several key features: (i) capability of exerting forces up to several hundred nN, (ii) active adjustment of the load on the actin network during an experiment, (iii) a flat nucleating surface to avoid ambiguities caused by surface curvature *(155)*.

First, we measured the f-v relationship by allowing the growing actin network to naturally deflect the cantilever. Because a cantilever exerts a restoring force proportional to its deflection, the actin network grew against increasing forces until growth stopped at the stall force, similar to single molecule studies with optical traps *(156-158)*. A typical result is shown in Figure 4.2A where the actin network exhibited three different growth phases. Initially, there was a developmental phase where the network growth velocity increased against increasing forces (Figure 4.2A, I). This developmental phase was also seen in constant force experiments, indicating that it is a transient phenomenon, and it was excluded from further analysis (APPENDIX I:, Figure I.2). Following this was a load-independent phase where the network length increased linearly with time against an increasing force (Figure 4.2A, II). The actin network in Figure 4.2 grew at a velocity of ~72 nm/min over a 50-160 nN range. Finally, the network entered a stall phase, where the rate of network elongation slowed until it stalled at a force of 294 nN corresponding

to a pressure of ~1 nN/μm^2 (Figure 4.2A, III). In order to demonstrate that the observed stall was indeed force-dependent and not due to depletion of protein components, we reduced the force on the stalled network after which the network resumed elongation (APPENDIX I:, Figure I.3).

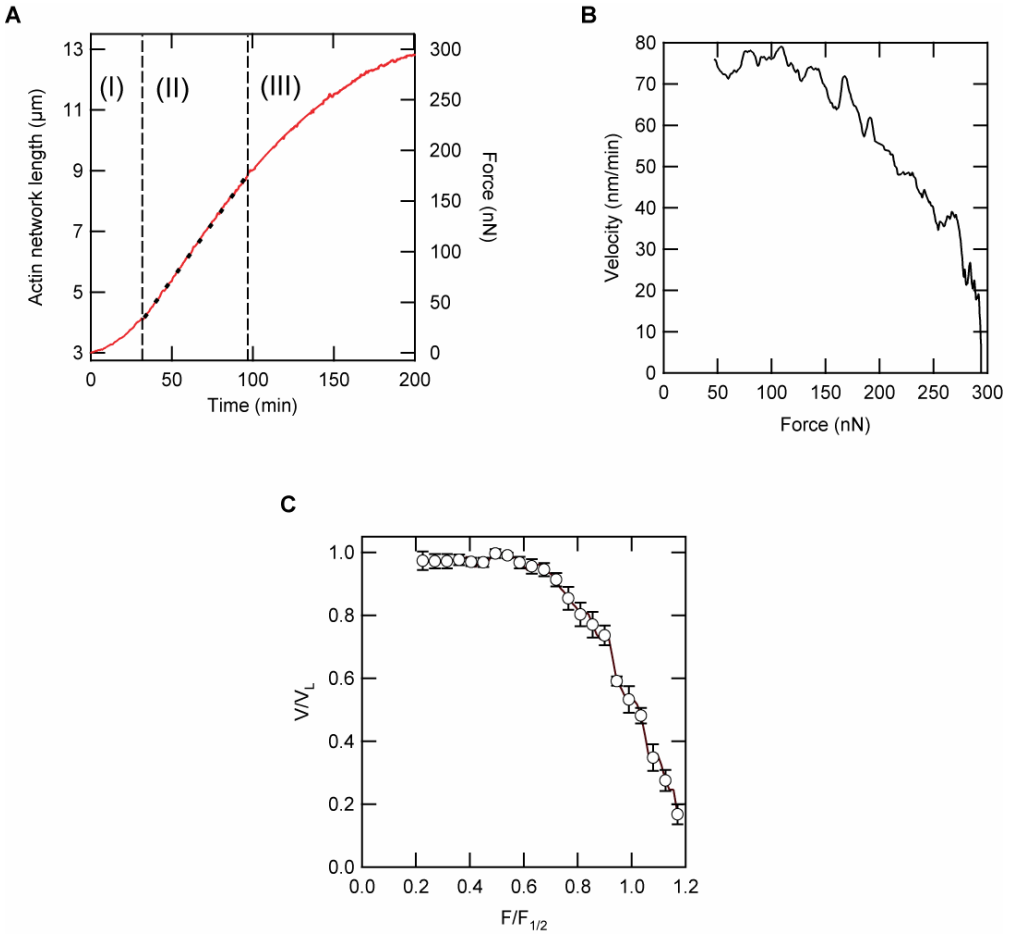

Figure 4.2 Force-velocity relationship of actin network growth under increasing forces.

(A) Length-force-time plot from a single experiment. Network length includes an extra 3 μm in addition to cantilever deflection to account for the cantilever tip spacing. The entire force-time trace is shown in red with the vertical dotted lines marking the transitions between phases I, II, and III. The black dotted line superimposed on the red trace in phase II is a linear fit ($R^2 = 0.999$) to highlight the load-independence of this phase. **(B)** Force-velocity relationship for the experiment in (A) showing the load-independent (II) and stall (III) phases. The transient developmental phase (I) is not included (APPENDIX I:, Figure I.2).

Briefly, the growth velocity is obtained by differentiating the deflection-time curve using a Savitzky-Golay filter and plotted versus a Boxcar-smoothed force axis. **(C)** Average normalized force-velocity plot from n = 10 experiments, showing an essentially constant velocity spanning more than a third of the total force range. Individual runs were normalized by V_L and $F_{1/2}$, and averaged at the indicated $F/F_{1/2}$ values. Individual normalized velocity values are shown as mean ± s.e.m. (see Methods).

From measurements of length and force over time, we computed the f-v relationship by differentiating length records to obtain growth velocity. A single f-v trace, based on the experiment in Figure 4.2A, is shown in Figure 4.2B. As indicated by the dashed line in Figure 4.2A, the network growth velocity remained essentially load-independent for more than a third of the force range. This load-independent phase is followed by a convex decline in velocity until stall. Stall forces (150 ± 120 nN, mean ± s.d., n = 10) and load-independent velocities (85 ± 68 nm/min, mean ± s.d., n = 10) varied significantly among trials primarily due to variations in ActA density and coverage area. However, after normalizing the velocity and force for each individual record, all f-v curves collapsed onto each other. This suggests that the average normalized f-v trace (Figure 4.2C) represents a characteristic behavior for actin networks growing against increasing loads, which is independent of network area as well as cantilever stiffness. This curve illustrates both the load-independent growth and convex stalling behavior.

Several models of actin-based motility might explain the load-independent behavior seen in Figure 4.2C. One explanation is that network growth is limited not by the applied force but rather by force-independent processes such as the inherent time required for polymerization of actin or nucleation of new filaments *(54, 154, 156)*. Alternatively, it is possible that remodeling of the actin network during growth by

increased branching, for example, is responsible for the load-independent regime. The autocatalytic model for actin growth posits a mechanism whereby the density of filaments increases with force to keep the velocity constant *(67)*. An increase in force causes a transient decrease in network growth velocity thus allowing more time for filament branching at the load surface. This enhanced branching increases the density of filaments at the load surface so that the force per filament remains constant with increasing load resulting in a constant velocity.

In order to differentiate between these explanations we performed the following force-reduction experiment (Figure 4.3A). The network was allowed to grow until it reached a force of 145 nN with a load-independent velocity of ~129 nm/min. We then reduced the applied load to 120 nN – still within the load-independent regime – by gradually retracting the surface with a piezoelectric stage (see Methods). Following the force-reduction, the load was clamped at 120 nN, and the growth velocity was measured. If force-independent kinetics determined the growth velocity from 120 up to 145 nN, then the velocity at 120 nN should not change following a force reduction. On the other hand, if the network has undergone structural remodeling as in the autocatalytic model, then the growth velocity would be greater after the force is reduced, but only for a short time. For the experiment shown in Figure 4.3A, a force decrease of 17% led to a 2.1 fold increase in velocity to 275 nm/min. Surprisingly, this velocity persisted for more than 10 minutes (or almost 3 μm of growth). In all force-reduction experiments the growth velocity after a 17 – 98% (n = 8) force reduction was found to stabilize at a value 1.75 – 10.9 (mean = 3.7) fold higher than the original velocity and persist for as long as data was recorded, 1-4 μm and up to 30 minutes.

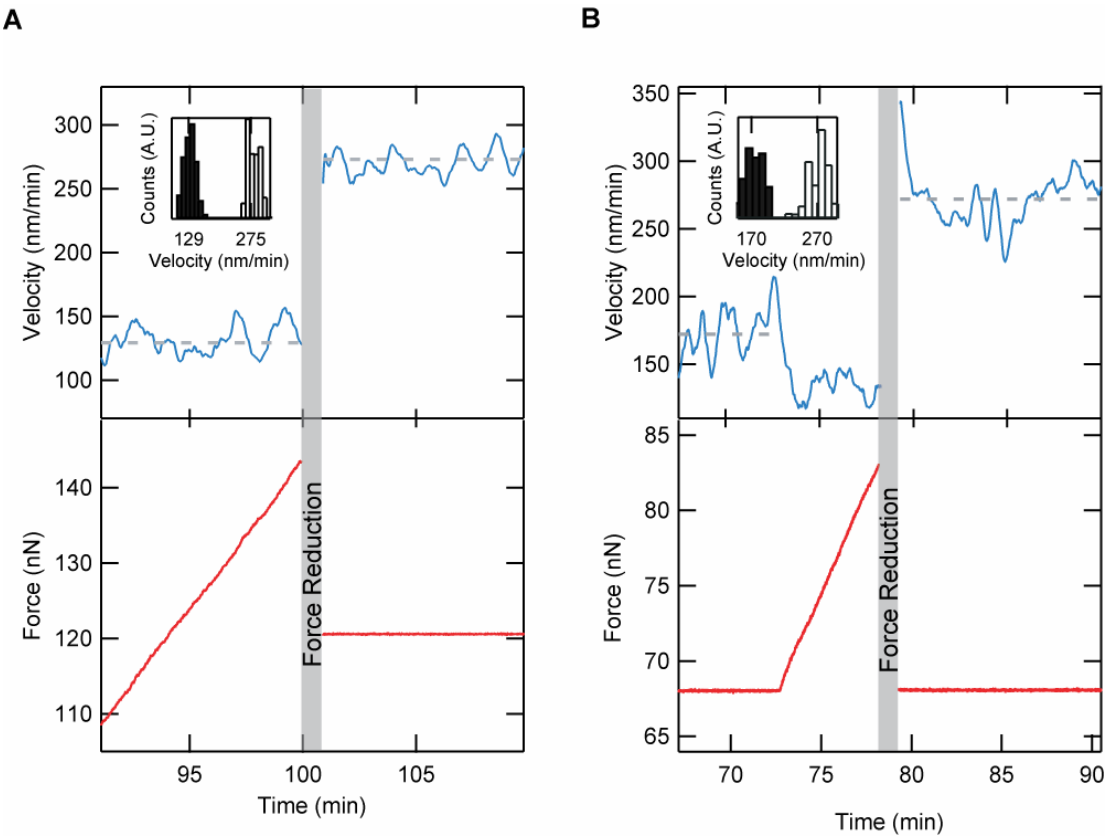

Figure 4.3 Force-reduction experiments showing two stable velocities at a single force.

(A) Actin network growth proceeded until the load-independent phase was reached, during which the growth velocity (blue) was ~129 nm/min. At t = 100 minutes the force (red) on the network was reduced from 145 nN to 120 nN, and the force was clamped at 120 nN. The average growth velocity (grey dotted line) following the force reduction increased to approximately 275 nm/min, which is ~2.1 fold greater than the velocity of network growth previously at 120 nN. This growth velocity persisted for more than 10 minutes (3 μm). Inset, Histogram of growth velocity in load-independent phase (black bars) and after force reduction (open bars). **(B)** Same color legends as in (A). Force exerted on the network was initially held constant at 68 nN, then allowed to increase naturally at t = 73 minutes (slight decrease in velocity). When the force reached 83 nN at t = 79 minutes, the force was reduced back to 68 nN and clamped. Following a brief decay in velocity, the average growth velocity stabilized at 270 nm/min, which is a 1.6 fold increase over the previous velocity of 170 nm/min. **Inset**, Histogram of growth velocity in force-clamp mode before (black bars) and after (open bars) the force reduction. The experiments shown in (A) and (B) demonstrate multiple stable growth velocities for a single force.

When actin network growth naturally deflects the cantilever in the load-independent phase and experiences an increasing force, kinetic processes such as molecular diffusion and increasing compression at higher forces may influence the velocity of growth in a transient manner. Under a constant force, however, concentrations are stable so that steady-state velocities are measured. To verify the existence of two growth velocities against the same force, we conducted force-clamp-reduction experiments. In these experiments, the force exerted on the network was initially held constant, and the resulting velocity was quantified. The force clamp was then removed and subsequent network growth resulted in increased cantilever deflection and increased force on the network, just as in the previous force-reduction experiments. After this period of increasing force, the force on the network was reduced to the initial value and clamped, and the resulting velocity was quantified. An example of this experiment is shown as Figure 4.3B. In this trial, the velocity during the second force clamp was 1.6 fold greater than the velocity during the first force clamp following a 19% reduction in force. In all force-clamp-reduction experiments (n = 8), the growth velocity was found to increase by a factor of 1.22 to 3.63 (mean = 2.3) following a 20 – 95% reduction in force. Additional control experiments showed that this phenomenon is not dependent on network length (data not shown). These force-clamp-reduction experiments confirm the existence of two steady-state growth velocities against the same load in the same experiment, demonstrating hysteresis in the f-v relationship. Consequently, the velocity of actin network growth at a given force depends on its loading history, and a single f-v relationship can not capture the behavior of this system.

In the autocatalytic model, filament density is governed by the load velocity and adjusts to prevent changes in velocity as force increases or decreases *(67)*. This model is consistent with a load-independent growth velocity (Figure 4.2C) as well as with the increased velocity immediately after a force-reduction (Figure 4.3). However, the autocatalytic model predicts that an instantaneous increase in velocity after force-reduction will be followed by an exponential return to the previous velocity at that force. Rather, we find that an increased velocity after force-reduction continues indefinitely.

4.4 Conclusions

While the predicted return to the previous velocity, V_1, does not occur, increasing filament density with force is a plausible explanation for our observations. In this scenario, the density of filaments increases to sustain a constant force per filament leading to a constant velocity during the load-independent phase as force increases. Following a force-reduction, the density of filaments stabilizes so that a velocity, V_2, greater than V_1 is maintained, rather than exponentially reduced to V_1. At forces above the load-independent regime, the growth velocity begins to roll off as the network approaches a saturating density of filaments, and growth is stalled soon after. This would suggest a crucial role for actin filament nucleation in force production. Previous studies *(65, 71, 72)* have reported increases in actin density with load through fluorescence or phase imaging of actin, which is consistent with our interpretation. Several molecular mechanisms may be responsible for regulating the number of filaments in the network, such as force-dependent branching or capping rates. If the branching or capping rate depends on the force per filament, then increasing the total force on the network could

stimulate a net increase in the filament density. However, simple kinetic models cannot capture the hereditary nature of this system, and other biochemical processes in the extract may influence network organization. Further experiments will be required to elucidate the specific molecular mechanisms involved in remodeling and hysteresis.

Our work shows that under an increasing load, actin network growth is load-independent prior to stall, which is explained by structural remodeling of the actin network, likely due to an increase in the number of working filaments pushing the load. From force-reduction experiments, we find that the f-v relationship for a growing actin network depends on its loading history, unlike the f-v relationships of molecular motors or individual filaments. In moving cells, remodeling of the actin network as result of load may enable immediate cytoskeletal responses to physical obstacles, independent of chemical signaling. The observed load-independent growth regime also suggests that an optimum force range exists in which crawling cells may operate for robust, stable movement.

4.5 Methods

4.5.1 Protein preparation

Actin was purified from rabbit skeletal muscle *(146)*, labeled on random lysines with NHS-rhodamine *(159)* (Pierce Biotechnology), and cycled repeatedly to ensure polymerization competency. *Xenopus laevis* extract was prepared as previously described *(43)*. Following isolation, crude extract was ultracentrifuged for clarification, aliquoted, and stored at -80°C. Extract mix was prepared by diluting the clarified extract to 50% with *Xenopus* buffer (XB) (100 mM KCl, 0.1 mM $CaCl_2$, 2 mM $MgCl_2$, 5 mM

EGTA, 10 mM HEPES pH 7.7), spin-filtering through 100 nm pores (Millipore) to remove large particulates, and adding 37.5 μl of 50% extract to 1.7 μl of energy mix (150 mM creating phosphate, 2mM EGTA, 20 mM $MgCl_2$, 20 mM ATP pH 7.4) and 2 μl of rhodamine-actin (2 mg/ml).

4.5.2 Differential AFM

The differential AFM was developed to increase stability of long time-scale force measurements *(160)*. Briefly, two silicon nitride cantilevers (Veeco Metrology, Inc) were monitored simultaneously with an optical lever design using separate position sensitive detectors (PSD) (Pacific Silicon Sensors, Inc.). The deflection of each cantilever was calibrated with a piezoelectric nanopositioning stage (Physik Instrumente, L.P.). The instrument was controlled using custom software written in LabView 7 (National Instruments). Both cantilever position signals were recorded at 100 Hz (National Instruments), anti-aliased to 50 Hz with an 8-pole Butterworth (Krohn-Hite, Inc.), and saved for offline processing. Software feedback, also at 100 Hz, was used to control the piezoelectric stage and operate the AFM in different modes. Epi-fluorescence imaging was performed using mercury arc-lamp illumination and cooled CCD camera imaging (Qimaging).

The instrument was operated in either drift-clamp or force-clamp mode. In drift-clamp experiments, the actin network was allowed to freely deflect one cantilever while the second cantilever position was held constant by actively controlling the glass surface, thereby negating the effect of thermal drift and other uncontrolled influences. In force-reduction experiments, once the load-independent phase was reached, the glass surface

was gradually retracted at ~100 nm/s. After force reduction, the AFM was operated as a force-clamp by actively controlling the glass surface to maintain a constant force on the actin-associated cantilever. In this mode, the growth velocity is reported by the second cantilever, as it is in contact with the surface and reflects displacement under the actin-associated cantilever.

4.5.3 Force measurements

Force measurements were conducted with a cantilever having a stiffness of either 20 or 30 pN/nm based on the manufacturer value and confirmed with thermal noise measurements *(124)*. The cantilever was functionalized by dipping the end into a solution of ActA (0.4 mg/ml) for 30 seconds. After functionalization, the cantilever was placed in a fluid cell and immersed in *Xenopus laevis* extract mix after a brief positioning period. Subsequently, cantilever deflection was calibrated, and the surface was adjusted to a distance of 200 nm from the cantilever after which data acquisition and time-lapse fluorescence microscopy commenced. Network growth was usually detected after ~ 5-50 minutes. We note that our load-independent velocities were significantly slower than those of motility assays, most likely due to the application of larger forces.

4.5.4 Data analysis

The cantilever voltage signals were converted to deflection using a deflection map and downsampled to 5 Hz for further processing in Igor Pro 5 (Wavemetrics, Inc). Length of the actin network was calculated as the distance between the two cantilevers plus an additional 3 μm due to the size of the tip. Force was determined by multiplying

cantilever deflection by the stiffness. Occasionally (~1-2 times/trial) particulates in the extract mix temporarily obscured the laser signal and the total laser power decreased. These segments were deleted from the data and replaced with values from a 7^{th} order polynomial fitted to the remaining trace. Velocities were obtained from length-time curves by using a Savitzky-Golay filter with a window size corresponding to 6% of the time for each trial *(156)*. Force data used in f-v traces was boxcar-smoothed with a 6.67 minute window. Each f-v trace was normalized by the load-independent velocity, V_L, and force where $V = V_L/2$, which we refer to as $F_{1/2}$, as calculated from a sigmoid fit *(156)*. All normalized f-v curves were averaged to arrive at the average normalized f-v trace.

4.6 Acknowledgements

We thank J.W. Shaevitz, A.P. Liu, and J.L. Choy for helpful discussions and careful reading of the manuscript as well as the entire Fletcher laboratory for support. We are also grateful to R.L. Jeng, C. Le Clainche, and M.J. Footer for assistance in protein preparation. This work was supported by an ASEE NDSEG Fellowship to O.C. and an NSF CAREER Award to D.A.F.

CHAPTER 5: REVERSIBLE STRESS SOFTENING OF ACTIN NETWORKS

5.1 Abstract

The mechanical properties of cells play an essential role in numerous physiological processes. Organized networks of semiflexible actin filaments determine cell stiffness and transmit force during mechanotransduction, cytokinesis, cell motility, and other cellular shape changes *(30, 79, 161)*. While numerous actin binding proteins have been identified that organize networks, the mechanical properties of actin networks with physiological architectures and concentrations have been difficult to measure quantitatively. Studies of mechanical properties *in vitro* have found that crosslinked networks of actin filaments formed in solution exhibit stress stiffening arising from the entropic elasticity of individual filaments or crosslinkers resisting extension *(83, 87, 90, 162)* Here we report reversible stress softening behavior in actin networks reconstituted *in vitro* that suggests a critical role for filaments resisting compression. Using a modified atomic force microscope to probe dendritic actin networks, like those formed in the lamellipodia of motile cells, we observe stress stiffening followed by a regime of reversible stress softening at higher loads. This softening behavior can be explained by elastic buckling of individual filaments under compression that avoids catastrophic fracture of the network. The observation of both stress stiffening and softening suggests a complex interplay between entropic and enthalpic elasticity in determining the mechanical properties of actin networks.

5.2 Introduction

Monomers of actin assemble into polar filaments that are organized by various actin binding proteins into branched, bundled, and/or crosslinked networks essential for basic cellular functions *(30)*. In crawling cells, growth of actin filament networks characterized by a dendritic architecture – highly branched structures with short filaments (~0.1 – 1 μm) oriented in the direction of migration – generates force at the cell periphery for membrane protrusions *(30, 38, 41)*.

Actin filaments, as well as other biological and synthetic polymers, are categorized by the relationship between their persistence length, L_p, and contour length, L_c. The persistence length is defined as the average length over which the filament orientation changes due to thermal fluctuations, and the contour length is the length of the completely extended filament. For flexible polymers ($L_c \gg L_p$) the resistance to extension and compression is determined by the conformational entropy of the chain, which is described as entropic elasticity. Near full extension they exhibit increasing elasticity with extension, or stress stiffening, because extension reduces the conformational entropy of the chain *(77)*. In contrast, the elasticity of stiff polymers ($L_c \ll L_p$) arises from resistance to bending, stretching, and compression due to straining of molecular links from equilibrium, which is quantified by the bending modulus and termed enthalpic elasticity. Under compressional forces, stiff polymers buckle at the Euler buckling force, $F_b = \frac{\pi^2 \kappa}{L_c^2}$, where κ is the bending modulus *(75)*, whereas there is no equivalent buckling instability for flexible polymers because random thermal forces exceed the Euler buckling force. Actin filaments are considered to be semiflexible polymers because their

persistence length (~ 10-17 μm) *(75, 162)* is comparable to their physiological contour length (~ 0.1 to 10 μm) *(38)*. At physiological temperatures, individual filaments are expected to exhibit a combination of both entropic and enthalpic elasticity that is sensitive to the ratio of L_c to L_p *(163)*.

The mechanical properties of actin networks have been studied extensively using rheology of random networks formed by mixing purified actin and various actin binding proteins in solution *(79, 83, 87, 90)*. Recent studies have demonstrated stress stiffening of crosslinked actin networks *in vitro* under shear and explained this behavior as arising from the inherent stress stiffening of individual filaments or flexible crosslinkers between filaments under extension, suggesting the elasticity of these networks is entropic *(83, 87, 88)*. Filaments resisting compression have not been found to be important *(87)*. However, as filament length decreases from lengths seen in these *in vitro* assays (~2-70 μm) to physiological values, filaments are expected to support more significant bending and compressional forces *(163)*. Indeed, the increasing importance of enthalpic elasticity has been predicted for high concentrations of actin and crosslinkers when the distance between crosslinks becomes small *(83, 164)*. Here we report that dendritic actin networks reconstituted *in vitro* exhibit a regime of reversible stress softening. This stress softening can be explained by the elastic buckling of individual filaments, providing evidence for an elastic response of dendritic actin networks that is enthalpic under large compressional forces and dominated by resistance of individual filaments to compression.

5.3 Results and Discussion

We studied the mechanical properties of growing dendritic actin networks *in vitro* using a recently developed dual-cantilever atomic force microscope (AFM) that uses a second cantilever to improve instrument stability (see APPENDIX II:) *(74)*. Dendritic networks, like those formed during cell motility, must be assembled hierarchically from a nucleating surface and cannot be formed randomly in equilibrium solutions of component proteins. In our assay, the nucleation promotion factor ActA, from the bacterial pathogen *Listeria monocytogenes,* was nonspecifically adhered to the end of an AFM cantilever prior to immersion in cytoplasmic extract from *Xenopus laevis* eggs. Upon immersion, ActA activates the Arp2/3 complex, which nucleates growing filaments as 70^{o} branches off of existing filaments, catalyzing the formation of a growing dendritic actin network between the cantilever and a nearby glass surface (Figure 5.1A,B) *(30, 38, 165)*. Surfaces coated with ActA and other nucleation promotion factors have been shown to grow dendritic actin networks in cytoplasmic extract *(43, 165)*. The AFM cantilever behaves like a Hookean spring for small deflections (for which $F = k\Delta x$), allowing measurement and application of compressional forces to the growing network.

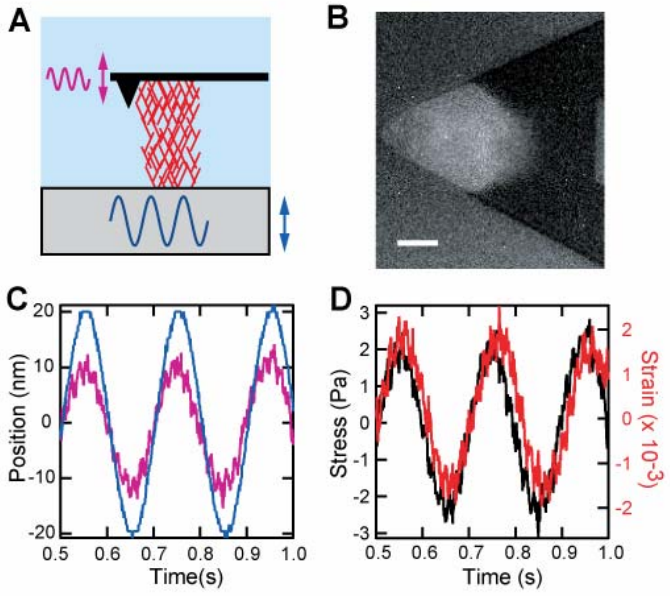

Figure 5.1 AFM-based microrheology of growing dendritic actin networks.

(A) Cartoon illustrating the measurement geometry in which the surface is driven sinusoidally (blue sinusoid/ arrowheads), and the force transmitted through the network (red mesh) is transduced by the cantilever (magenta sinusoid/arrowheads). **(B)** Fluorescence micrograph of the actin network, which is used to calculate network area, *A*. Scale bar is 10 μm. **(C)** Surface and cantilever displacement graph showing surface drive and cantilever response signal as a function of time for a 5 Hz measurement (colors are same as in (A). Note the cantilever response is damped with respect to the drive signal indicating compression of the network. This technique has the effect of applying a sinusoidal stress on the network where hydrodynamic coupling was found to be negligible (see APPENDIX II:). **(D)** Stress and strain graph calculated from measurement in (C) showing stress (black) and strain (red) as a function of time (see Methods).

Using AFM-based microrheology (Figure 5.1C,D, Methods), we measured frequency-dependent elastic, or storage, and viscous, or loss, moduli. After normalization at a reference frequency (see APPENDIX II:), we find that the frequency dependence of the elastic modulus, *E'*, is consistent with power law rheology, $E' \propto f^x$,

with $x = 0.13$ (Figure 5.2). This falls within the range of exponents measured from cells ($x = 0.12$ - 0.25) *(80, 166, 167)*.

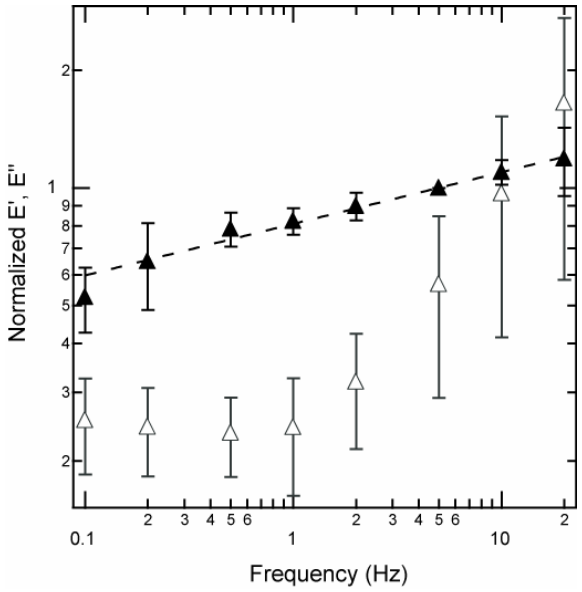

Figure 5.2 Frequency dependence of elastic (filled triangles, *E'*) and viscous (open triangles, *E''*) moduli.

The traces were constructed by averaging normalized data from 11 separate experiments and 21 different measurements. Each measurement of the elastic and viscous moduli was normalized by the average elastic modulus at 5 Hz taken before and after the measurement (see APPENDIX II:). The best fit power law exponent for *E'(f)* was determined to be $x = 0.13$ (dotted line), and the average elastic modulus at 5 Hz was 985 ± 655 Pa (mean ± s.d.), which are consistent with previous studies on cells. In addition to the power law behavior, the viscous modulus has a similar shape to those seen previously. Error bars on both curves are normalized s.d.

The average linear elasticity of the dendritic actin networks, 985 Pa ± 655 Pa (mean ± s.d.) at 5 Hz, is similar to the elastic modulus measured on various cell types *(80, 81, 166, 167)* and in a previous reconstitution of actin based motility *(65)*. Dendritic actin network elasticity is significantly higher than the elasticity of actin networks

reconstituted in solution containing the Arp2/3 complex (~1 Pa), though differences in concentration and components could account for this disparity *(85, 168)*. The average elasticity of the actin networks studied here was found to be independent of prestressing by myosin II motors (see APPENDIX II:).

In order to further understand the mechanical properties of growing dendritic actin networks, we probed the stress dependence of the elastic modulus *(83, 88)* (see Methods). A typical experiment is shown in Figure 5.3A (black trace) where stress was increased on the network incrementally, and the elasticity at each value of applied stress was measured. For stresses up to ~ 15 Pa the elasticity remained constant, indicating a linear elastic regime. Then the elasticity increased with stress in a stress-stiffening regime, as has been seen previously *(83, 87, 90)*, for stresses up to a critical stress, σ_c ~ 270 Pa. Above the critical stress, we found that the elasticity of the network gradually decreased with stress in a stress-softening regime.

Stress softening has been previously explained by network rupture or crosslinker rearrangement. In rigidly crosslinked actin networks, stress softening has been attributed to the fracture of extended filaments or crosslinking/branch points at σ_c, after which elasticity drastically decreased *(83, 87, 90)*. Alternatively, softening was proposed to occur due to unbinding of flexible crosslinkers above σ_c, which either remain unbound or re-bind to form crosslinks at different positions *(88)*. Under either of these explanations, stress softening reflects permanent alterations in the network that would lead to irreversibility in the elasticity of the network. That is, higher elasticities could not be recovered by reducing network loading from stresses above σ_c *(83, 87, 88, 90)*. However in dendritic actin networks, the stress softening behavior was reversible, as the elasticity

measured as the stress was reduced to σ_c matched that seen for increasing stress (Figure 5.3A, red trace). This was seen in all experiments (Figure 5.3B), requiring that stress softening in the dendritic actin network must arise from a reversible mechanism.

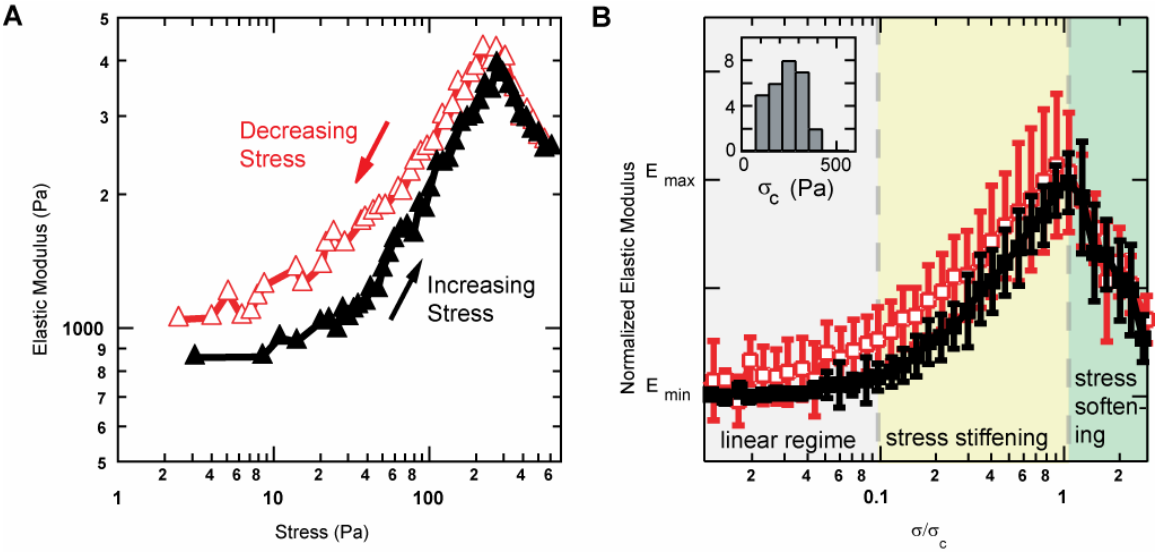

Figure 5.3 Dendritic actin networks exhibit stress stiffening and reversible stress softening.

(A) In a typical nonlinear elasticity measurement, the stress on the network is first increased incrementally (black trace) to and then decreased incrementally from a maximum stress (red trace) of ~600 Pa, with the elasticity measured at each stress at 5 Hz. The elasticity remains constant for stresses up to ~15 Pa and then increases in a stress-stiffening regime. For stresses above the critical stress, σ_c, of ~270 Pa the elasticity decreases in a stress-softening regime that is reversible as indicated by the overlay of the black and red traces. **(B)** Averaged and normalized trace of the nonlinear elasticity of actin networks (see APPENDIX II:). Each individual measurement was normalized by the difference between the elasticity before the measurement, E_{min}, and the maximum elasticity for increasing stresses, E_{max}, and the stress, σ_c, at which the maximum elasticity was achieved for increasing stresses. The results of 28 different measurements from 12 separate experiments were averaged together (mean +/- s.d. shown) and found to exhibit three distinct regimes of elasticity: linear, stress stiffening, and stress softening. The stress softening is shown to be reversible. Note that the elasticity in b is shown on a linear scale while the elasticity in a is shown on a log scale. **Inset**: Histogram of σ_c, for which the average was 233 Pa.

A plausible explanation for reversible stress softening is through elastic buckling of individual filaments under compression. A population of filaments in the dendritic network, based on their length and orientation, will begin to buckle at a threshold stress. Upon buckling, these filaments are infinitely compliant while still supporting F_b *(169)*. As a result, the number of load-bearing elements decreases for higher stresses, resulting in a decrease in the effective stiffness of the network. As the stress is increased, more filaments buckle, reducing the elasticity of the network further. Because filaments are assembled into an interconnected dendritic network, buckled filaments do not collapse completely, and they can unbuckle when the force is reduced making the process of buckling reversible with load. Stress softening has been predicted from simulations of athermal crosslinked actin networks due to filament buckling and in an elastic element model of the cytoskeleton *(170, 171)*, though these models do not predict stress stiffening before softening. Interestingly, reversible elastic buckling of component elements is observed under high compressional forces in some types of foams *(172)*. Electron micrographs have shown the actin cytoskeleton ultrastructure to exhibit similarities with open lattice foams, so that this buckling behavior might be expected *(161)*.

Buckling of individual filaments can occur at forces consistent with the observed stress softening, based on a simple calculation. Using published electron micrographs of dendritic actin networks reconstituted *in vitro* in a similar biochemical system, we estimate filament lengths L_c to be from 0.1 μm to 1 μm *(165)*. We calculate an expected buckling force F_b of 0.5 – 50 pN per filament using these lengths and assuming Euler buckling, though the behavior in a constrained environment can lead to higher buckling

forces *(173)*. In our experiments, the average force per filament at σ_c (233 Pa, mean from Figure 5.3B, Inset), using an average filament spacing of 50 – 100 nm *(165)*, is calculated to be 0.45 – 2 pN, which lies within the lower range of predicted buckling forces. We note that the buckling instability is smoothed entropically for a semiflexible polymer at finite temperature, so that individual polymers will undergo stress softening as the compressional force approaches the Euler buckling force. The overlap in the lower range of predicted buckling forces with the range of calculated applied force per filament at σ_c supports the idea that buckling explains stress softening, as σ_c represents the threshold force at which filament buckling dominates nonlinear elasticity. As the stress is increased, up to 3 σ_c in our experiments, shorter filaments buckle, and the elasticity decreases further.

5.4 Conclusions

Our measurements of nonlinear elasticity in dendritic actin networks are consistent with a model in which a combination of compression, bending, and extension gives rise to network mechanical properties (Figure 5.4).

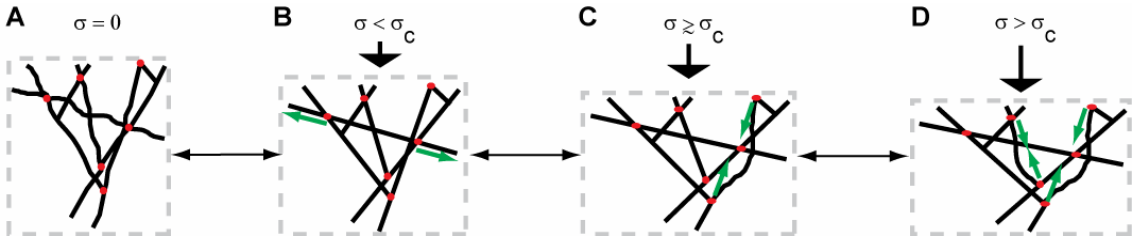

Figure 5.4 Stress stiffening and stress softening can arise in dendritic networks due to filaments resisting extension and buckling of filaments resisting compression.

(A-B) When the stress on the network (σ, indicated by black arrows) is increased from $\sigma = 0$, a population of filaments or crosslinkers is stretched (as indicated by green arrows) as the material expands laterally, and the resistance to extension of filaments increases due to entropic elasticity, leading to a stress stiffening regime. **(C)** However, when the stress is increased above σ_c, some filaments resisting compression buckle when the compressional force (green arrows) exceeds the Euler buckling force. Buckled filaments exhibit infinite compliance so that they no longer contribute to the elasticity, but they do not collapse due to connections with the network and thus still support the buckling force. **(D)** As the stress is further increased, more filaments buckle and the elasticity of the network is decreased further, leading to the stress softening regime. In principle, this process is completely reversible because buckled filaments will unbuckle once the stress is reduced.

As stress is initially applied to the network, the elasticity increases as a result of entropic resistance to filament and flexible crosslinker extension normal to the direction of compression, in addition to possible effects from nonlinear compliance of the Arp2/3 complex (Figure 5.4A-B). As stress on the network is further increased, filaments oriented in the direction of compression begin to buckle, reducing the elasticity of the network at higher stresses (Figure 5.4C-D). Since buckling occurs only after filaments have already been supporting a load, the enthalpic resistance of filaments to compression is likely to play a significant role in the linear and stress stiffening regimes.

The difference in the elasticity of dendritic networks grown from surfaces and crosslinked networks formed in solution can be partly explained by the actin concentration in the network. The modulus of elasticity is expected to scale as $E' \sim C_A^{5/2}$ (ref 8) for isotropically crosslinked actin networks, where C_A is the concentration of actin in the network and the crosslinks are assumed to be rigid. The concentration of actin in dendritic networks has been estimated to be ~1 mM *(33)* while the concentration of networks studied *in vitro* was of order ~10 μM *(85, 168)* suggesting that the magnitude of elasticities for dendritic networks should be significantly higher. Component concentration alone is sufficient to describe network properties in flexible polymer networks ($L_c \gg L_p$), where L_p is much less than the distance between crosslinks, because initial orientation and lengths of the filaments do not matter. However, for semiflexible polymer networks, filament length can be important when L_p is greater than the distance between crosslinks *(164)*. Additionally, the particular orientation of a filament in the network determines whether the filament deforms by compression, bending, or extension. Our finding of an elastic response in which filaments resisting extension and compression are both significant, suggests that architecture – filament length and orientation – influences the elastic behavior of actin networks.

The reversible elastic behavior and large elastic modulus of dendritic actin networks indicate that these networks have an architecture that is geared towards bearing high compressive loads. Since the leading edge of crawling cells is normally under compression during motility, we expect these measurements to be relevant to the mechanics of lamellipodial protrusions. Dynamic remodeling of dendritic actin network

architecture may provide a mechanism for altering network elasticity in response to changing external loads.

5.5 Methods

5.5.1 AFM-based microrheology

In AFM based microrheology, the deformation of the material is measured in response to a small sinusoidal stress at a given frequency, f *(80, 81)*. The elastic modulus, *E'*, and the viscous modulus, *E''*, are then calculated as $E'(f)+iE''(f)=\tilde{\sigma}(f)/\tilde{\varepsilon}(f)$, where $\tilde{\sigma}$ and $\tilde{\varepsilon}$ are the Fourier transforms of the stress, σ, and the strain, ε, respectively (Figure 5.1D). This method is necessary for growing actin networks because only the response at the drive frequency is analyzed, thereby decoupling mechanical property measurements from network growth. Changes in network length due to growth over measurement timescales (~ 5 minutes) would obscure the true strain values needed for traditional stress-strain measurements.

After the network length reached ~ 6 μm while growing under a small constant force, the force clamp (see APPENDIX II:) was released and the bottom surface was sinusoidally oscillated with an amplitude of 20 nm at 0.1, 0.2, 0.5, 1, 2, 5, 10, and 20 Hz using the piezoelectric positioner. This applies a sinusoidal stress to the network where hydrodynamic coupling was found to be negligible (see APPENDIX II:). At each frequency, the surface was oscillated 10 times and the cantilever deflection data was used to calculate both the σ and ε on the network, which are shown in Figure 5.1 *(80, 81)*.

5.5.2 Stress dependence measurements

We adapted a technique to quantify the stress dependence of elasticity used by Gardel *et al.* on crosslinked random actin networks to our AFM-based system *(83, 88)*. Because the relaxation processes are very slow ($x \sim 0.13$), the elasticity at a given stress changes very slowly, and this technique provides a well defined stress-elasticity relation. In this technique, the bottom surface was incrementally stepped into (or away from) the network, and a rheology test at 5 Hz was performed to obtain the elastic modulus as a function of stress on the network. At the beginning of a nonlinear elasticity measurement, the stress on the network was reduced to nearly zero, and a 5 Hz rheology test was conducted. We incrementally increased the force on the network, and obtained the elastic modulus at each incremental stress. The stress on the network was increased until ~ 600 Pa, after which we incrementally decreased the stress on the network by moving the bottom surface away from the cantilever, continuing to conduct 5 Hz rheology tests after each step. Subsequent tests on the same network were started at a stress of zero.

5.5.3 Data Analysis

In each measurement, the cantilever voltage signals were converted to deflection in Igor Pro 5 (Wavemetrics, Inc) using a voltage-deflection calibration constant that was determined at the beginning of each experiment. Length of the actin network was calculated as the distance between the two cantilevers plus an additional 3 μm due to the size of the tip. Force was determined by multiplying cantilever deflection by the stiffness (100 pN/nm). Network area was determined by thresholding the image at a grayscale

value in midway between the highest and lowest value along the cantilever in ImageJ (NIH). There is a 0.1% error in this measurement due to the diffraction limited resolution of the fluorescence imaging.

To obtain the elastic and viscous moduli, the best fit line was initially subtracted from the measurement cantilever deflection to eliminate the effect of slow timescale growth. The elastic (*E'*) and viscous (*E''*) moduli are calculated as $E'(f) + iE''(f) = \tilde{\sigma}(f) / \tilde{\varepsilon}(f)$, where $\tilde{\sigma}$ is the Fourier transform of the stress, $\tilde{\varepsilon}$ is the Fourier transform of the strain of the material, and *f* is the frequency of oscillation. We approximate the geometry of the system as a network sandwiched between two parallel plates so that $\sigma = F / A$ and $\varepsilon = \Delta L / L$, where *F* is the force exerted on the network by the cantilever, *A* is the cross sectional area of the network and *L* is the length of the network. The parallel plate approximation ignores the effect of the pyramidal geometry of the tip because the tip typically represents less than 2.5% of the network area.

Additional methods are described in APPENDIX II:.

5.6 Acknowledgements

We thank J.W. Shaevitz, M.J. Rosenbluth, S. Pronk, P.L. Geissler, and J. Alcaraz for helpful discussions and careful reading of the manuscript as well as the entire Fletcher laboratory for support. We are also grateful to R.L. Jeng and M.J. Footer for assistance in protein preparation. This work was supported by an ASEE NDSEG Fellowship to O.C., an ARCS Fellowship to S.H.P., and an NSF CAREER Award and NIH RO1 to D.A.F.

CHAPTER 6: CONCLUSION

6.1 Overview

This dissertation presents experimental results from the majority of my PhD research in Dan Fletcher's lab UC Berkeley. I spent the better part of 3 years constructing a unique differential force microscope and developing an experimental platform for analysis of growing actin networks (Chapters 2 and 3). This platform was used during years 4-6 to perform a set of experiments on growing dendritic actin networks with nanometer-scale precision (Chapters 4 and 5). Cell crawling and force generation by motile and adherent cells has been the subject of many previous studies, and it will continue to present intriguing questions to future cell biologists, biophysicists, and bioengineers. Actin network force generation occurs during many physiological processes, and along with the work presented in this dissertation, the scientific community has just scratched the surface of understanding the biophysics of this process. Steady progress on the biochemical front and continued innovation in metrology techniques will enable us to better understand "how biology happens" in addition to watching it happen. Cell crawling is a perfect example of this successful partnership; after more than 50 years of biochemical research, we now understand that crawling cells

generate nN forces during motility *(174)* and that dendritic actin network growth is the driving force during lamellipodial protrusion *(65, 74)*.

6.2 Summary of findings

In this dissertation, Chapters 3, 4, and 5 present original engineering/scientific advancement in our understanding of cellular motility and force generation by growing dendritic actin networks. Chapter 3 describes the construction of a differential AFM instrument that overcomes the sensitivity and stability limitations of other force microscopy techniques for probing biophysical systems that generate large forces over long times, such as actin filament networks. Our instrument presented a significant advancement in AFM stability by demonstrating 14 nm absolute position control over measurement times of at least 3 hours. The experimental result in this paper showed actin network growth under constant load results in a network with a constant average actin density.

In Chapter 4, we used this experimental system to investigate the force generating mechanism of overall network growth. That is, our aim was to understand how individual force-generating filaments in the network cooperatively displace increasing loads. Our report was the first to demonstrate mechanical stall of actin network displacement and provide a figure, 1 $nN/\mu m^2$, for the amount of mechanical work that network growth can perform. Furthermore, our results showed that actin networks structurally remodel as they grow under increasing loads, consistent with the autocatalytic model for network growth. While this finding was new, this "adaptive" property is not entirely unexpected because the network is a non-equilibrium system that

is growing and because filament creation depends on the interaction of filaments with the Arp2/3 complex and an NPF. Increased loads could presumably increase the time that filaments spend in the "branching zone" where they are in proximity to surface-bound NPF molecules to increase the rate of filament branching *(67)*. The finding that loading history affects network growth such that multiple stable growth velocities exist at a single load is very surprising because this behavior is different than for other molecular motors or individual filaments and is not predicted by any theoretical model.

While Chapter 4 presented the ability for the network to generate significant force and remodel under opposing loads, Chapter 5 presents the other side of productive actin network growth. As mentioned in Chapter 1, in order to generate productive displacement of a load, the network must be: 1) capable of generating force and 2) generate force against a sufficiently rigid base so that growth is transduced into productive movement of the load rather than compression of the existing network. In Chapter 5, we demonstrated that dendritic actin networks have significantly different mechanical properties than random, equilibrium mixtures of actin filaments and crosslinking proteins. This idea can be understood by considering the organization of I-beams in a building frame. Their length, interconnectivity, and orientation with respect to the load will undoubtedly influence the ability for the frame to resist identical compressive loads. In the same way, short, stiff filaments will resist deformation in a different manner than longer filaments because of the relative contributions of thermal energy and resistance to filament bending. We showed that dendritic actin networks composed of short, inter-connected filaments oriented towards the load exhibit reversible stress softening, which can be explained by buckling of individual filaments in the

network. This was the first demonstration of an actin network mechanical response dominated by bending and buckling in addition to entropic extension.

6.3 Ongoing experimental work and future directions

Understanding the physical forces involved eukaryotic cell motility is a very complex problem. In this dissertation, I have focused only on protrusion and specifically actin network growth during protrusion. While the results presented here shed light onto the physical behaviors and mechanisms at work during protrusive network growth, questions remain about the coupling between biochemical inputs and biophysical output. All actin network experiments described in this dissertation used complex *Xenopus* extract as the protein medium, which offered very little control over biochemical components. A straightforward variation would be to perform very similar experiments in a purified medium.

6.3.1 Force generation

I have begun performing actin force generation experiments in purified proteins with only actin, Arp2/3, capping protein, and profilin in the medium. This mix generates significant force (~100 nN) and grows with a similar velocity to that seen from networks formed from extract media. Besides assessing the raw force generating ability of networks formed from purified proteins, which is very interesting by itself, one could imagine a number of potential experiments. For example, I am currently trying to

understand the mechanistic details that allow dendritic networks to grow at constant velocity against increasing loads. Recall that Chapter 4 presented data showing that network growth against increasing loads results in network remodeling to sustain a constant growth rate. Using position-clamp and force-clamp experiments along with fluorescence imaging of actin and Arp2/3 in a purified protein medium, we have obtained data that shows that actin density may increase with increasing load. Our preliminary data also shows a corresponding increase in the Arp2/3 density, which suggests that the mechanism for network remodeling offered in the autocatalytic model may indeed regulate growth velocity.

Ovijit Chaudhuri and I have successfully constructed a side-view imaging AFM and obtained preliminary data on testing our hypothesis for the loading history dependent growth of dendritic actin networks. Preliminary results from *Xenopus* extract networks show that loading history dependence is coincident with a sustained increase in the density of actin at the load surface, which is consistent with the hypothesis presented in Chapter 4. In future experiments, we have discussed changing the unloading rate and/or amount of force reduction to see how these parameters affect the loading history dependence. Does the velocity increase even when the load is slowly released? How does the absolute force reduction affect the change in network growth velocity?

6.3.2 Mechanics

Additional experiments aimed at understanding how the elastic response (both linear and non-linear elasticity) changes with different degrees of crosslinking and branching will provide new insight into the nature of elasticity in dendritic actin

networks. Gardel *et al*. performed a similar study where they varied the amount of crosslinking, entanglement, and bundling in random networks *(83)*, and we envision that a similar study on purified dendritic actin networks may uncover the architectural qualities that lead to the high elasticity and reversible stress softening behavior seen in Chapter 5 *(37)*. Initially, measuring the elasticity of Arp2/3-branched networks and titrating physiological crosslinking proteins such as filamin, α-actinin, or fascin will be interesting experiments that will uncover scaling laws of $E' = f([branch]/[cross])$ similar to that described by Shin *et al (91)*.

Does branching alone generate networks that possess reversible stress softening? Previous work by Marcy *et al*. suggests that branching may be sufficient to produce large elastic moduli, but doesn't speak to nonlinear elasticity. What will happen if we let filaments in the network get longer by reducing the capping protein? Will the buckling behavior become undetectable? How much will crosslinking change the mechanics?

A parallel set of experiments with these AFM studies would be performing electron microscopy on dendritic networks formed in both purified proteins and *Xenopus* extract. A critical difference between random networks and dendritic networks is the interconnectivity, mesh size, filament length, and orientation with respect to the loading direction. However, our lab has yet to image the ultrastructure of dendritic actin networks grown from cantilever surfaces so we don't actually know what the network looks like. Scanning electron microscopy will confirm whether actin networks nucleated from cantilevers have similar architectural features to dendritic networks in cells and provide measurable quantitative metrics for comparison at different [branch]:[cross] ratios.

Another interesting direction that we briefly considered was to measure network mechanics under varying loads. In Chapter 5, we measured the linear elasticity for networks grown under constant low loads and non-linear elasticity for the same networks. If network growth under increasing load does change the network structure (as hypothesized in Chapter 4), then shouldn't the mechanics also change with load?

6.4 Long term outlook

With nanotechnology receiving significant attention for its potential application in biomedicine, understanding how nanoscale biological machines perform physical tasks should help guide and inspire our engineering pursuits for innovation in nanomedicine. As shown in this dissertation, and by others, dendritic actin networks are robust nanomachines that produce physical work when nucleated in a variety of geometries such as on highly curved *Listeria* or on flat AFM cantilevers. In this way, this system can be considered a module and can be used as one would use a drive train or transmission when designing a car. A possible biomedical application of dendritic network growth is creation of synthetic immune particles to assist platelets during blood clot formation. The basic functionality required for a platelet is the ability to activate and incorporate into a clot upon sensing environmental cues. Activation involves significant morphological changes, and combining the appropriate sensory network with dendritic actin network growth inside a biomimetic capsule could be a promising technology. Sensing an external signal could trigger actin network growth that could deform the particle to allow incorporation into a nearby clot. Current work by Dave Richmond, Ross Rounsevell, Thomas Li, and Jeanne Stachowiak in the Fletcher Lab is focused on encapsulating the

actin force generating system inside biomimetic lipid vesicles to evaluate the feasibility of this and other similar ideas.

In addition to biomedicine, another application for actin networks is their use as etching masks and nanowires for semiconductor processing *(175)*. With photolithography reaching physical limits set by diffraction, biopolymers such as actin filaments can be used to generate patterns with significantly smaller features. Work by Allen Liu showed that actin filaments can be selectively patterned by shining UV light to uncage actin monomers at distinct spatial locations *(176)*. A variation of this technique could potentially be used for creating nanoscale patterns during a fabrication process.

The potential realization of these and other more applied goals will finally resolve the inner struggle that has never left my mind since August 2003: "How can we apply this basic science actin research?" Perhaps I was a bit short sighted 5 years ago, but now I see that the future of actin research, from basic science exploration to application driven technology development, is very exciting. It's funny how things seem to come together in the end, but I suppose that is the reason why we take the journey. I suppose that means it's time for me to dive into the next unknown. Want to go for a swim?

APPENDIX I: SUPPLEMENTARY INFORMATION FOR CHAPTER 4

A. Differential AFM actin measurements

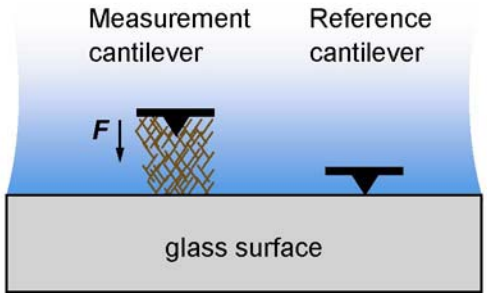

Figure I.1 Cartoon illustration showing the side view of dual cantilever AFM setup.

The reference cantilever is in hard contact with the surface and is used to compensate for unpredictable drift (up to 50 nm/min) over the entire length of the experiment. Actin polymerizes from and deflects the measurement cantilever. This differential approach yields accurate measurements that are not affected by uncontrolled movement between the surface and cantilevers.

B. Elasticity of the actin network

Actin networks are elastic materials and therefore polymerization at the cantilever (nucleating) surface results in both compression of the supporting network and deflection of the cantilever[s1,s2]. Treating the network as compressible spring, the fractional amount of growth transduced by the cantilever is:

$$\frac{\delta}{D} = \frac{k_a}{k_a + k_c} \qquad (1)$$

where δ is the deflection of the cantilever, D is the increase in length of the actin network due to polymerization, k_a is the stiffness of the actin network, and k_c is stiffness of the cantilever. Assuming the network is a homogeneous elastic body with an elastic modulus, E, the stiffness of the network is:

$$k_a = \frac{EA}{L} \qquad (2)$$

where A is the area of the network and L is the length of the network. For example, if E = 3.7 kPa (average from ref. s2), A = 381 μm^2, and L = 8 μm, then k_a = 0.17 nN/nm. In this case, $\frac{\delta}{D}$ = 0.90 and $\frac{\delta}{D}$ = 0.85 for our cantilevers of stiffness k_c = 0.02 nN/nm and k_c = 0.03 nN/nm, respectively. In other words, 90% or 85% of actin polymerization is transduced into cantilever deflection. For both cantilevers, we observe the same characteristics of load-independent growth, convex stall, and increase in velocity following a force-reduction, suggesting that cantilever deflection measurements reflect the behavior of actin network polymerization.

One possible explanation for the observed history dependence in Figure 4.3 is that the network stiffens (k_a increases) with increasing force. In this case, the increased velocity seen after a force reduction is solely due to an increase in cantilever transduction of actin network growth as described above. Taking the extreme case that E = 700 Pa (the lower bound from ref. s2), A = 381 μm^2, and L = 5 μm (average network length during initial force clamp) gives $k_a \sim$ 0.054 nN/nm. For a cantilever stiffness of k_c = 0.02 nN/nm (as used in force-clamp-reduction experiments), the amount of actin growth

transduced throughout the experiment is greater than 73% (Eq.1). Therefore the maximum increase in velocity due to network hardening following a force reduction is 1.37 fold, which is contingent upon the network becoming completely rigid under increasing forces before the force reduction. This factor of 1.37 is smaller than most velocity increases (7 out of 8 trials: 1.26-3.5, mean = 2.3) observed in force-clamp-reduction experiments. Thus network hardening alone cannot explain the observed history dependence.

B. Constant force experiment

In a constant force experiment, the cantilever is preloaded by moving the glass surface into contact until the desired force is reached. During the experiment, the surface is actively controlled to keep the cantilever deflection constant. In Figure I.2, the cantilever is preloaded and clamped at 38.35 nN. After ~115 minutes, the actin network begins to deflect the cantilever. Because the force on the network is not changing in this experiment, we expect a constant growth velocity. However, the developmental phase described in the text (Figure 4.2A), in which length increases exponentially with time, also exists in this experiment. The presence of the developmental phase in force-clamp experiments indicates that it is a transient phenomenon that is independent of the applied force.

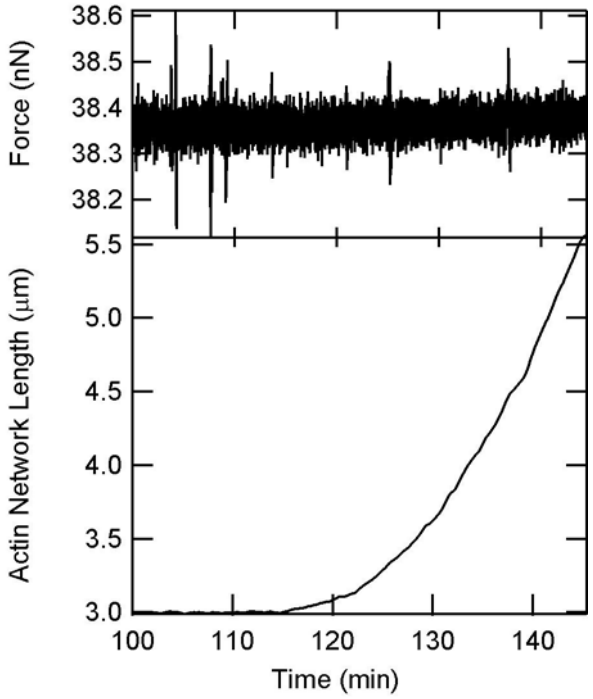

Figure I.2 Constant force experiment.

The cantilever force is set to 38.35 nN as shown in the top trace. The bottom trace shows the actin network length. The network begins to deflect the cantilever after about 115 minutes (black), and the network length increases super-linearly initially before growing linearly. The presence of the developmental phase in constant force experiments demonstrates that it is independent of force and transient.

A reasonable explanation of this behavior is that it is due to the initial formation of actin filaments. Machesky *et al.* found that Arp2/3 nucleation of branches involved the formation of a quaternary complex consisting of F-actin, G-actin, ActA, and the Arp2/3 complex[s3]. Essentially all actin in the extract mix was in the G-actin form due to ultracentrifugation of the crude extract. Thus, the lack of nascent F-actin may be rate limiting for initial actin network growth until the Arp 2/3 complex nucleates enough filaments to provide a stable structure for steady growth.

C. Mechanical stall

To verify that a force-dependent stall is observed, we reduced the force on a stalled network, and the network resumed elongation (Figure I.3).

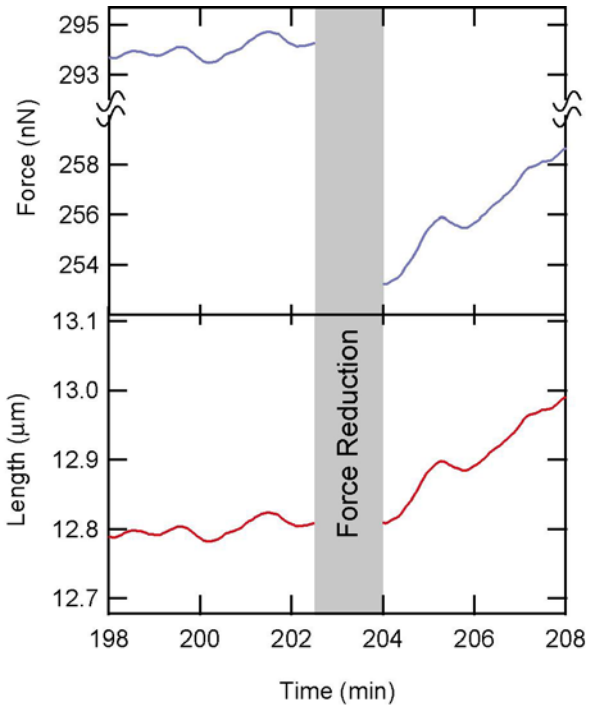

Figure I.3 Mechanical stall of dendritic actin network growth.

Force (red) and length (blue) versus time for actin growth during a mechanical stall test following the experiment illustrated in Figure 4.2A. Actin network growth was stalled for the first five minutes of this experiment. After the force was reduced from 295 nN to 254 nN, the actin network resumes growth. This demonstrates that stall was force-induced, and not due to depletion of actin or other factors.

References

s1. Gerbal, F., Chaikin, P., Rabin, Y. & Prost, J. An elastic analysis of Listeria monocytogenes propulsion. *Biophysical Journal* **79**, 2259-2275 (2000).

s2. Marcy, Y., Prost, J., Carlier, M. F. & Sykes, C. Forces generated during actin-based propulsion: A direct measurement by micromanipulation. *Proceedings of*

the National Academy of Sciences of the United States of America **101**, 5992-5997 (2004).

s3. Machesky, L. M. et al. Scar, a WASp-related protein, activates nucleation of actin filaments by the Arp2/3 complex. *Proceedings of the National Academy of Sciences of the United States of America* **96**, 3739-3744 (1999).

s4. Carlsson, A. E. Growth velocities of branched actin networks. *Biophysical Journal* **84**, 2907-2918 (2003).

APPENDIX II: SUPPLEMENTARY INFORMATION FOR CHAPTER 5

A. Additional methods

Protein preparation

Actin was purified from rabbit skeletal muscle acetone powder (Pelfreez, Inc.) [s1], labeled on random lysines with NHS-rhodamine (Pierce Biotechnology, Inc.), and cycled repeatedly to ensure polymerization competency. *Xenopus laevis* extract was prepared as previously described [s1]. Following isolation, crude extract was aliquoted and stored at -80°C. Extract mix was prepared by diluting crude extract to 50% with *Xenopus* buffer (XB) (100 mM KCl, 0.1 mM $CaCl_2$, 2 mM $MgCl_2$, 5 mM EGTA, 10 mM HEPES pH 7.7), spinning through Durapore® 100 nm centrifugation filters (Millipore) to remove large particulates, and adding 37.5 µl of 50% extract to 1.7 µl of energy mix (150 mM creating phosphate, 2mM EGTA, 20 mM $MgCl_2$, 20 mM ATP pH 7.4) and 1.7 µl of rhodamine-actin (1.7 mg/ml).

Dual-cantilever AFM

A dual-cantilever AFM has been developed to provide increased long-term stability for actin network measurements [s2]. Briefly, two silicon nitride cantilevers, supported by the same rigid support (Veeco Metrology, Inc.), are monitored with separate optical levers and position sensitive detectors (PSD, Pacific Silicon Sensor, Inc.) to allow accurate long timescale measurements of actin network growth. The PSD signals were calibrated before each experiment by incrementally driving the glass (bottom) surface into the cantilevers with an extremely accurate (resolution better than 0.05 nm) piezoelectric positioner (Physik Instrumente, GmBH) and subsequent fitting of the resulting PSD signal-position curve. Calibration data were used for real-time software feedback while experimental data signals from each PSD were anti-alias filtered with an 8-pole Butterworth filter (Krohn-hite, Inc.), recorded at 100 Hz with a PCI-6053E data acquisition board (National Instruments, Inc.), and saved for offline processing. Custom software written in LabView 7 (National Instruments, Inc.) was used to control data acquisition, calibration, cantilever feedback, and piezoelectric stage position for the instrument. Epi-fluorescence imaging was accomplished using a 32X 0.4NA objective (Carl Zeiss, Corp.) and a low-light cooled charge coupled device (CCD) (QImaging, Corp.).

During each experiment, the instrument was operated as a force-clamp and microrheometer. In a force-clamp, one cantilever was used as a reference to the bottom surface while the other cantilever was functionalized to nucleate actin network growth. Software feedback was used to hold the actin-associated cantilever's deflection, and therefore force, constant while the signal from the other cantilever reflects drift-corrected

changes in network length under the specified load. As a microrheometer, the force-clamp was disengaged, and the bottom surface was sinusoidally driven at specified frequencies while both cantilever positions were recorded at 1 kHz and saved for offline processing.

Experimental setup

Mechanical property experiments were performed with a cantilever having a mean stiffness of 100 pN/nm. This cantilever was dipped into a solution of 0.4 mg/ml ActA as described previously [s2] followed by immersion in 10 mg/ml bovine serum albumin (BSA) to prevent nonspecific adsorption of proteins from the extract mix during the experiments. No other cantilever was dipped in ActA. The cantilever was then loaded into the fluid cell, placed in the AFM, positioned near a piezoelectric-driven glass surface and immersed in extract mix. The surface was then finely adjusted, the PSD signals were calibrated, and a force-clamp was engaged to hold the network under a constant stress (~ 6 Pa) at the outset of each experiment.

Cantilever preparation

Uncoated silicon nitride cantilevers (Veeco Metrology, Inc.) were cleaned of organic contaminants using Piranha (3:1 sulphuric acid: hydrogen peroxide), rinsed in deionized water, and dried. Drying was followed by chemical vapor deposition (CVD) of amino-propyl-trimethoxy-silane (APTMS, Sigma Aldrich, Inc.) onto the cantilevers, after which cantilevers were stored under vacuum and used in experiments within 3 days.

Data Analysis for Figure 5.3B

For the averaged normalized nonlinear elasticity trace shown in Figure 5.3B of the text, the normalization parameters E_{min}, E_{max}, and σ_c for each individual set of measurements (corresponding to one nonlinear elasticity trace) was first determined from a sliding 5-point boxcar window for increasing stress. Then the traces (both for increasing and decreasing stresses) were normalized by these parameters. Each set of measurements was binned into 40 log-spaced bins between $0.005\sigma_c$ and $3\sigma_c$. All individual data sets for increasing stresses were then averaged together to produce the final averaged normalized (black) trace shown in Figure 5.3B of the manuscript, as were all data sets for decreasing stresses (Figure 5.3B, red trace). Each point represents data from at least 4 measurements though most represent data from more than 10 measurements.

B. Cantilever-surface interaction

To account for hydrodynamic influences between the oscillating surface and cantilever, we performed control measurements in which the surface was held at specific distances from the cantilever and oscillated at all frequencies. Our controls show that the interaction due to hydrodynamic effects is at most a 2 nm oscillation of the cantilever when the standoff distance is 0.5 μm, which is a spacing that was rarely achieved in any microrheology/nonlinear elasticity experiments (Figure II.1). The typical minimum spacing between the cantilever and surface in our experiments is ~ 1.5 μm, a spacing at which the cantilever amplitude of oscillation is less than 1 nm and is approaching the inherent Brownian fluctuations of the cantilever itself. Furthermore, this interaction

shows no clear frequency dependence at any standoff distance measured, which would be expected for a hydrodynamic coupling between the surface and cantilever [s3].

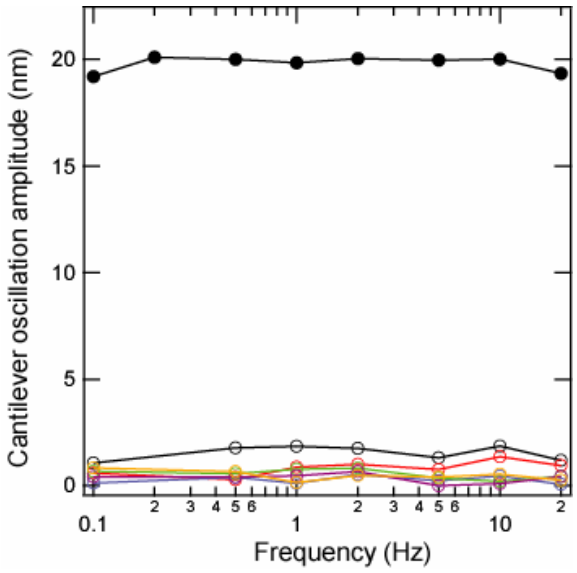

Figure II.1 Cantilever-surface coupling as a function of standoff distance from surface.

Open circles correspond to standoff distance of 0.500 µm (black), 1.5 µm (red), 2.5 µm (blue), 3.5 µm (green), 4.5 µm (magenta), and 5.5 µm (orange). Filled circles show cantilever deflection when in contact with the bottom surface, which matches the drive amplitude of 20 nm within experimental error. Cantilever oscillation is always less than 1 nm over relevant distances in our experiments when there is no actin network (1.5 µm and greater).

Another possible source of error in our measurements is time-dependent changes in the extract mix. It has been shown that cytoskeletal proteins in *Xenopus* extract will polymerize over time, which may change the mechanical properties [s4]. Control measurements where the cantilever was held 3 µm away from the surface showed little to no change in coupling after 100 minutes of immersion (Figure II.2).

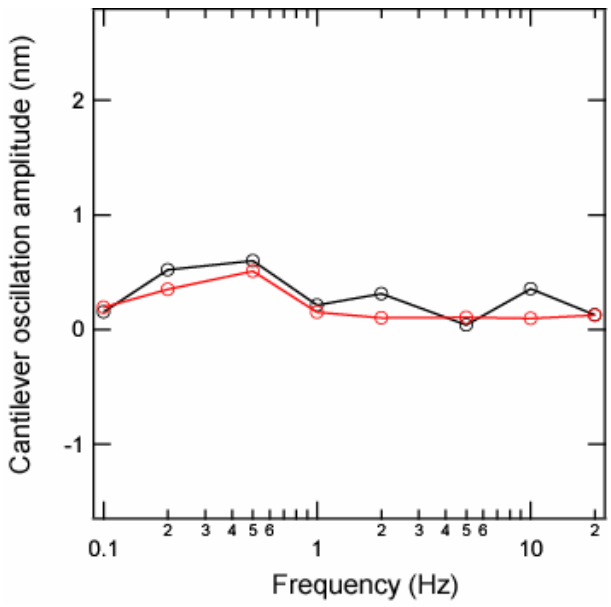

Figure II.2 Cantilever-surface coupling in extract mix does not change with time.

Black circles show coupling at t = 0 minutes after extract immersion and red circles show coupling at t = 100 minutes. The standoff distance used in this experiment was 3 μm.

C. Normalization method to determine power law

One particular measurement challenge had to be overcome before mechanical property data could be interpreted. Actin networks exhibit nonlinear elasticity, in which the elastic modulus increases with applied stresses beyond a critical value. We found that network growth during the rheology measurements slowly deflected the cantilever during the frequency sweep measurement thus affecting elasticity measurements due to the nonlinear elasticity of the network. To account for this, we performed the following normalization procedure: each measurement at a particular frequency was preceded and followed by a measurement at 5 Hz. The viscous and elastic moduli obtained for that measurement were then normalized by the average elastic modulus from the two 5 Hz measurements. This method yields relative viscous and elastic moduli that are always

compared to the 5 Hz elasticity, and is valid provided that the power law does not change significantly over the range of stresses traversed during one frequency sweep. We found this to be true (Figure II.3). In each frequency sweep, measurements were first done from 20 Hz to .1 Hz and then repeated from 1 Hz to 20 Hz. The power law obtained from the first segment of the sweep (20 Hz – 1 Hz) with an average stress of 11 Pa was found to be $x = 0.108$ (Figure II.3 red dotted line), while the power law over the second segment of the sweep (1 Hz – 20 Hz) was found to be $x = 0.104$ (Figure II.3, black dotted line) over an average stress of 24 Pa. This validates the application of this normalization procedure in determining the overall power law behavior.

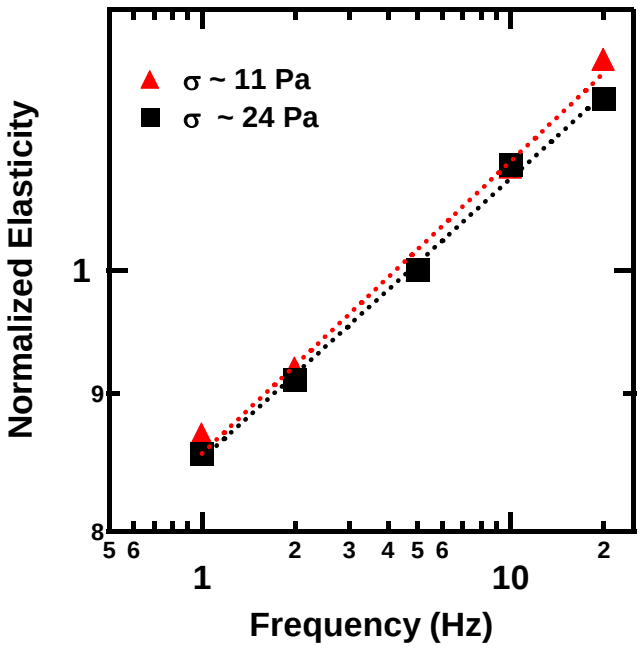

Figure II.3 Power law does not change significantly during a frequency sweep due to growth of the network.

Power law for measurements taken over an average stress of 11 Pa (n = 22, red triangles) is $x = 0.108$ (red dotted line) while the power law for measurements taken over an average stress of 24 Pa (n = 22, black squares) is $x = 0.104$ (black dotted line).

D. Myosin inhibition experiments

To determine whether there was any myosin dependent prestressing of the networks in these experiments, we performed frequency dependent microrheology experiments in the presence of 50 μM of blebbistatin (Sigma Aldrich, Inc.). Blebbistatin is a known myosin II inhibitor[s5]. The average elasticity at 5 Hz of these networks was 1.6 kPa (n = 2 trials, 20 measurements), among the higher range of elasticities seen without blebbistatin, demonstrating that myosin dependent prestress does not play a role in the elasticity of the dendritic actin networks studied here.

References

s1. Cameron, L. A., Footer, M. J., van Oudenaarden, A. & Theriot, J. A. *Proceedings of the National Academy of Sciences of the United States of America* **96**, 4908-4913 (1999).

s2. Parekh, S. H., Chaudhuri, O., Theriot, J. A. & Fletcher, D. A. *Nature Cell Biology* **7**, 1119-1123 (2005).

s3. Alcaraz, J. et al. *Biophysical Journal* **84**, 2071-2079 (2003).

s4. Valentine, M. T., Perlman, Z. E., Mitchison, T. J. & Weitz, D. A. *Biophysical Journal* **88**, 680-689 (2005).

s5. Limouze, J., Straight, A. F., Mitchison, T. & Sellers, J. E. *Journal of Muscle Research and Cell Motility* **25**, 337-341 (2004).

REFERENCES

1. Stachowiak, J. C., M. G. von Muhlen, T. H. Li, L. Jalilian, S. H. Parekh, and D. A. Fletcher. 2007. Piezoelectric control of needle-free transdermal drug delivery. Journal of Controlled Release 124:88-97.

2. Stachowiak, J. C., D. L. Richmond, T. H. Li, A. P. Liu, S. H. Parekh, and D. A. Fletcher. 2008. Unilamellar vesicle formation and encapsulation by microfluidic jetting. Proceedings of the National Academy of Sciences 105:4697-4702.

3. Chaudhuri, O., S. H. Parekh, W. A. Lam, and D. A. Fletcher. 2008. in preparation.

4. Einstein, A. 1906. The theory of the Brownian Motion. Annalen Der Physik 19:371-381.

5. Brown, R. 1828. A brief account of microscopical observations made in the months of June, July and August, 1827, on the particles contained in the pollen of plants; and on the general existence of active molecules in organic and inorganic bodies. Philosophical Magazine 4:161-173.

6. Random walks in biology. http://ezproxy.library.arizona.edu/login?url=http://site.ebrary.com/lib/arizona/Doc?id=10035929 An electronic book accessible through the World Wide Web; click to view, Accessed

7. Marieb, E. N., and J. Mallatt. *Human Anatomy*. Benjamin Cummings, 2001.

8. Svoboda, K., C. F. Schmidt, B. J. Schnapp, and S. M. Block. 1993. Direct Observation of Kinesin Stepping by Optical Trapping Interferometry. Nature 365:721-727.

9. Toyoshima, Y. Y., S. J. Kron, E. M. McNally, K. R. Niebling, C. Toyoshima, and J. A. Spudich. 1987. Myosin Subfragment-1 Is Sufficient to Move Actin-Filaments Invitro. Nature 328:536-539.

10. Vander, A. J., J. H. Sherman, and D. S. Luciano. *Human physiology : the mechanisms of body function*. McGraw-Hill, Boston, 2001.

11. Abercrombie, M., and J. E. M. Heaysman. 1953. Observations on the social behaviour of cells in tissue culture. I. Speed of movement of chick heart fibroblasts in relation to their mutual contacts. Exptl Cell Res 5:111-131.

12. CARTER, S. B. 1965. Principles of Cell Motility: The Direction of Cell Movement and Cancer Invasion. 208:1183-1187.

13. Mitchison, T. J., and L. P. Cramer. 1996. Actin-based cell motility and cell locomotion. Cell 84:371-379.

14. Verkhovsky, A. B., T. M. Svitkina, and G. G. Borisy. 1999. Self-polarization and directional motility of cytoplasm. Current Biology 9:11-20.

15. Alberts, B. *Molecular biology of the cell*. Garland Science, New York, 2008.

16. Theriot, J. A., and T. J. Mitchison. 1991. Actin Microfilament Dynamics in Locomoting Cells. Nature 352:126-131.

17. Cortese, J. D., B. Schwab, C. Frieden, and E. L. Elson. 1989. Actin Polymerization Induces a Shape Change in Actin-Containing Vesicles. Proceedings of the National Academy of Sciences of the United States of America 86:5773-5777.

18. Dabiri, G. A., J. M. Sanger, D. A. Portnoy, and F. S. Southwick. 1990. Listeria-Monocytogenes Moves Rapidly through the Host-Cell Cytoplasm by Inducing Directional Actin Assembly. Proceedings of the National Academy of Sciences of the United States of America 87:6068-6072.

19. Higgs, H. N., and T. D. Pollard. 2001. Regulation of actin filament network formation through Arp2/3 complex: Activation by a diverse array of proteins. Annual Review of Biochemistry 70:649-676.

20. Burns, S., G. O. Cory, W. Vainchenker, and A. J. Thrasher. 2004. Mechanisms of WASp-mediated hematologic and immunologic disease. Blood 104:3454-3462.

21. Wang, W. G., S. Goswami, E. Sahai, J. B. Wyckoff, J. E. Segall, and J. S. Condeelis. 2005. Tumor cells caught in the act of invading: their strategy for enhanced cell motility. Trends in Cell Biology 15:138-145.

22. Martin, T. A., G. Pereira, G. Watkins, R. E. Mansel, and W. G. Jiang. 2008. N-WASP is a putative tumour suppressor in breast cancer cells, in vitro and in vivo, and is associated with clinical outcome in patients with breast cancer. Clinical & Experimental Metastasis 25:97-108.

23. Yamazaki, D., S. Kurisu, and T. Takenawa. 2005. Regulation of cancer cell motility through actin reorganization. Cancer Science 96:379-386.

24. Adams, J. C. 2004. Roles of fascin in cell adhesion and motility. Current Opinion in Cell Biology 16:590-596.

25. Chhabra, E. S., and H. N. Higgs. 2007. The many faces of actin: Matching assembly factors with cellular structures. Nature Cell Biology 9:1110-1121.

26. Kaksonen, M., C. P. Toret, and D. G. Drubin. 2006. Harnessing actin dynamics for clathrin-mediated endocytosis. Nature Reviews Molecular Cell Biology 7:404-414.

27. Taunton, J., B. A. Rowning, M. L. Coughlin, M. Wu, R. T. Moon, T. J. Mitchison, and C. A. Larabell. 2000. Actin-dependent propulsion of endosomes and lysosomes by recruitment of N-WASP. Journal of Cell Biology 148:519-530.

28. Castellano, F., P. Chavrier, and E. Caron. 2001. Actin dynamics during phagocytosis. Seminars in Immunology 13:347-355.

29. Bernstein, B. W., and J. R. Bamburg. 1989. Cycling of Actin Assembly in Synaptosomes and Neurotransmitter Release. Neuron 3:257-265.

30. Pollard, T. D., and G. G. Borisy. 2003. Cellular motility driven by assembly and disassembly of actin filaments. Cell 113:549-549.

31. Howard, J. *Mechanics of motor proteins and the cytoskeleton*. Sinauer Associates, Publishers, Sunderland, Mass., 2001.

32. Pollard, T. D. 1986. Rate Constants for the Reactions of Atp-Actin and Adp-Actin with the Ends of Actin-Filaments. Journal of Cell Biology 103:2747-2754.

33. Pollard, T. D., L. Blanchoin, and R. D. Mullins. 2000. Molecular mechanisms controlling actin filament dynamics in nonmuscle cells. Annual Review of Biophysics and Biomolecular Structure 29:545-576.

34. Fujiwara, I., S. Takahashi, H. Tadakuma, T. Funatsu, and S. Ishiwata. 2002. Microscopic analysis of polymerization dynamics with individual actin filaments. Nature Cell Biology 4:666-673.

35. Welch, M. D., and R. D. Mullins. 2002. Cellular control of actin nucleation. Annual Review of Cell and Developmental Biology 18:247-288.

36. Bausch, A. R., and K. Kroy. 2006. A bottom-up approach to cell mechanics. Nature Physics 2:231-238.

37. Chaudhuri, O., S. H. Parekh, and D. A. Fletcher. 2007. Reversible stress softening of actin networks. Nature 445:295-298.

38. Svitkina, T. M., and G. G. Borisy. 1999. Arp2/3 complex and actin depolymerizing factor cofilin in dendritic organization and treadmilling of actin filament array in lamellipodia. Journal of Cell Biology 145:1009-1026.

39. Welch, M. D., A. Iwamatsu, and T. J. Mitchison. 1997. Actin polymerization is induced by Arp2/3 protein complex at the surface of Listeria monocytogenes. Nature 385:265-269.

40. Goley, E. D., and M. D. Welch. 2006. The ARP2/3 complex: an actin nucleator comes of age. Nature Reviews Molecular Cell Biology 7:713-726.

41. Mullins, R. D., J. A. Heuser, and T. D. Pollard. 1998. The interaction of Arp2/3 complex with actin: Nucleation, high affinity pointed end capping, and formation of branching networks of filaments. Proceedings of the National Academy of Sciences of the United States of America 95:6181-6186.

42. Smith, G. A., D. A. Portnoy, and J. A. Theriot. 1995. Asymmetric Distribution of the Listeria-Monocytogenes Acta Protein Is Required and Sufficient to Direct Actin-Based Motility. Molecular Microbiology 17:945-951.

43. Cameron, L. A., M. J. Footer, A. van Oudenaarden, and J. A. Theriot. 1999. Motility of ActA protein-coated microspheres driven by actin polymerization. Proceedings of the National Academy of Sciences of the United States of America 96:4908-4913.

44. Jeng, R. L., E. D. Goley, J. A. D'Alessio, O. Y. Chaga, T. M. Svitkina, G. G. Borisy, R. A. Heinzen, and M. D. Welch. 2004. A Rickettsia WASP-like protein activates the Arp2/3 complex and mediates actin-based motility. Cellular Microbiology 6:761-769.

45. Rohatgi, R., H. Y. H. Ho, and M. W. Kirschner. 2000. Mechanism of N-WASP activation by CDC42 and phosphatidylinositol 4,5-bisphosphate. Journal of Cell Biology 150:1299-1309.

46. Blanchoin, L., T. D. Pollard, and R. D. Mullins. 2000. Interactions of ADF/cofilin, Arp2/3 complex, capping protein and profilin in remodeling of branched actin filament networks. Current Biology 10:1273-1282.

47. Cooper, J. A., and T. D. Pollard. 1985. Effect of Capping Protein on the Kinetics of Actin Polymerization. Biochemistry 24:793-799.

48. McGough, A., B. Pope, W. Chiu, and A. Weeds. 1997. Cofilin Changes the Twist of F-Actin: Implications for Actin Filament Dynamics and Cellular Function 10.1083/jcb.138.4.771. J. Cell Biol. 138:771-781.

49. DesMarais, V., M. Ghosh, R. Eddy, and J. Condeelis. 2005. Cofilin takes the lead. Journal of Cell Science 118:19-26.

50. Goldschmidtclermont, P. J., M. I. Furman, D. Wachsstock, D. Safer, V. T. Nachmias, and T. D. Pollard. 1992. The Control of Actin Nucleotide Exchange by Thymosin-Beta-4 and Profilin - a Potential Regulatory Mechanism for Actin Polymerization in Cells. Molecular Biology of the Cell 3:1015-1024.

51. Vinson, V. K., E. M. De la Cruz, H. N. Higgs, and T. D. Pollard. 1998. Interactions of Acanthamoeba profilin with actin and nucleotides bound to actin. Biochemistry 37:10871-10880.

52. Amann, K. J., and T. D. Pollard. 2001. The Arp2/3 complex nucleates actin filament branches from the sides of pre-existing filaments. Nature Cell Biology 3:306-310.

53. Pantaloni, D., R. Boujemaa, D. Didry, P. Gounon, and M. F. Carlier. 2000. The Arp2/3 complex branches filament barbed ends: functional antagonism with capping proteins. Nature Cell Biology 2:385-391.

54. Hill, T. L., and M. W. Kirschner. 1982. Bioenergetics and Kinetics of Microtubule and Actin Filament Assembly-Disassembly. International Review of Cytology-a Survey of Cell Biology 78:1-125.

55. Footer, M. J., J. W. J. Kerssemakers, J. A. Theriot, and M. Dogterom. 2007. Direct measurement of force generation by actin filament polymerization using an optical trap. Proceedings of the National Academy of Sciences of the United States of America 104:2181-2186.

56. Kovar, D. R., and T. D. Pollard. 2004. Insertional assembly of actin filament barbed ends in association with formins produces piconewton forces. Proceedings of the National Academy of Sciences of the United States of America 101:14725-14730.

57. Isambert, H., P. Venier, A. Maggs, A. Fattoum, R. Kassab, D. Pantaloni, and M. Carlier. 1995. Flexibility of actin filaments derived from thermal fluctuations. Effect of bound nucleotide, phalloidin, and muscle regulatory proteins. J. Biol. Chem. 270:11437-11444.

58. Peskin, C. S., G. M. Odell, and G. F. Oster. 1993. Cellular Motions and Thermal Fluctuations - the Brownian Ratchet. Biophysical Journal 65:316-324.

59. Mogilner, A., and G. Oster. 2003. Polymer motors: Pushing out the front and pulling up the back. Current Biology 13:R721-R733.

60. Mogilner, A., and G. Oster. 1996. Cell motility driven by actin polymerization. Biophysical Journal 71:3030-3045.

61. Mogilner, A., and G. Oster. 2003. Force generation by actin polymerization II: The elastic ratchet and tethered filaments. Biophysical Journal 84:1591-1605.

62. Gerbal, F., V. Laurent, A. Ott, M. F. Carlier, P. Chaikin, and J. Prost. 2000. Measurement of the elasticity of the actin tail of Listeria monocytogenes. European Biophysics Journal with Biophysics Letters 29:134-140.

63. Kuo, S. C., and J. L. McGrath. 2000. Steps and fluctuations of Listeria monocytogenes during actin-based motility. Nature 407:1026-1029.

64. Dickinson, R. B., L. Caro, and D. L. Purich. 2004. Force generation by cytoskeletal filament end-tracking proteins. Biophysical Journal 87:2838-2854.

65. Marcy, Y., J. Prost, M. F. Carlier, and C. Sykes. 2004. Forces generated during actin-based propulsion: A direct measurement by micromanipulation. Proceedings of the National Academy of Sciences of the United States of America 101:5992-5997.

66. Gerbal, F., P. Chaikin, Y. Rabin, and J. Prost. 2000. An elastic analysis of Listeria monocytogenes propulsion. Biophysical Journal 79:2259-2275.

67. Carlsson, A. E. 2003. Growth velocities of branched actin networks. Biophysical Journal 84:2907-2918.

68. Cameron, L. A., P. A. Giardini, F. S. Soo, and J. A. Theriot. 2000. Secrets of actin-based motility revealed by a bacterial pathogen. Nature Reviews Molecular Cell Biology 1:110-119.

69. Upadhyaya, A., J. R. Chabot, A. Andreeva, A. Samadani, and A. van Oudenaarden. 2003. Probing polymerization forces by using actin-propelled lipid vesicles. Proceedings of the National Academy of Sciences of the United States of America 100:4521-4526.

70. Giardini, P. A., D. A. Fletcher, and J. A. Theriot. 2003. Compression forces generated by actin comet tails on lipid vesicles. Proceedings of the National Academy of Sciences of the United States of America 100:6493-6498.

71. McGrath, J. L., N. J. Eungdamrong, C. I. Fisher, F. Peng, L. Mahadevan, T. J. Mitchison, and S. C. Kuo. 2003. The force-velocity relationship for the actin-based motility of Listeria monocytogenes. Current Biology 13:329-332.

72. Wiesner, S., E. Helfer, D. Didry, G. Ducouret, F. Lafuma, M. F. Carlier, and D. Pantaloni. 2003. A biomimetic motility assay provides insight into the mechanism of actin-based motility. Journal of Cell Biology 160:387-398.

73. Shaevitz, J. W., and D. A. Fletcher. 2007. Load fluctuations drive actin network growth. Proceedings of the National Academy of Sciences of the United States of America 104:15688-15692.

74. Parekh, S. H., O. Chaudhuri, J. A. Theriot, and D. A. Fletcher. 2005. Loading history determines the velocity of actin-network growth. Nature Cell Biology 7:1119-1123.

75. Gittes, F., B. Mickey, J. Nettleton, and J. Howard. 1993. Flexural Rigidity of Microtubules and Actin-Filaments Measured from Thermal Fluctuations in Shape. Journal of Cell Biology 120:923-934.

76. Stossel, T. P. 1993. On the Crawling of Animal-Cells. Science 260:1086-1094.

77. Bustamante, C., J. F. Marko, E. D. Siggia, and S. Smith. 1994. Entropic Elasticity of Lambda-Phage DNA. Science 265:1599-1600.

78. Gennes, P.-G. d. *Scaling concepts in polymer physics*. Cornell University Press, Ithaca, N.Y., 1979.

79. Janmey, P. A., and D. A. Weitz. 2004. Dealing with mechanics: mechanisms of force transduction in cells. Trends in Biochemical Sciences 29:364-370.

80. Alcaraz, J., L. Buscemi, M. Grabulosa, X. Trepat, B. Fabry, R. Farre, and D. Navajas. 2003. Microrheology of human lung epithelial cells measured by atomic force microscopy. Biophysical Journal 84:2071-2079.

81. Mahaffy, R. E., C. K. Shih, F. C. MacKintosh, and J. Kas. 2000. Scanning probe-based frequency-dependent microrheology of polymer gels and biological cells. Physical Review Letters 85:880-883.

82. Gardel, M. L., J. C. Crocker, M. T. Valentine, A. R. Bausch, and D. A. Weitz. 2003. One- and two-particle microrheology of F-actin. Biophysical Journal 84:437A-437A.

83. Gardel, M. L., J. H. Shin, F. C. MacKintosh, L. Mahadevan, P. Matsudaira, and D. A. Weitz. 2004. Elastic Behavior of cross-linked and bundled actin networks. Science 304:1301-1305.

84. Xu, J. Y., D. Wirtz, and T. D. Pollard. 1998. Dynamic cross-linking by alpha-actinin determines the mechanical properties of actin filament networks. Journal of Biological Chemistry 273:9570-9576.

85. Tseng, Y., and D. Wirtz. 2004. Dendritic branching and homogenization of actin networks mediated by Arp2/3 complex. Physical Review Letters 93.

86. Kasza, K. E., A. C. Rowat, J. Y. Liu, T. E. Angelini, C. P. Brangwynne, G. H. Koenderink, and D. A. Weitz. 2007. The cell as a material. Current Opinion in Cell Biology 19:101-107.

87. Storm, C., J. J. Pastore, F. C. MacKintosh, T. C. Lubensky, and P. A. Janmey. 2005. Nonlinear elasticity in biological gels. Nature 435:191-194.

88. Gardel, M. L., F. Nakamura, J. H. Hartwig, J. C. Crocker, T. P. Stossel, and D. A. Weitz. 2006. Prestressed F-actin networks cross-linked by hinged filamins replicate mechanical properties of cells. Proceedings of the National Academy of Sciences of the United States of America 103:1762-1767.

89. Wagner, B., R. Tharmann, I. Haase, M. Fischer, and A. R. Bausch. 2006. Cytoskeletal polymer networks: The molecular structure of cross-linkers determines macroscopic properties. Proceedings of the National Academy of Sciences of the United States of America 103:13974-13978.

90. Xu, J. Y., Y. Tseng, and D. Wirtz. 2000. Strain hardening of actin filament networks - Regulation by the dynamic cross-linking protein alpha-actinin. Journal of Biological Chemistry 275:35886-35892.

91. Shin, J. H., M. L. Gardel, L. Mahadevan, P. Matsudaira, and D. A. Weitz. 2004. Relating microstructure to rheology of a bundled and cross-linked F-actin network in vitro. Proceedings of the National Academy of Sciences of the United States of America 101:9636-9641.

92. Mizuno, D., C. Tardin, C. F. Schmidt, and F. C. MacKintosh. 2007. Nonequilibrium mechanics of active cytoskeletal networks. Science 315:370-373.

93. Deguchi, S., T. Ohashi, and M. Sato. 2006. Tensile properties of single stress fibers isolated from cultured vascular smooth muscle cells. Journal of Biomechanics 39:2603-2610.

94. Binnig, G., C. F. Quate, and C. Gerber. 1986. Atomic Force Microscope. Physical Review Letters 56:930-933.

95. Meyer, G., and N. M. Amer. 1988. Novel Optical Approach to Atomic Force Microscopy. Applied Physics Letters 53:1045-1047.

96. Bustamante, C., J. C. Macosko, and G. J. L. Wuite. 2000. Grabbing the cat by the tail: Manipulating molecules one by one. Nature Reviews Molecular Cell Biology 1:130-136.

97. Sarid, D. *Scanning force microscopy : with applications to electric, magnetic, and atomic forces*. Oxford University Press, New York, 1994.

98. Rief, M., F. Oesterhelt, B. Heymann, and H. E. Gaub. 1997. Single molecule force spectroscopy on polysaccharides by atomic force microscopy. Science 275:1295-1297.

99. Fernandez, J. M., and H. B. Li. 2004. Force-clamp spectroscopy monitors the folding trajectory of a single protein. Science 303:1674-1678.

100. Radmacher, M., M. Fritz, C. M. Kacher, J. P. Cleveland, and P. K. Hansma. 1996. Measuring the viscoelastic properties of human platelets with the atomic force microscope. Biophysical Journal 70:556-567.

101. Rosenbluth, M. J., W. A. Lam, and D. A. Fletcher. 2006. Force microscopy of nonadherent cells: A comparison of leukemia cell deformability. Biophysical Journal 90:2994-3003.

102. Rivetti, C., M. Guthold, and C. Bustamante. 1996. Scanning force microscopy of DNA deposited onto mica: Equilibration versus kinetic trapping studied by statistical polymer chain analysis. Journal of Molecular Biology 264:919-932.

103. Dupres, V., F. D. Menozzi, C. Locht, B. H. Clare, N. L. Abbott, S. Cuenot, C. Bompard, D. Raze, and Y. F. Dufrene. 2005. Nanoscale mapping and functional analysis of individual adhesins on living bacteria. Nature Methods 2:515-520.

104. Wu, G. H., R. H. Datar, K. M. Hansen, T. Thundat, R. J. Cote, and A. Majumdar. 2001. Bioassay of prostate-specific antigen (PSA) using microcantilevers. Nature Biotechnology 19:856-860.

105. Sulchek, T. A., R. W. Friddle, K. Langry, E. Y. Lau, H. Albrecht, T. V. Ratto, S. J. DeNardo, M. E. Colvin, and A. Noy. 2005. Dynamic force spectroscopy of parallel individual Mucin1-antibody bonds. Proceedings of the National Academy of Sciences of the United States of America 102:16638-16643.

106. Rief, M., M. Gautel, F. Oesterhelt, J. M. Fernandez, and H. E. Gaub. 1997. Reversible unfolding of individual titin immunoglobulin domains by AFM. Science 276:1109-1112.

107. Jena, B. P., and J. K. H. Hèorber. *Atomic force microscopy in cell biology*. Academic Press, San Diego, 2002.

108. Hansma, H. G., J. Vesenka, C. Siegerist, G. Kelderman, H. Morrett, R. L. Sinsheimer, V. Elings, C. Bustamante, and P. K. Hansma. 1992. Reproducible Imaging and Dissection of Plasmid DNA under Liquid with the Atomic Force Microscope. Science 256:1180-1184.

109. Kindt, J. H., G. E. Fantner, J. A. Cutroni, and P. K. Hansma. 2004. Rigid design of fast scanning probe microscopes using finite element analysis. Ultramicroscopy 100:259-265.

110. Viani, M. B., T. E. Schaffer, A. Chand, M. Rief, H. E. Gaub, and P. K. Hansma. 1999. Small cantilevers for force spectroscopy of single molecules. Journal of Applied Physics 86:2258-2262.

111. Hoh, J. H., and P. K. Hansma. 1992. Atomic Force Microscopy for High-Resolution Imaging in Cell Biology. Trends in Cell Biology 2:208-213.

112. AFM schematic. http://www3.physik.uni-greifswald.de/method/afm/AFM_laser.gif, Accessed April 13, 2008

113. Gustafsson, M. G. L., and J. Clarke. 1994. Scanning force microscope springs optimized for optical-beam deflection and with tips made by controlled fracture. Journal of Applied Physics 76:172-181.

114. Jaschke, M., and H.-J. Butt. 1995. Height calibration of optical lever atomic force microscopes by simple laser interferometry. Review of Scientific Instruments 66:1258-1259.

115. OSI Optoelectronics Application Notes. http://www.udt.com/application-notes.asp, Accessed April 10, 2008

116. Li, T. D., and E. Riedo. 2008. Nonlinear viscoelastic dynamics of nanoconfined wetting liquids. Physical Review Letters 100.

117. Wallmark, J. T. 1957. A New Semiconductor Photocell Using Lateral Photoeffect. Proceedings of the Institute of Radio Engineers 45:474-483.

118. Horowitz, P., and W. Hill. *The art of electronics*. Cambridge University Press, Cambridge [England] ; New York, 1989.

119. Nise, N. S. 2000. Control systems engineering. John Wiley, New York.

120. Physik Instrumente piezo tutorials. http://www.physikinstrumente.com/en/products/piezo_tutorial.php, Accessed April 9, 2008

121. Gradinaru, C. C., P. Martinsson, T. J. Aartsma, and T. Schmidt. 2004. Simultaneous atomic-force and two-photon fluorescence imaging of biological specimens in vivo. Ultramicroscopy 99:235-245.

122. Neuman, K. C., and S. M. Block. 2004. Optical trapping. Review of Scientific Instruments 75:2787-2809.

123. Levy, R., and M. Maaloum. 2002. Measuring the spring constant of atomic force microscope cantilevers: thermal fluctuations and other methods. Nanotechnology 13:33-37.

124. Hutter, J. L., and J. Bechhoefer. 1993. Calibration of atomic-force microscope tips. Review of Scientific Instruments 64:1868-1873.

125. Butt, H. J., and M. Jaschke. 1995. Calculation of Thermal Noise in Atomic-Force Microscopy. Nanotechnology 6:1-7.

126. Bustamante, C., Y. R. Chemla, N. R. Forde, and D. Izhaky. 2004. Mechanical processes in biochemistry. In Annual Review of Biochemistry. 705-748.

127. Shaevitz, J. W., E. A. Abbondanzieri, R. Landick, and S. M. Block. 2003. Backtracking by single RNA polymerase molecules observed at near-base-pair resolution. Nature 426:684-687.

128. Nugent-Glandorf, L., and T. T. Perkins. 2004. Measuring 0.1-nm motion in 1 ms in an optical microscope with differential back-focal-plane detection. Optics Letters 29:2611-2613.

129. Altmann, S. M., P. F. Lenne, and J. K. H. Horber. 2001. Multiple sensor stabilization system for local probe microscopes. Review of Scientific Instruments 72:142-149.

130. Sparks, A. W., and S. R. Manalis. 2006. Atomic force microscopy with inherent disturbance suppression for nanostructure imaging. Nanotechnology 17:1574-1579.

131. Schitter, G., and A. Stemmer. 2002. Eliminating mechanical perturbations in scanning probe microscopy. Nanotechnology 13:663-665.

132. Sparks, A. W., and S. R. Manalis. 2004. Scanning probe microscopy with inherent disturbance suppression. Applied Physics Letters 85:3929-3931.

133. Vonna, L., A. Wiedemann, M. Aepfelbacher, and E. Sackmann. 2003. Local force induced conical protrusions of phagocytic cells. Journal of Cell Science 116:785-790.

134. Radmacher, M., J. P. Cleveland, and P. K. Hansma. 1995. Improvement of Thermally-Induced Bending of Cantilevers Used for Atomic-Force Microscopy. Scanning 17:117-121.

135. Savran, C. A., T. P. Burg, J. Fritz, and S. R. Manalis. 2003. Microfabricated mechanical biosensor with inherently differential readout. Applied Physics Letters 83:1659-1661.

136. Beyder, A., C. Spagnoli, and F. Sachs. 2006. Reducing probe dependent drift in atomic force microscope with symmetrically supported torsion levers. Review of Scientific Instruments 77.

137. Abraham, D. W., C. C. Williams, and H. K. Wickramasinghe. 1988. Noise-Reduction Technique for Scanning Tunneling Microscopy. Applied Physics Letters 53:1503-1505.

138. Tabard-Cossa, V., M. Godin, L. Y. Beaulieu, and P. Grutter. 2005. A differential microcantilever-based system for measuring surface stress changes induced by electrochemical reactions. Sensors and Actuators B-Chemical 107:233-241.

139. Wickramasinghe, H. K. 1990. Scanning Probe Microscopy - Current Status and Future-Trends. J Vac Sci Technol A 8:363-368.

140. Schaffer, T. E., and P. K. Hansma. 1998. Characterization and optimization of the detection sensitivity of an atomic force microscope for small cantilevers. Journal of Applied Physics 84:4661-4666.

141. Drake, B., C. B. Prater, A. L. Weisenhorn, S. A. C. Gould, T. R. Albrecht, C. F. Quate, D. S. Cannell, H. G. Hansma, and P. K. Hansma. 1989. Imaging Crystals,

Polymers, and Processes in Water with the Atomic Force Microscope. Science 243:1586-1589.

142. Walters, D. A., J. P. Cleveland, N. H. Thomson, P. K. Hansma, M. A. Wendman, G. Gurley, and V. Elings. 1996. Short cantilevers for atomic force microscopy. Review of Scientific Instruments 67:3583-3590.

143. Gimzewski, J. K., and C. Joachim. 1999. Nanoscale science of single molecules using local probes. Science 283:1683-1688.

144. Weizmann, Y., F. Patolsky, O. Lioubashevski, and I. Willner. 2004. Magneto-mechanical detection of nucleic acids and telomerase activity in cancer cells. Journal of the American Chemical Society 126:1073-1080.

145. Wu, G. H., H. F. Ji, K. Hansen, T. Thundat, R. Datar, R. Cote, M. F. Hagan, A. K. Chakraborty, and A. Majumdar. 2001. Origin of nanomechanical cantilever motion generated from biomolecular interactions. Proceedings of the National Academy of Sciences of the United States of America 98:1560-1564.

146. Spudich, J. A., and S. Watt. 1971. Regulation of Rabbit Skeletal Muscle Contraction .1. Biochemical Studies of Interaction of Tropomyosin-Troponin Complex with Actin and Proteolytic Fragments of Myosin. Journal of Biological Chemistry 246:4866-&.

147. Rozelle, A. L., L. M. Machesky, M. Yamamoto, M. H. E. Driessens, R. H. Insall, M. G. Roth, K. Luby-Phelps, G. Marriott, A. Hall, and H. L. Yin. 2000. Phosphatidylinositol 4,5-bisphosphate induces actin-based movement of raft-enriched vesicles through WASP-Arp2/3. Current Biology 10:311-320.

148. Merrifield, C. J., S. E. Moss, C. Ballestrem, B. A. Imhof, G. Giese, I. Wunderlich, and W. Almers. 1999. Endocytic vesicles move at the tips of actin tails in cultured mast cells. Nature Cell Biology 1:72-74.

149. Theriot, J. A., T. J. Mitchison, L. G. Tilney, and D. A. Portnoy. 1992. The Rate of Actin-Based Motility of Intracellular Listeria-Monocytogenes Equals the Rate of Actin Polymerization. Nature 357:257-260.

150. Loisel, T. P., R. Boujemaa, D. Pantaloni, and M. F. Carlier. 1999. Reconstitution of actin-based motility of Listeria and Shigella using pure proteins. Nature 401:613-616.

151. Upadhyaya, A., and A. van Oudenaarden. 2003. Biomimetic systems for studying actin-based motility. Current Biology 13:R734-R744.

152. C. Bustamante, Y. R. Chemla, N. R. Forde, D. Izhaky, in Annual Review of Biochemistry. (2004), vol. 73, pp. 705-748 and references contained within

153. Dogterom, M., and B. Yurke. 1997. Measurement of the force-velocity relation for growing microtubules. Science 278:856-860.

154. Dickinson, R. B., and D. L. Purich. 2002. Clamped-filament elongation model for actin-based motors. Biophysical Journal 82:605-617.

155. Schwartz, I. M., M. Ehrenberg, M. Bindschadler, and J. L. McGrath. 2004. The role of substrate curvature in actin-based pushing forces. Current Biology 14:1094-1098.

156. Wang, M. D., M. J. Schnitzer, H. Yin, R. Landick, J. Gelles, and S. M. Block. 1998. Force and velocity measured for single molecules of RNA polymerase. Science 282:902-907.

157. Smith, D. E., S. J. Tans, S. B. Smith, S. Grimes, D. L. Anderson, and C. Bustamante. 2001. The bacteriophage phi 29 portal motor can package DNA against a large internal force. Nature 413:748-752.

158. Finer, J. T., R. M. Simmons, and J. A. Spudich. 1994. Single Myosin Molecule Mechanics - Piconewton Forces and Nanometer Steps. Nature 368:113-119.

159. Kellogg, D. R., T. J. Mitchison, and B. M. Alberts. 1988. Behavior of Microtubules and Actin-Filaments in Living Drosophila Embryos. Development 103:675-686.

160. Choy, J. L., S. H. Parekh, O. Chaudhuri, A. P. Liu, C. Bustamante, M. J. Footer, J. A. Theriot, and D. A. Fletcher. 2007. Differential force microscope for long time-scale biophysical measurements. Review of Scientific Instruments 78.

161. Satcher, R. L., and C. F. Dewey. 1996. Theoretical estimates of mechanical properties of the endothelial cell cytoskeleton. Biophysical Journal 71:109-118.

162. Mackintosh, F. C., J. Kas, and P. A. Janmey. 1995. Elasticity of Semiflexible Biopolymer Networks. Physical Review Letters 75:4425-4428.

163. Kroy, K., and E. Frey. 1996. Force-extension relation and plateau modulus for wormlike chains. Physical Review Letters 77:306-309.

164. Head, D. A., A. J. Levine, and E. C. MacKintosh. 2003. Deformation of cross-linked semiflexible polymer networks. Physical Review Letters 91.

165. Cameron, L. A., T. M. Svitkina, D. Vignjevic, J. A. Theriot, and G. G. Borisy. 2001. Dendritic organization of actin comet tails. Current Biology 11:130-135.

166. Stamenovic, D., B. Suki, B. Fabry, N. Wang, and J. J. Fredberg. 2004. Rheology of airway smooth muscle cells is associated with cytoskeletal contractile stress. Journal of Applied Physiology 96:1600-1605.

167. Fabry, B., G. N. Maksym, J. P. Butler, M. Glogauer, D. Navajas, and J. J. Fredberg. 2001. Scaling the microrheology of living cells. Physical Review Letters 8714.

168. Nakamura, F., E. Osborn, P. A. Janmey, and T. P. Stossel. 2002. Comparison of filamin A-induced cross-linking and Arp2/3 complex-mediated branching on the mechanics of actin filaments. Journal of Biological Chemistry 277:9148-9154.

169. Landau, L. D., and E. M. Lifshitz. *Theory of Elasticity*, 1986.

170. Onck, P. R., T. Koeman, T. van Dillen, and E. van der Giessen. 2005. Alternative explanation of stiffening in cross-linked semiflexible networks. Physical Review Letters 95.

171. Coughlin, M. F., and D. Stamenovic. 1998. A tensegrity model of the cytoskeleton in spread and round cells. Journal of Biomechanical Engineering-Transactions of the Asme 120:770-777.

172. Gibson, L. J., and M. F. Ashby. *Cellular Solids: structure & properties*. Pergamon Press, 1988.

173. Brangwynne, C. P., F. C. MacKintosh, S. Kumar, N. A. Geisse, J. Talbot, L. Mahadevan, L. L. Parker, D. E. Ingber, and D. A. Weitz. 2006. Microtubules can bear enhanced compressive loads in living cells because of lateral reinforcement. The Journal of Cell Biology 173:733-741.

174. Prass, M., K. Jacobson, A. Mogilner, and M. Radmacher. 2006. Direct measurement of the lamellipodial protrusive force in a migrating cell. Journal of Cell Biology 174:767-772.

175. Patolsky, F., Y. Weizmann, and I. Willner. 2004. Actin-based metallic nanowires as bio-nanotransporters. Nature Materials 3:692-695.

176. Liu, A. P., and D. A. Fletcher. 2005. Photopatterning of actin filament structures. Nano Letters 5:625-628.

Publishing Agreement

It is the policy of the University to encourage the distribution of all theses and dissertations. Copies of all UCSF theses and dissertations will be routed to the library via the Graduate Division. The library will make all theses and dissertations accessible to the public and will preserve these to the best of their abilities, in perpetuity.

I hereby grant permission to the Graduate Division of the University of California, San Francisco to release copies of my thesis or dissertation to the Campus Library to provide access and preservation, in whole or in part, in perpetuity.

Author Signature

05/27/09
Date